Fat-water separated T_1 mapping with inversion-prepared multi-echo MRI

Marc-Antoine Fortin
Medical Physics Unit
McGill University, Montreal

A thesis submitted to McGill University in partial fulfilment of the degree of
M.Sc. Medical Radiation Physics

Table of Contents

Acknowledgments

Foremost, I would like to thank my supervisor Prof. Ives Levesque for giving me the opportunity to join the MRI Methods Research Group at McGill University as an undergraduate intern at first and as one of his MSc students more recently. Being supervised by Prof. Ives Levesque was a privilege and his guidance helped me becoming the researcher that I am today. The dedication and support of Prof. Ives Levesque towards his students is unmatched, and above all, invaluable.

I would also like to thank the lab members I met while being in the MRI Methods Research Group: Véronique Fortier, Jorge Campos Pazmino, Zaki Ahmed, Alex Ensworth, Dipal Patel, Anastasia Kolokotronis and Stella Xing. A special thanks to Veronique Fortier, PhD, who helped me with the fat-water separation implementation, data acquisition, phantom design and valuable feedback during my project and Jorge Campos Pazmino who is the best MSc student partner I could have wished for during my Master's. In addition, I would like to personally express my gratitude towards the other MSc students graduating with me this year and the rest of staff, students and faculty members at the Medical Physics Unit at McGill University that created the best learning atmosphere during my Master's.

I would like to thank NSERC for the financial support granted throughout my graduate studies. Furthermore, I would like to express my thanks to Andre van der Kouwe, PhD, from the Athinoula A. Martinos Center for Biomedical Imaging at the Massachusetts General Hospital (MGH) for sharing the ME-MP2RAGE sequence used in this project and answering many of my questions throughout this project.

In the end, I would like to thank my family and friends for their constant support during the duration of my studies. They helped me becoming the person I am today. Specifically, my mother who helped me substantially in the past several months when I could not walk. I also owe a special thank you to my girlfriend, Alexanne Lupien, who supports me in everything I do and who is my favorite guinea pig to practice the vulgarization of my work.

Abstract

Knowing the oxygen level inside cancer tumors before radiotherapy can significantly affect the choice of treatment Currently, measuring oxygen levels *in vivo* before radiotherapy is not performed due to the lack of a simple and validated method that could be easily incorporated clinically. Recent work in Magnetic Resonance Imaging (MRI) reported that variations in fat T_1 values could be used as an indirect and non-invasive method to measure tissue oxygenation. For this purpose, the Magnetization Prepared Two Rapid Acquisition of Gradient Echoes (MP2RAGE) sequence designed for brain T_1 mapping and 3-point Dixon to perform fat-water separation were adapted and combined to design a novel fat-water separated T_1 mapping technique from a multi echo (ME) MP2RAGE sequence.

Extensive assessment and validation of the accuracy and precision of the newly designed ME-MP2RAGE protocol were performed throughout this project. First, from a qualitative assessment of the acquisition parameters, the original MP2RAGE protocol developed for T_1 values between 1000 ms and 2000 ms (typical of brain tissue at 3 T) was modified to be optimized for a T_1 range between 200 ms and 800 ms. A quantitative assessment of the theoretical accuracy and precision for the new short T_1 MP2RAGE protocol was performed with numerical simulations to compare with the original brain T_1 MP2RAGE protocol. Afterwards, the short T_1 MP2RAGE protocol was experimentally validated against the original brain T_1 MP2RAGE protocol and a reference T_1 mapping technique in a homemade phantom with water and gadolinium-based contrast agent. The experimental feasibility of a ME-MP2RAGE protocol for fat-water separation with 3-point Dixon was also verified. The fat-water separated T_1 mapping technique from the short T_1 ME-MP2RAGE protocol was then experimentally assessed with a second experiment and a homemade phantom with fat and water. Finally, an extensive quantitative assessment of the fat-water separated T_1 values calculated from the ME-MP2RAGE protocol and 3-point Dixon across a wide range of T_1 values was performed inside another homemade phantoms including different concentrations of gadolinium-based contrast agent and fat fractions.

The qualitative and quantitative assessments of the new short T_1 MP2RAGE protocol showed higher theoretical accuracy and precision than the original brain T_1 MP2RAGE protocol for the T_1 range of interest. Moreover, the T_1 values calculated from the short T_1 MP2RAGE showed a remarkably high correlation with the reference T_1 mapping technique whereas the feasibility of the ME-MP2RAGE protocol was also demonstrated experimentally. The second experiment demonstrated that the ME-MP2RAGE protocol with 3-point Dixon was suitable for precise and uniform fat-water separated T_1 mapping. With the final experiment, the fat T_1 values calculated from the ME-MP2RAGE protocol did not show any trend across different fat fractions and concentrations of gadolinium-based contrast agent whereas the water T_1 values showed an expected decrease with increasing concentrations of gadolinium-based contrast agent and smaller but noticeable decrease with increasing fat fractions.

In summary, the fat-water separated ME-MP2RAGE T_1 mapping technique presented in this thesis can easily and rapidly produce accurate and precise fat-water separated T_1 maps. Moreover, the precision level measured in fat T_1 values would make the technique suitable to measure variations in fat T_1 values due to the presence of oxygen. Once validated, this new technique could be used as a non-invasive technique to measure oxygen level in cancer tumors.

Résumé

Connaître le niveau d'oxygène à l'intérieur des tumeurs cancéreuses avant la radiothérapie peut affecter de manière significative le choix du traitement. Actuellement, le niveau d'oxygène *in vivo* avant la radiothérapie n'est pas mesuré parce aucune technique de référence simple existe. Des travaux récents en imagerie par résonance magnétique (IRM) ont indiqué que les variations dans les valeurs de T_1 du gras pourraient être utilisées comme méthode non invasive pour mesurer l'oxygénation des tissus. À cette fin, la séquence *Magnetization Prepared Two Rapid Acquisition of Gradient Echoes* (MP2RAGE) conçue pour la cartographie T_1 du cerveau et *3-point Dixon* pour effectuer la séparation gras-eau ont été combinées pour concevoir une nouvelle technique de cartographie T_1 séparée gras-eau.

Des évaluations et validations approfondies de l'exactitude et précision ont été effectuées pour développer le nouveau modèle multi-écho (ME) MP2RAGE. Tout d'abord, à partir d'une évaluation qualitative des paramètres d'acquisition de la séquence, le protocole MP2RAGE original développé pour des valeurs de T_1 entre 1000 ms et 2000 ms a été modifié pour être optimisé pour des valeurs de T_1 entre 200 ms et 800 ms. Ensuite, une évaluation quantitative de l'exactitude et précision théoriques du protocole MP2RAGE nouvellement conçu a été réalisée avec des simulations numériques servant à comparer avec le protocole original MP2RAGE. Par la suite, le nouveau protocole MP2RAGE a été validé expérimentalement avec le protocole MP2RAGE original et une technique de cartographie T_1 de référence à l'intérieur d'un fantôme fait maison avec de l'eau et un agent de contraste à base de gadolinium. La faisabilité expérimentale de la séparation gras-eau avec le protocole ME-MP2RAGE a également été vérifiée. La technique de cartographie T_1 séparée de l'eau et du gras produite par le protocole ME-MP2RAGE a ensuite été évaluée expérimentalement avec une deuxième expérience dans un fantôme fait maison avec du gras et de l'eau. Enfin, une évaluation quantitative approfondie des valeurs de T_1 séparées d'eau et de gras calculées avec le protocole ME-MP2RAGE a été réalisée à l'intérieur d'un autre fantôme maison comprenant différentes concentrations d'agent de contraste à base de gadolinium et de fractions de gras.

Les évaluations qualitatives et quantitatives du nouveau protocole MP2RAGE ont montré sa meilleure exactitude et précision théoriques pour la plage d'intérêt prédéfinie de T_1 en comparaison avec le protocole original MP2RAGE. De plus, les valeurs de T_1 calculées à partir du protocole MP2RAGE pour les courtes valeurs de T_1 ont montré une corrélation remarquablement élevée avec la technique de référence alors que la faisabilité expérimentale du protocole ME-MP2RAGE a aussi été démontrée. La deuxième expérience a démontré que le protocole ME-MP2RAGE avec 3-point Dixon produisait une cartographie T_1 séparée précise et uniforme du gras et de l'eau. Avec la troisième expérience, les valeurs de T_1 calculées du gras à partir du protocole ME-MP2RAGE n'ont montré aucune tendance particulière à travers les différentes fractions de gras et concentrations d'agent de contraste, tandis que les valeurs de T_1 de l'eau ont montré une diminution attendue avec l'augmentation de la concentration d'agent de contraste et une diminution moindre, mais perceptible avec l'augmentation des fractions de gras.

En résumé, la technique de cartographie T_1 séparée de l'eau et du gras venant du protocole ME-MP2RAGE présentée dans cette thèse peut rapidement produire des cartes T_1 séparées exactes et précises de l'eau et du gras. De plus, le niveau de précision mesuré dans les valeurs de T_1 du gras rendrait la technique appropriée pour mesurer les variations dans les valeurs de T_1 du gras dues à la présence d'oxygène. Une fois validée, cette nouvelle technique pourrait être utilisée pour mesurer de façon non-invasive le niveau d'oxygène dans les tumeurs cancéreuses.

List of Figures

Chapter 2

Chapter 3

Chapter 4

List of Tables

Chapter 3

Chapter 4

Abbreviations

$\mathbf{B_0}$	Main static magnetic field
$\mathbf{B_1}$	Excitation pulse
$\mathbf{B_{eff}}$	Effective magnetic field
CI	Confidence Interval
FID	Free Induction Decay
FT	Fourier Transform
GBCA	Gadolinium-Based Contrast Agent
[GBCA]	Concentration of GBCA
GRAPPA	GeneRalized Autocalibrating Partial Parallel Acquisition
GRE	Gradient-Recalled Echo
invEff	Inversion Efficiency
IP	In-phase
IR	Inversion Recovery
M	Net Magnetization vector
ME	Multi-Echo
MRI	Magnetic Resonance Imaging
MRS	Magnetic Resonance Spectroscopy
$\mathbf{M_{xy}}$	Transverse Magnetization
$\mathbf{M_z}$	Longitudinal Magnetization
NMR	Nuclear Magnetic Resonance
OP	Out-of-phase
PF	Partial Fourier
PI	Parallel Imaging
qMRI	Quantitative MRI
QSM	Quantitative Susceptibility Mapping
RAGE	Rapid Acquisition of Gradient Echoes
RF	Radio-frequency

SE	Spin Echo
SENSE	SENSitivity Encoding
T	Tesla
TE	Echo Time
TI	Inversion Time
TR	Repetition Time

Chapter 1

Introduction

1.1 Motivation

Magnetic resonance imaging (MRI) is an imaging modality used for a wide variety of applications. Due to its extensive possibilities of contrast, MRI is of interest for diagnostic imaging but also relevant for treatment planning [1]. More precisely, several applications like Dynamic Contrast Enhanced MRI (DCE-MRI) and Diffusion-Weighted MRI (DW-MRI) have been found to be useful in radiotherapy treatment planification and monitoring of tumor response [2]. Moreover, measurement of relaxation parameters like the longitudinal (or T_1) relaxation time constant can non-invasively help to determine brain tumor types [3]. The development of quantitative metrics from MR images like T_1 is known as quantitative MRI (qMRI) and groups a wide variety of techniques.

In radiotherapy, the oxygen level inside cancer tumors was shown to play a significant role in tumor response to treatment [4]. The current gold standard for measuring oxygen levels inside tumor habitats is the insertion of an oxygen electrode which is a long and invasive procedure which is normally not performed due to its considerable impact on the clinical workload [5]. On the other hand, MRI has shown promise with specific applications to non-invasively measure the oxygen levels *in vivo* with techniques like blood oxygen level-dependent (BOLD) MRI or injection of fluorinated agent with a T_1 sensitive to oxygen [6]. However, these techniques are either specific to a single application or require a specialized contrast agent not readily available in clinical situations. Measuring oxygen level with MRI is also known as MR-Oximetry. Recent works in the literature [7] suggested that T_1 measured from fat signal was particularly affected by the quantity of oxygen present in the fat. Consequently, variations in fat T_1 values have been

proposed as an indirect quantitative metric to non-invasively measure the oxygen level *in vivo*. However, producing accurate and precise fat specific T_1 maps is not something readily done yet in qMRI. Currently, most T_1 mapping techniques used cannot differentiate signal from various chemical species like fat and water. Thus, the T_1 maps produced are said to be "global" T_1 maps.

1.2 Objectives

The aim of this work was to develop a novel T_1 mapping technique to produce accurate and precise fat-specific T_1 maps optimized for a short T_1 values. Ultimately, the proposed novel fat T_1 mapping technique could be used to evaluate variations in fat T_1 due to the presence of oxygen and serve as a technique to non-invasively measure oxygen levels in cancer tumors, in particular for radiotherapy treatment planning. It was hypothesized that a version of the well-known T_1 mapping technique using MP2RAGE [8] modified with three echoes [9] and shorter sensitive T_1 range could be combined with a robust fat-water separation technique like 3-point Dixon [10] to produce three distinct T_1 maps: the global, water-specific, and fat-specific T_1 maps. Moreover, it was speculated that the modified MP2RAGE protocol would be more accurate and precise for shorter T_1 values than the original implementation for brain T_1 mapping. Once validated, this new, rapid, and simple protocol will produce highly precise fat T_1 maps and could be easily implemented into radiotherapy treatment planning as a non-invasive hypoxia measurement tool which is not a tool currently available for radio oncologists.

1.3 Thesis Outline

This thesis is composed of 6 chapters as explained below.

Chapter 2 presents the necessary background information required to understand the work presented in this thesis. A broad overview of the basic MR concepts is presented first. This general overview of basic MR concepts is then followed by a selected variety of topics in quantitative MRI related and necessary to understand the project. More precisely, T_1 mapping and fat-water separation are explained extensively.

Chapter 3 introduces the methodology used for the realization of this project. This chapter is separated in several subsections related to different experiments performed during this project. It starts with the methodology used for the optimization of the MP2RAGE protocol for short T_1 values followed by a section about the numerical simulations used to assess the theoretical accuracy and precision of the newly designed MP2RAGE protocol. Afterwards, the next three subsections present the methodology used to (1) experimentally validate the new short T_1 MP2RAGE T_1 mapping protocol against a reference T_1 mapping technique, (2) experimentally assess the quality of the fat-water separated T_1 mapping from the ME-MP2RAGE sequence and (3) quantitatively assess the fat-water separated T_1 mapping from the ME-MP2RAGE sequence across a wide range of T_1 values.

Chapter 4 presents the results produced during the project whereas chapter 5 presents the discussion of the results. Chapter 4 and 5 are separated into sections that mirror the methods presented in Chapter 3.

Chapter 6 presents the conclusion of the thesis. In this chapter, the thesis is summarized, and future research pathways are presented.

Chapter 2

Background

This chapter is an overview of the fundamental concepts and physics behind MRI that are necessary to understand the rest of the work. The chapter is divided into three main sections where the fundamental concepts behind MRI, T_1 mapping, and fat-water separation are explained, respectively.

2.1 Fundamentals of MRI

Section 2.1 presents the basic concepts necessary to understand MRI and is an adaptation of Chapters 4 and 5 of D. Nishimura book *Principles of Magnetic Resonance Imaging* [11] and Chapters 11 and 14 of the *Handbook of MRI pulse sequences* from M. Bernstein, K. King and X. Zhou [12].

Section 2.1 approaches MRI with a classically oriented point-of-view. However, to thoroughly explain MRI, quantum mechanics are required. Thus, the concepts shown in this chapter are mostly using classical mechanics and quantum mechanics when required.

2.1.1 Nuclear spin

In MRI, the most fundamental concept to understand is the concept of spin of atomic nuclei. Every elementary particle such as the proton, the neutron, and the electron possesses a spin. The spin is an intrinsic property like mass or charge. For charged particles like the proton, the spin has two intrinsic properties to the particle: an angular momentum and a magnetic moment. A visual representation of the concept of spin for a proton is shown on Figure 2.1. To simplify the

peculiar concept of spin, a particle with a non-zero spin can be compared to a small bar magnet (magnetic moment) spinning on itself (angular momentum). More precisely, the magnetic moment is induced by the charge of the particle itself as described by Faraday's law of induction.

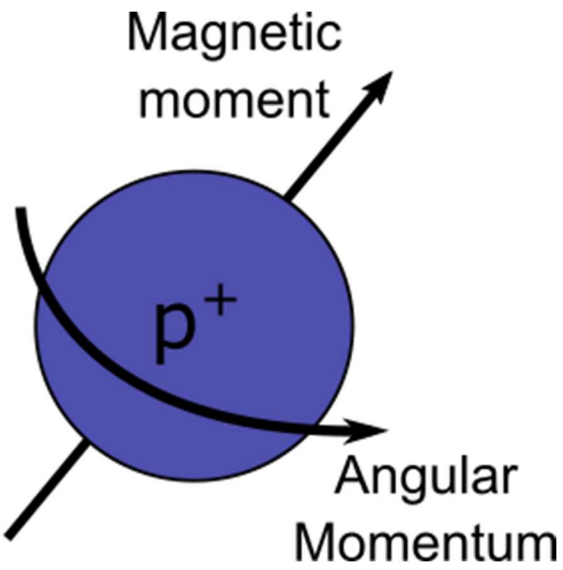

Figure 2.1 *- Illustration of a proton with its spin creating an angular momentum and magnetic moment.*

All atomic nuclei with an odd number of nucleons will possess a non-zero spin whereas nuclei with an even number of nucleons will always possess a total spin of zero. The most used atomic nucleus in MRI is by far the hydrogen nucleus because it is composed of one proton (spin: ± 1/2) and because it is excessively abundant inside the human body inside molecules like water (H_2O) or fat (triglycerides). Ultimately, the human body can be seen as a sum of an extraordinarily large quantity of minuscule bar magnets.

2.1.2 Nuclear Magnetic Resonance

In the absence of an external magnetic field, the magnetic moments of hydrogen nuclei inside the body are randomly oriented. The small magnetic fields cancel out together to produce a net magnetization of zero. The net magnetization vector **M** is the vector sum of all the magnetic moment vectors (**μ**) per volume V. It can be described with the following equation:

$$\mathbf{M} = \frac{1}{V}\sum_{n=0}^{N} \boldsymbol{\mu} \qquad \textit{Eq. 1}$$

In the presence of a static magnetic field $\mathbf{B_0}$, all the magnetic moments of hydrogen nuclei align in the direction of $\mathbf{B_0}$ either in a parallel or anti-parallel manner and precess at a well-defined frequency around the $\mathbf{B_0}$ axis (called the longitudinal direction). The fact that all magnetic moments are aligned either in parallel or anti-parallel with a small excess in the parallel state will create a non-zero net magnetization vector at equilibrium $\mathbf{M_0}$ in $\mathbf{B_0}$ direction.

From quantum mechanics principles, two discrete states are possible for ±1/2 spins and they are described as two discrete energy levels: the low energy level corresponding to the parallel state and the high energy level corresponding to the anti-parallel state. The number of magnetic moments in both energy levels can be described by the Boltzmann distribution derived from statistical mechanics. At the human body temperature, the Boltzmann distribution predicts a minuscule excess of magnetic moments in the parallel state compared to the anti-parallel state, creating the $\mathbf{M_0}$ oriented in the longitudinal direction. By convention, the longitudinal direction is associated with the z-direction. Thus, $\mathbf{M_0}$ only possesses a z-component at equilibrium and no x- or y-component.

As mentioned two paragraphs above, spins subject to a static magnetic field will precess around the $\mathbf{B_0}$ axis (or z-axis). The precession exists because $\mathbf{B_0}$ introduces a torque on the spins that applies a force which results in a rotation of spins perpendicularly to $\mathbf{B_0}$ and $\mathbf{M_0}$ (i.e., a rotation in the x-y plane). The well-defined precession frequency of the spins is called the Larmor frequency (f_0 or its angular equivalent ω_0) and can be described with the following equations:

$$\omega_0 = \gamma B_0 \qquad \textit{Eq. 2}$$

$$f_0 = \frac{\gamma}{2\pi} B_0 \qquad \textit{Eq. 3}$$

where γ is the gyromagnetic ratio in MHz/T, which is a constant specific to every atomic nucleus and the strength of the static magnetic field applied $\mathbf{B_0}$ in *tesla* (T). For instance, the hydrogen nucleus has a well-known $\gamma/2\pi$ value of 42.58 MHz/T [11].

Signal in MRI is created by manipulating $\mathbf{M_0}$ in a precise manner. By applying a radiofrequency (RF) pulse, it is possible to tip $\mathbf{M_0}$ by a certain angle θ or α (called the flip angle) away from $\mathbf{B_0}$ axis and towards the transverse plane (the x-y plane). In fact, the RF pulse produces a weak, time-varying and rotating magnetic field called $\mathbf{B_1}$, which is applied perpendicular to $\mathbf{B_0}$. It is important to mention that $\mathbf{M_0}$ is not rotating around $\mathbf{B_0}$ axis at equilibrium because it is perfectly aligned with $\mathbf{B_0}$ but will start rotating at Larmor frequency after being perturbed (do not forget that $\mathbf{M_0}$ is the sum of individual precessing spins). The perturbation of $\mathbf{M_0}$ by $\mathbf{B_1}$ is called the excitation and is shown in Figure 2.2.

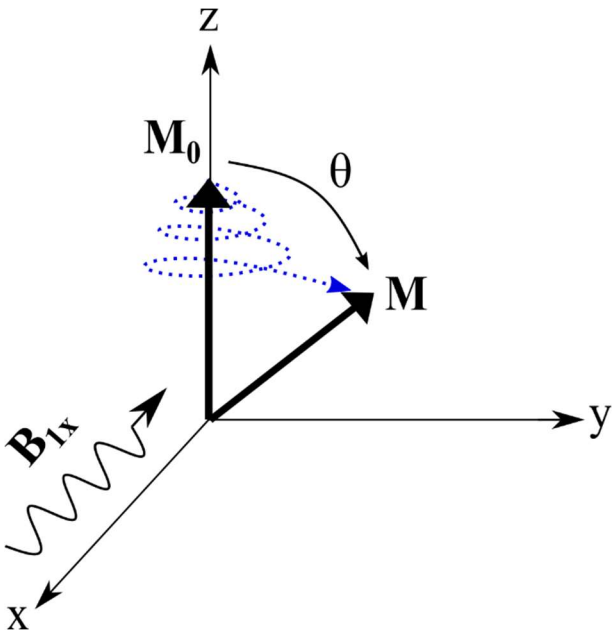

Figure 2.2 *- Excitation of $\boldsymbol{M_0}$ by a short time-varying magnetic field $\boldsymbol{B_1}$ in the transverse plane. The resulting **M** is tipped towards the transverse plane (perpendicular to $\boldsymbol{M_0}$ and $\boldsymbol{B_1}$) by an angle θ called the flip angle.*

There are two important points to maximize the perturbation created by $\mathbf{B_1}$: the direction and frequency of the perturbation. If the $\mathbf{B_1}$ is perpendicular to $\mathbf{B_0}$ and has a frequency equal to the Larmor frequency (i.e., $\omega_1 = \omega_0$), the torque applied to $\mathbf{M_0}$ will be maximized. The perturbation performed while respecting these conditions in addition with the detection of the signal produced is known as nuclear magnetic resonance (NMR). Thus, in MRI, the fundamental principle used to create signal is NMR from hydrogen nuclei inside the human body. Different types of excitations exist in MRI and the most relevant for this work will be presented in section 2.1.7.

Once $\mathbf{M_0}$ is tipped towards the transverse plane, it is no longer in an equilibrium state, and it possesses a component in that plane called the transverse magnetization or $\mathbf{M_{xy}}$. $\mathbf{M_{xy}}$ is the complex vector combination of the magnetization in the x and y directions (i.e., $\mathbf{M_{xy}}(t) = \mathbf{M_x}(t) + i\,\mathbf{M_y}(t)$). Thus, after excitation, $\mathbf{M_0}$ becomes $\mathbf{M}$ which is a sum of the longitudinal ($\mathbf{M_z}$) and transverse ($\mathbf{M_{xy}}$) components. The flip angle θ is determined by the duration τ and amplitude of the $\mathbf{B_1}$ pulse as shown with the following equation:

$$\theta = \int_0^{\tau} \omega_1(t)dt = \int_0^{\tau} \gamma B_1(t)\, dt \qquad \textit{Eq. 4}$$

It is possible to detect the NMR signal produced by the rotating $\mathbf{M}$ after the excitation pulse by carefully positioning a receiver coil in the transverse plane. The signal detection is possible due to Faraday's law of electromagnetic induction. More precisely, an alternating current will be induced in the receiver coil (conductive loop) by the magnetic field created from the rotating $\mathbf{M_{xy}}$ passing through it. This signal produced directly after excitation is known as the Free Induction Decay (FID).

2.1.3 Relaxation

After the excitation, spins return to their equilibrium state aligned with $\mathbf{B_0}$ by releasing the energy gained from the excitation. This recovery process in NMR is known as relaxation and is due to two mechanisms: (1) energetic transitions of spins from the high energy level (anti-parallel state) to the low energy level (parallel state) and (2) spin dephasing in the transverse

plane. Specifically, there are two different types of relaxation: the longitudinal (T_1) and transverse (T_2) relaxation. Both relaxations are explained in detail in sections 2.1.3.1 and 2.1.3.2 respectively.

2.1.3.1 T_1 relaxation

The T_1 relaxation or spin-lattice relaxation is the process whereby $\mathbf{M_z}$ returns to its initial value ($\mathbf{M_0}$) aligned with $\mathbf{B_0}$ after $\mathbf{B_1}$ excitation. As the name says, the T_1 relaxation is due to the exchange of energy between the excited spins and their surrounding environment (i.e., lattice). This process follows an exponential recovery that is described by the following equation:

$$\mathbf{M_z} = \mathbf{M_0} + \left(\mathbf{M_{z(0)}} - \mathbf{M_0}\right)e^{\frac{-t}{T_1}} \qquad \textit{Eq. 5}$$

Where t is the time after the excitation, $\mathbf{M_0}$ the net magnetization vector at equilibrium, $\mathbf{M_{z(0)}}$ the longitudinal magnetization directly after the excitation and T_1 the time constant related to the longitudinal relaxation. More precisely, the T_1 constant is the time required for $\mathbf{M_z}$ to recover $1/(1 - e)$ (or ~63%) of its equilibrium value. The T_1 relaxation can be shown with Figure 2.3. The T_1 time constant is an intrinsic property of all materials including human body tissues and is dependent on the strength of $\mathbf{B_0}$. Several techniques exist to measure T_1 values, and the techniques relevant to this work will be presented in section 2.2.

Frequently, the relaxation rate R_1 instead of the relaxation time T_1 is used. R_1 corresponds to the inverse of T_1 (i.e., $R_1 = 1/T_1$). R_1 values measured are linearly dependent on the concentrations of gadolinium-based contrast agent (GBCA) used [13]. Contrast agents in MRI most commonly contain gadolinium due to its powerful paramagnetic properties that considerably increase the T_1 relaxation rate (or R_1) of water protons [14]. More information about gadolinium-based contrast agents can be found in [14]. The slope of the linear increase of R_1 values against concentrations of GBCA is known as the relaxivity or r_1 of the contrast agent [14]. The relaxivity value is temperature dependent and different for every brand of contrast agent available.

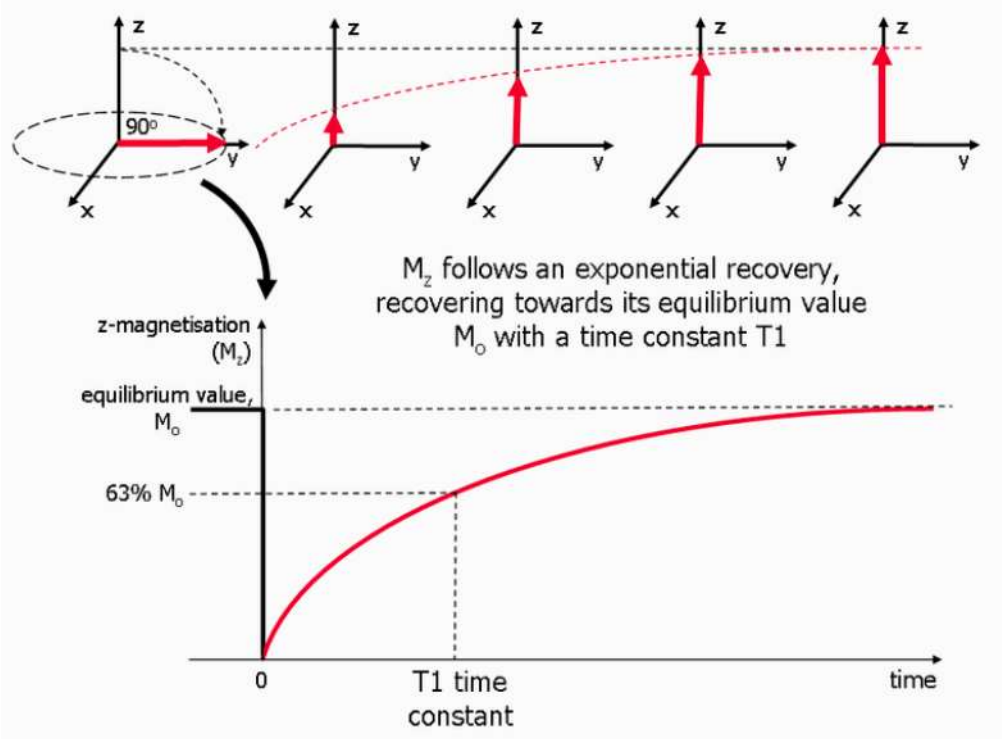

***Figure 2.3** - Illustration of the longitudinal (T_1) relaxation after a 90º excitation of the magnetization. The T_1 time constant is also shown. Figure reproduced from* [60]*, with permission.*

2.1.3.2 T_2 relaxation

The T_2 relaxation or spin-spin relaxation is the process whereby $\mathbf{M_{xy}}$ decays after the excitation pulse. As said in section 2.1.2, the excitation pulse creates a $\mathbf{M_{xy}}$ component by tipping $\mathbf{M_0}$ into the transverse plane. In addition, the $\mathbf{B_1}$ excitation pulse puts all excited spins in phase (creates a phase coherence). The random interactions between individual and adjacent spins in the transverse plane result in the destruction of the phase coherence seen directly after excitation pulse. It is the loos of phase coherence that ultimately produces the $\mathbf{M_{xy}}$ decay. The T_2 relaxation follows an exponential decay and is described with the following equation:

$$\mathbf{M_{xy}} = \mathbf{M_0} e^{\frac{-t}{T_2}} \qquad \textit{Eq. 6}$$

where *t* is the time after the excitation and T_2 the time constant related to the transverse relaxation. Specifically, T_2 is the time required by $\mathbf{M_{xy}}$ to reach (1/e) (or ~37%) of its initial value directly after the excitation. In opposition with T_1, T_2 is mostly independent of the static field strength. Visually, T_2 relaxation can be described with Figure 2.4. As for T_1 relaxation, the relaxation rate R_2 corresponds to the inverse of the relaxation time T_2 (i.e., $R_2 = 1/T_2$).

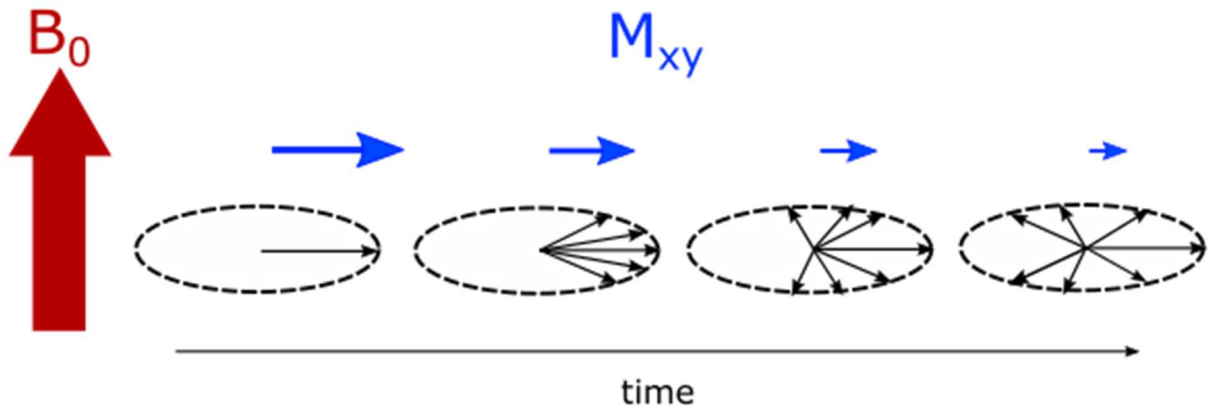

Figure 2.4 *- T_2 relaxation process after $\mathbf{B_1}$ excitation. The dephasing of individual spins (black arrows) in the transverse plane results in the decay of $\mathbf{M_{xy}}$ (blue arrow) with time.*

It is important to specify that in MRI or NMR experiments, $\mathbf{M_{xy}}$ decays considerably faster than what is predicted from the theory. The T_2 values measured are an "effective" T_2 called T_2* ("T_2-star"). T_2* is a combination of the "true" T_2 and transverse relaxation effects resulting from inhomogeneities in the main magnetic field $\mathbf{B_0}$ called T_2' ("T_2-prime"). These inhomogeneities are coming from defects in the magnet itself or field distortions due to susceptibility effects in the tissue or object imaged. T_2* is defined with the following equation:

$$\frac{1}{T_2^*} = \frac{1}{T_2} + \frac{1}{T_{2'}} \qquad \textit{Eq. 7}$$

Where T_2^* is the effective or measured T_2, T_2 the true T_2, and T_2' the additional relaxation due to inhomogeneities.

2.1.4 MR Signal

The raw MR signal is a complex signal detected in quadrature. The quadrature detection of MR signal enables the possibility to know the exact intensity (or magnitude) and direction (or phase) of **M** in the transverse plane. The quadrature detection of MR signal can be seen as two coils positioned perpendicularly to each other with coils representing two different "channels": one real (*Re*) and one imaginary (*Im*). Therefore, it is possible to represent MR signal as a complex signal with a real (*Re*) and imaginary (*Im*) component. Nowadays, MR scanners do not use two orthogonal coils to detect signal. Sophisticated coil designs are used and the physical principles explaining their functioning are out of the scope of the current work. However, the fundamental principle of quadrature detection is still used and valid for those sophisticated coils. Therefore, the complex MR signal (S(t)) can be described with the two following equivalent equations:

$$\mathrm{S(t)} = Re(\mathrm{S(t)}) + \mathrm{i}\, Im(\mathrm{S(t)}) \qquad \textit{Eq. 8}$$

$$\mathrm{S(t)} = \mathrm{Mag(t)} \times \mathrm{e}^{\mathrm{i}\phi(\mathrm{t})} \qquad \textit{Eq. 9}$$

where *i* is the imaginary number, Mag the magnitude of the complex signal ($\mathrm{Mag(t)} = \sqrt{\mathrm{Re(S(t))}^2 + \mathrm{Im(S(t))}^2}$) and φ the phase ($\phi = \arctan\left(\frac{Im}{Re}\right)$). In clinical situations, the magnitude image is usually used to give a diagnosis. However, the phase can give valuable information for certain applications of qMRI like Quantitative Susceptibility Mapping (QSM).

2.1.5 Spatial encoding of MR signal

Once we know raw MR signal is complex, it is important to know also how MR signal is spatially encoded. Spatial encoding of MR signal is done by applying a combination of linearly varying gradient fields inside the volume of interest. More precisely, these gradient fields introduce spatially linear variations in the precession frequency of the spins ω(x,y) felt by the spins. By looking at Eq. 2, it can be observed that a variation in the magnetic field **B** will

automatically produce a variation in the precession frequency of the spins. Thus, spins that were originally precessing at Larmor frequency (ω_0) because they were only subject to $\mathbf{B_0}$ are now precessing at a slightly different frequency $\omega(x,y)$ due to the new effective magnetic field ($\mathbf{B_{eff}}$) felt by the spins based on their spatial localization.

In total, three gradient field are applied to create linear variations in all physical directions (i.e., x, y, and z). The linear variations introduced in spatial precession frequencies depend on the amplitude of the gradient fields. It is common in MRI to call the three gradients the slice-selective gradient, phase-encoding gradient, and frequency-encoding or readout gradient. As the name says, the slice-selective gradient (in combination with $\mathbf{B_1}$) is used to selectively excite the spins inside a precise 2D plane inside the volume of interest. The phase-encoding and frequency-encoding gradients are used to modify the phase and frequency of the spins for two distinct directions inside the selected excitation plane or volume respectively.

The sophisticated way of encoding MR signal is not the most intuitive concept. The spatial variations introduced in the phase and frequencies of the spins are the basis of spatial encoding of the complex MR signal. The complex MR signal is encoded in something called “k-space”. Specifically, the k-space is a frequency space representing the spatial frequencies in the MR images which corresponds to the Fourier domain mathematically and is defined with three axes: k_x, k_y and k_z. It is important to point out that a k-space point (k_x, k_y, k_z) do not have a one-to-one relationship with a spatial position (x, y, z) in the image. The main point to know about MRI signal encoding is that at any given time, the MR signal corresponds to the Fourier transform of the spatial distribution of the magnetization (or spins) determined by the linear variations created from time-varying gradients. The simplest way to understand MR signal encoding is to see the application of gradients as a way to move through different locations in the k-space. For instance, by applying a phase-encoding gradient of a certain amplitude and duration in the k_y direction, a k_y value will be selected. Then, a frequency-encoding or readout gradient will be applied to acquire the complete k_x line at the k_y value determined by the phase-encoding gradient before. By repeating this process several times for different values of phase-encoding gradient, it is possible to fill the 2D k-space. The complete 3D k-space is acquired by repeating the combination of phase- and frequency-encoding gradients for different values of slice-selective

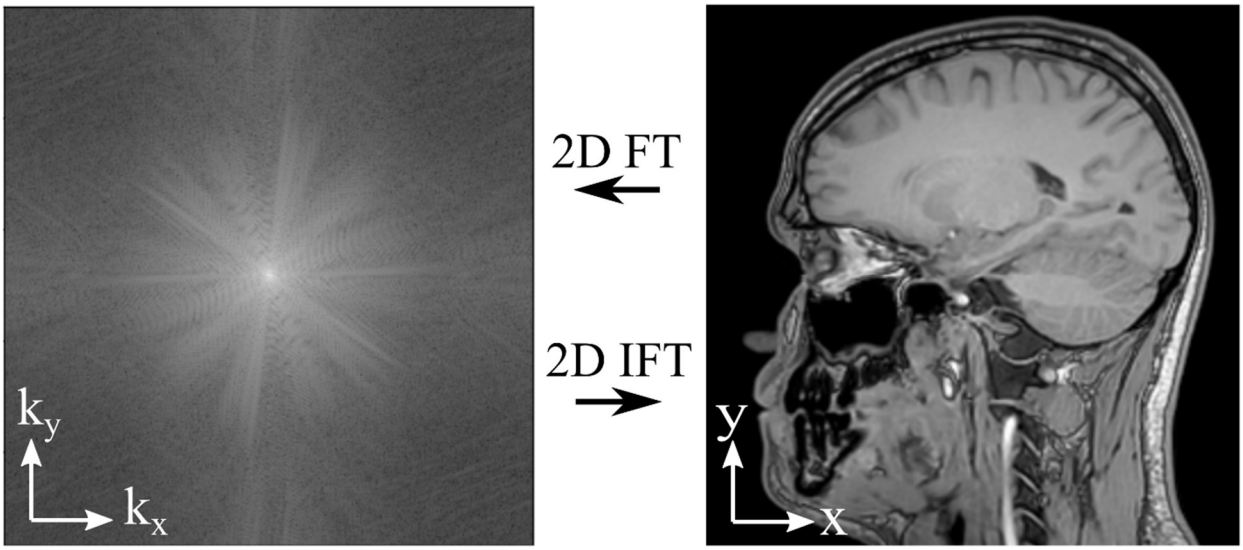

Figure 2.5 *- 2D k-space (left) and the correspond 2D MR image (right). The mathematical transformations required to go from the image space to k-space and vice-and-versa are shown between the two images.*

gradient. It is important to mention that the association of phase-encoding gradient with k_y direction and frequency-encoding with k_x is purely arbitrary and is determined by the MR system operator. Once the k-space is filled, a mathematical transformation called the Inverse Fourier Transform (IFT) is applied to transform the information contained in k-space into the final MR image. Conversely, to go from the image space to the k-space, the Fourier Transform (FT) is applied. An example of a 2D k-space and its corresponding 2D MR image with the transformation processes necessary to change from the k-space to the image space (and vice-and-versa) are shown on Figure 2.5. A more detailed and complete description of spatial encoding in MRI can be found in chapter 5 of [11].

2.1.6 K-space acceleration techniques

The k-space has special properties like the conjugate (or Hermitian) symmetry. This symmetry is only valid if the real part of the k-space is even and the imaginary part odd. It is theoretically possible to reconstruct an image by acquiring only half of the k-space because the missing data points can be inferred from the other encoded half. This process of partly acquiring the k-space is known as Partial Fourier (PF). In practice, due to phase errors from various sources like $\mathbf{B_0}$

inhomogeneities, the minimum part of k-space that can be acquired is slightly more than half of k-space. By acquiring slightly more k-space data, it is possible to account for the phase errors. Typical fractions of k-space acquired are 5/8, 6/8 or 7/8 when PF is enabled.

Moreover, it is possible to undersample the k-space in a predefined encoding scheme. However, if someone would decide to acquire every other k-space line (k_y or k_x), it would result in aliasing in the undersampled direction of the final image. The minimum sampling rate of k-space directions is defined by the Nyquist criterion which states that the sampling rate must be larger or equal to two times the highest (spatial) frequency. More details can be obtained in Chapter 5 of [11]. On the other hand, it is possible to get around aliasing by acquiring the data from multiple receiving coils around the volume of interest. This process of undersampling the k-space while acquiring the signal from multiple receiving coils is known as Parallel Imaging (PI). Each individual coil independently measures the signal in parallel and is sensitive to different regions inside the imaging volume. The complex signal from each individual coil is then recombined to produce the final unaliased image. The two main PI techniques in MRI are SENSE [15] and GRAPPA [16]. Both techniques differ on how the missing information is recovered. SENSE is said to be an “image-based” PI technique since the reconstruction and unfolding of the aliased images take place in the image space whereas GRAPPA is said to be a “k-space based” technique because the reconstruction (or calculation of the missing information) takes place in k-space. More details about these two PI techniques can be found in [15] and [16] respectively.

In the end, the main reason why PF or PI is applied is to reduce scan time, which can be prohibitively long depending on the acquisition. For instance, with PI, acceleration factors (R) around 4 or 5 can be seen [17]. Scan time is reduced by a factor of R directly or close to R depending on the PI technique. However, choosing an unreasonably large R value results in the decrease of the quality of the resulting images. Specifically, Signal-to-Noise Ratio (SNR) is automatically degraded by a factor of the square root of R for both techniques in addition to spatially dependent noise being increased by a factor related to the g-factor. More details can be found in [17]. Therefore, using PI or PF is always a tradeoff between scan time and image quality.

2.1.7 MR sequences

As written in section 2.1.2, the MR signal produced directly after the $\mathbf{B_1}$ excitation pulse is the FID. However, FID alone is not frequently used produce MR images. The two most common ways to produce signal in MRI are named Gradient-Recalled Echo and Spin Echo and will be described in the sections 2.1.7.1 and 2.1.7.2, respectively.

2.1.7.1 Gradient-Recalled Echo (GRE)

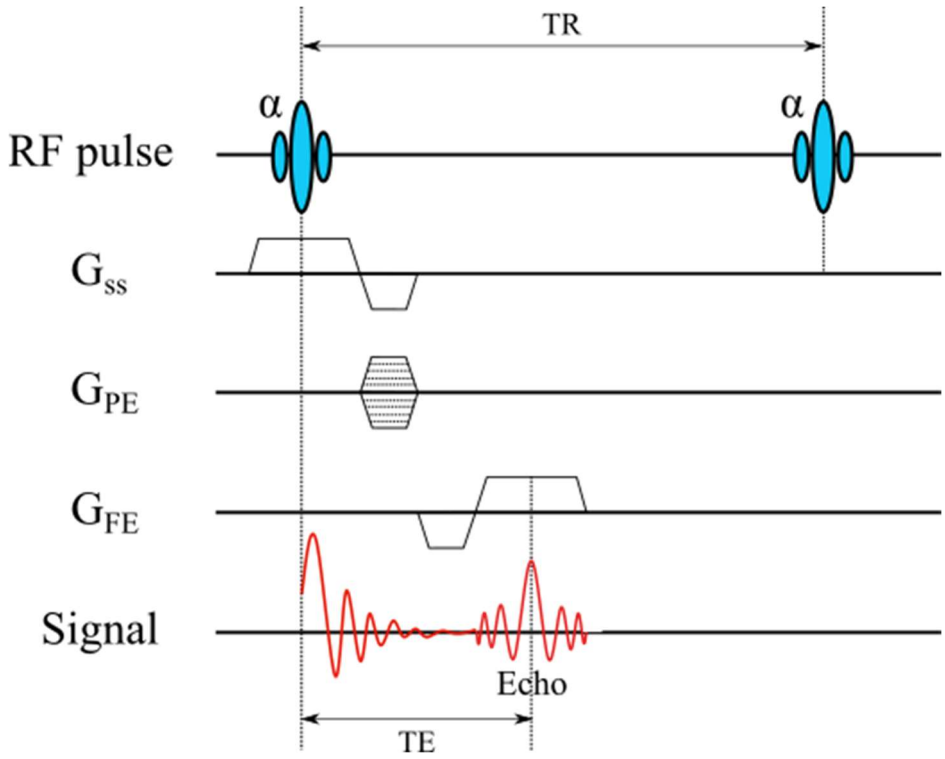

***Figure 2.**6 - Example of a GRE pulse sequence. α corresponds to the flip angle. G_{ss}, G_{PE} and G_{FE} correspond to the slice-selective, phase-encoding and frequency-encoding or readout gradients respectively. The GRE is created by the dephasing (negative lobe) and rephasing (positive lobe) of the frequency-encoding gradient.*

A Gradient-Recalled Echo (GRE) is a MR signal produced from an "echo" of the magnetization generated by the manipulation of gradient fields. Thus, to produce a GRE, a RF pulse ($\mathbf{B_1}$) is used to excite the magnetization with a readout gradient composed of a dephasing lobe first and a rephasing lobe afterwards. This is presented on Figure 2.6. The process of defocusing the spins

can be seen as moving towards the left extremity of a horizontal k-space line. Then, the refocusing lobe is used to move towards the other right extremity of the same k-space line. Ultimately, the dephasing gradient lobe destroys the phase coherence of spins after the excitation whereas the refocusing lobe refocuses the spins to create a Gradient-Recalled Echo. By choosing a dephasing gradient lobe with half the size of the rephasing gradient, the echo produced is maximized when the k-space center is crossed. The gradient used to dephase and rephase the magnetization is the frequency-encoding or readout gradient.

As seen on Figure 2.6, the repetition time (TR) is the time between two successive RF pulses while the echo time (TE) is the time between the RF pulse and the echo produced mutually from the excitation pulse and gradient reversal. The RF pulse normally produces an excitation with a flip angle (α) between 0º and 90º. GRE sequences are frequently used in MRI due to their ability to rapidly acquire the data. In fact, by using small α values (i.e., < 10º), the T_1 recovery period of spins is considerably short. Ultimately, that gives the possibility to reduce the TR which is directly linked to scan time. If TR >> T_2^*, the GRE signal can be modeled with the following equation:

$$\text{Signal} \propto \sin(\alpha)\left(\frac{1-e^{-\frac{TR}{T1}}}{1-e^{-\frac{TR}{T1}}\cos(\alpha)}\right)e^{-\frac{TE}{T2*}} \qquad \textit{Eq. 10}$$

where α is the flip angle value in degrees, T_1 and T_2^* the relaxation time constants described in section 2.1.3. By choosing different combinations of α, TE and TR, it is possible to produce different signal weightings in MR images. For instance, a T_1 weighted image (T_{1w}) is an image where most of the image contrast is due to differences in T_1 relaxation between the tissues.

It is possible to acquire more than one echo with GRE sequences. A multi-echo (ME) GRE sequence is nearly identical to a single echo GRE except that the readout gradient is multiplied N times for N echoes. Thus, the spins are defocused and refocused N times. Due to T_2^* relaxation, longer echoes have lower intensity resulting in less signal detected.

2.1.7.2 Spin Echo (SE)

From Eq. 10, it can be observed that GRE signal is dependent on T_2^* relaxation and not T_2. This is because the refocusing lobe of the GRE sequence does not cancel the T_2 relaxation due to magnetic inhomogeneities or susceptibility effects (T_2'). It is possible to cancel these unwanted effects by applying a refocusing pulse of 180º after an initial excitation pulse of 90º. The combination of excitation and refocusing pulses in this particular order (i.e., a 90º pulse followed by a 180º) produces an echo called a spin echo (SE). As explained in section 2.1.3.2, spins lose phase coherence (or dephase) after the excitation pulse. By adding the 180º pulse afterwards, it cancels the spin dephasing due to inhomogeneities and susceptibility effects (T_2') while not cancelling the dephasing due to T_2 relaxation. A typical SE imaging pulse sequence is shown on Figure 2.7.

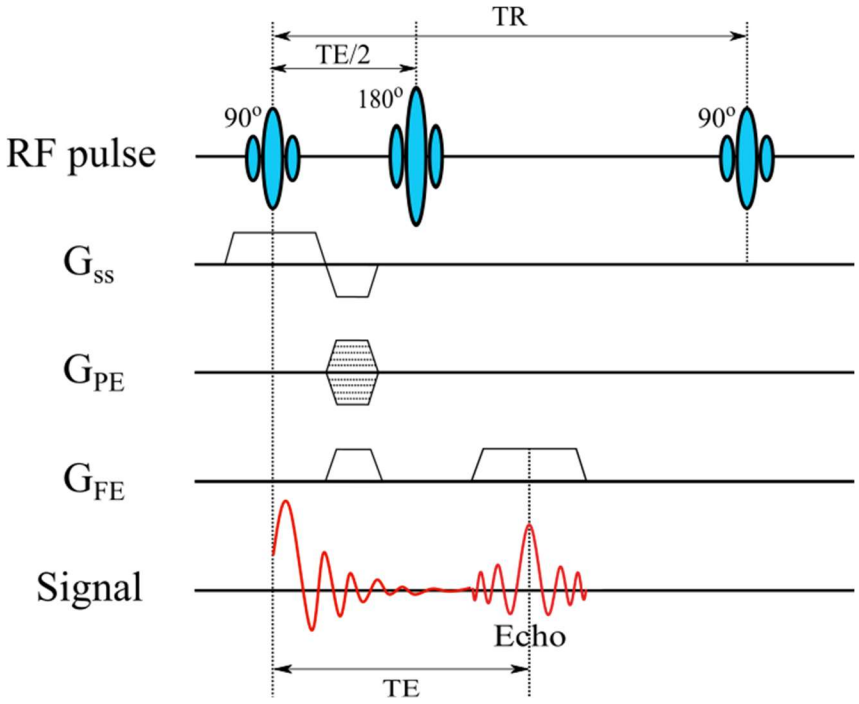

Figure 2.7 *- Example of a SE imaging pulse sequence. Flip angles are always 90º and 180º for the excitation and refocusing pulses respectively. The first lobe of the frequency-encoding or readout gradient can be inverted and placed between the excitation and refocusing pulses to gain time as shown in the pulse sequence diagram.*

As seen in Figure 2.7, it is possible to place the phase-encoding and first lobe of the readout gradients before the 180º to save time. In a SE sequence, TR is the time between two successive *excitation* pulses whereas TE is two times the duration between the *excitation* and refocusing pulses.

The main advantage of SE sequences is the robustness to $\mathbf{B_0}$ inhomogeneities and susceptibility effects because the refocusing pulse cancels most of these two effects. Consequently, SE is suited for measurements of T_2 (unlike GRE). The SE signal equation is a simplified version of GRE (Eq. 10) where $\alpha=90^{\circ}$ and T_2^* is replaced by T_2 (and assuming $TR >> T_2$). Like GRE sequences, SE sequences can have different contrast weightings based on the values of TE and TR. In addition, SE sequences can be extended to ME acquisitions by adding well positioned *refocusing* pulses after the first one.

2.2 Quantitative MRI: T_1 mapping

MR physicists have been developing quantitative metrics from MR images to help with diagnosis [1] and even treatment planning [2]. The work yielded a new branch to MRI known as quantitative MRI (qMRI). qMRI is a broad field that includes all types of studies that include the production of quantitative maps of any physical or physiological parameters of tissues from MR images.

For instance, it is possible to produce quantitative maps of the T_1 time constant and compare the T_1 values between different tissues. These maps are called T_1 maps and the process of producing them is known as T_1 mapping. Evaluating T_1 values for different anatomical regions can be an interesting biomarker to detect pathologies [18], [19].

Several techniques exist to produce T_1 maps, and each technique possesses its own advantages and disadvantages. That results in T_1 mapping techniques being used for a variety of applications where the disadvantages can be reduced significantly or bypassed. The main T_1 mapping techniques relevant for this work are presented in sections 2.2.1, 2.2.2 and 2.2.3.

2.2.1 Inversion Recovery (IR)

Inversion recovery (IR) T_1 mapping is considered the reference T_1 mapping technique [20]. IR consists of inverting the equilibrium magnetization $\mathbf{M_0}$ with a 180° inversion pulse (i.e., $\mathbf{M_z}$ becomes $\mathbf{-M_z}$) before acquiring the signal after a time delay called the inversion time (TI). More precisely, the TI corresponds to the time between the inversion and excitation pulses ($0° < \theta \leqslant 90°$). In opposition with SE, the 180° pulse is *before* the excitation pulse. Both GRE and SE acquisitions can be used for IR T_1 mapping.

By repeating the process of inverting the magnetization and acquiring the signal at different TIs, acquisitions happen at different moments on the T_1 recovery process of the magnetization. Therefore, exponential fitting of the signal values acquired can be performed to reproduce the T_1 relaxation curve of the magnetization and ultimately calculate the T_1 value associated with the T_1 relaxation curve. An example of a breath-hold IR-based T_1 mapping technique for cardiac quantitative imaging is shown on Figure 2.8.

IR T_1 mapping techniques have several benefits. First, IR T_1 mapping is used because it produces a magnetization dynamic range twice as large as sequences without an inversion pulse. The fact that the magnetization ranges from $-M_z$ to $+M_z$ (instead of 0 to $+M_z$) provides a greater contrast for T_{1w} images. IR sequences also give the possibility to null signal from specific tissues by carefully selecting the TI. This selective tissue nulling increases image contrast but also allow to do a quick (although approximate) estimation of the T_1 values in the tissues where signal is null. Moreover, IR sequences are simple to use and normally available on most clinical scanners, which is not the case for all T_1 mapping techniques.

On the other hand, IR T_1 mapping suffer from many drawbacks. Since TIs need to be optimized for the T_1 values mapped, long TR values can be required [21]. Moreover, IR T_1 mapping sequences need to be repeated several times to acquire images at different TI values. That limitation makes IR sequences inherently long. In fact, if no fast imaging techniques are applied, IR sequences like IR-SE are normally restricted to single slice acquisition because acquiring

multiple 2D slices can be prohibitively long (i.e., can easily reach several hours of scan time). However, fast or advanced imaging techniques like Fast (or Turbo) Spin Echo (FSE) [22] or Echo Planar Imaging (EPI) [23] can be used to accelerate scan time. In the end, without acceleration techniques, IR-based T_1 mapping techniques like the IR-SE sequence cannot be done in clinically feasible times [20].

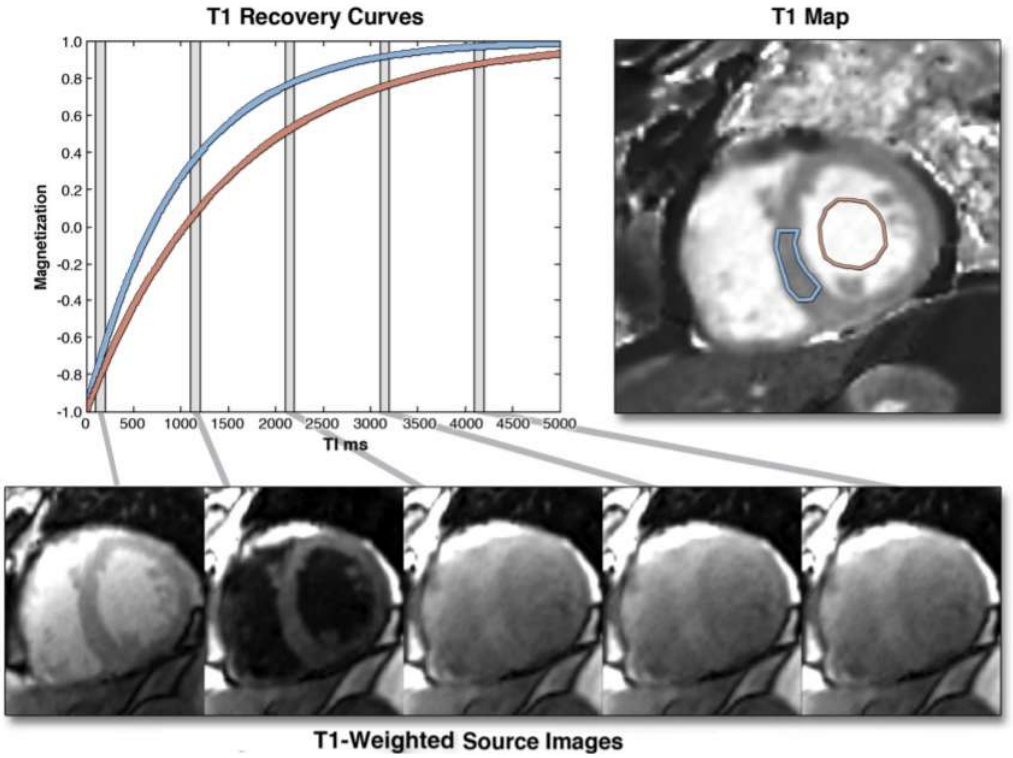

Figure 2.8 *- Example of an IR-based T_1 mapping technique. The images acquired at five different TIs (gray lines) are shown at the bottom. The resulting T_1 map is shown at the top right. Figure reproduced from* [19]*, with permission.*

Variations of IR T_1 mapping like MOLLI (Modified Look-Locker inversion recovery) sequence exist [24]. MOLLI is especially used for myocardial T_1 mapping. MOLLI is an IR-based technique with the difference that multiple signal acquisitions are done every TR in opposition with conventional IR where only one acquisition is done per TR. Ultimately, doing multiple acquisitions per TR reduces the number of inversion pulses required (i.e., fewer repeated acquisitions) and allows faster acquisition times. An important point to mention is that MOLLI does not calculate a "true" T_1 value, but an "apparent" T_1 value instead which is an underestimation of the "true" T_1 values [20]. A correction needs to be applied to obtain the

"true" T_1 values afterwards [24]. Even if faster than IR, MOLLI cannot produce volumetric T_1 maps within clinical feasible times. MOLLI is exclusively used in single-slice cardiac T_1 mapping. Furthermore, MOLLI is not a sequence readily available on most clinical scanners.

2.2.2 Variable Flip Angle (VFA)

In contrast with IR-SE and MOLLI, the Variable Flip Angle (VFA) T_1 mapping technique can produce 3D T_1 maps in clinically acceptable times [25]. VFA is not an IR-based T_1 mapping technique. The principle behind VFA is to acquire two (or more) spoiled GRE acquisitions with constant TR and TE and different flip angles. Subsequently, signal values acquired can be fitted to calculate the resulting T_1 values. VFA suffers from three assumptions that limit its accuracy. First, VFA assumes perfect spoiling of the transverse magnetization and perfect flip angles which is practically never the case [20]. However, flip angles values can be corrected by acquiring a B_1^+ map in addition to the spoiled GRE acquisition to the price of increasing scan time. Spoiling refers to the disruption of the remaining transverse magnetization before each excitation. Adding spoiling at the end of each repetition ensures that no transverse magnetization is transferred from an excitation to the other. Spoiling techniques are varied and can be used with the vast majority of sequences not only VFA [26]. Moreover, nonlinear fitting of the signal values to calculate the T_1 values can be considerably long. On the other hand, by adjusting the VFA signal equations, it is possible to avoid nonlinear fitting and use a simple linear fit of the signal values to the cost of creating a noise bias to low SNR regime in the resulting images [20].

2.2.3 MP2RAGE

The *Magnetization-Prepared 2 Rapid Acquisition Gradient Echo* (MP2RAGE) sequence is an extension of the MPRAGE sequence [27]. MPRAGE is currently the most widely used sequence for T_{1w} imaging of the brain [8]. The MP2RAGE sequence starts with a 180^o inversion pulse of the magnetization (i.e., MP2RAGE is also an IR-based T_1 mapping technique). After a certain delay named TA, a first Rapid Acquisition of Gradient Echoes (RAGE or FLASH [28]) block composed of several low flip angles (α_1) with short TRs (usually < 10 ms) is acquired. The TI of this RAGE block (TI_1) corresponds to the delay between the inversion pulse and the moment

when the center of k-space is crossed. After the first RAGE block, another delay called TB is applied before acquiring a second RAGE block. The same principle applies regarding TI_2 definition. Finally, another delay named TC is introduced after the second RAGE block to enable recovery of the magnetization. This process is repeated several times to sample the third dimension of the k-space. The MP2RAGE pulse sequence is shown on Figure 2.9.

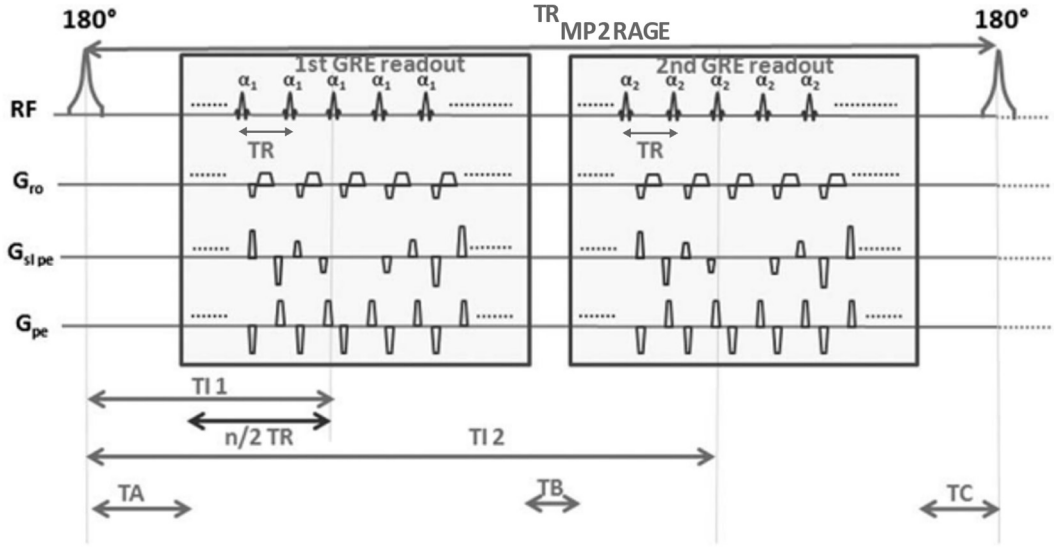

***Figure 2.9** - MP2RAGE pulse sequence. The two light grey rectangles correspond to the two RAGE blocks. The TR corresponds to the repetition time between two fast low flip angles excitations inside RAGE blocks whereas $TR_{MP2RAGE}$ corresponds to the repetition time between two successive inversion pulses. Figure adapted from [8], with permission.*

The particularity of MP2RAGE is that one T_{1w} image is produced per RAGE block, making a total of two images acquired with different T_{1w} contrasts per $TR_{MP2RAGE}$. Since both RAGE images are acquired with a very brief delay between each other, both images are inherently co-registered [8]. These two complex images (or signals) are then recombined to produce the final MP2RAGE image with Eq. 11.

$$\text{MP2RAGE Signal} = Re\left(\frac{\text{RAGE}_1^* \times \text{RAGE}_2}{|\text{RAGE}_1|^2 + |\text{RAGE}_2|^2}\right) \qquad \textit{Eq. 11}$$

Here $RAGE_1^*$ is the complex conjugate of the first RAGE block signal and $RAGE_2$ the complex signal of the second RAGE block. Only the real part of both complex signals is kept to produce MP2RAGE signal. Eq. 11 fundamentally limits MP2RAGE signal values calculated between -0.5 and +0.5. By recombining both complex signals with Eq. 11, two main advantages stand out. First, it is possible to know whether there was a phase change between the first and second RAGE block and, secondly, the SNR of MP2RAGE images calculated is superior to a conventional ratio of both RAGE signals [8].

MP2RAGE images have the property of being highly T_1-weighted. They are also completely independent of T_{2*}, proton density (hidden in M_0) and signal reception (B_1^-) biases because these effects are cancelled out with Eq. 11. Moreover, in the low flip angle regime, MP2RAGE images are partly independent of B_1^+ inhomogeneities. MP2RAGE images are said to be *partly* independent of B_1^+ inhomogeneities because unavoidable B_1^+ dependency remains in the RAGE signal equations [8]. Both RAGE theoretical signal equations are shown with Eq. 12Eq. 13 respectively.

$$RAGE_1 = B_1^- e^{-TE/T_2^*} M_0 \sin(\alpha_1) \times \left\{ \left(\frac{-invEff \times m_{z,SS}}{M_0} EA + (1 - EA) \right) (cos(\alpha_1) E1)^{n_{bef}} + (1 - E1) \frac{1 - (cos(\alpha_1) E1)^{n_{bef}}}{1 - cos(\alpha_1) E1} \right\} \quad \textit{Eq. 12}$$

where $E1 = \exp(-TR/T_1)$, $EA = \exp(-TA/T_1)$, invEff is the inversion efficiency of the inversion pulses, $m_{z,SS}$ the steady-state longitudinal magnetization and n_{bef} the number of excitations before the k-space center. InvEff is a value normally around 1.00 that represents how well the inversion pulse inverts the spins experimentally. Values smaller than 1.00 represents an inversion smaller than 180°.

$$RAGE_2 = B_1^- e^{-TE/T_2^*} M_0 sin(\alpha_2) \times \left\{ \frac{\mathrm{m_{z,SS}}}{\mathrm{M_0}} - (1 - \mathrm{EC}) \over \mathrm{EC}(\cos(\alpha_2)\mathrm{E1})^{\mathrm{n_{aft}}} - (1 - E1) \frac{(cos(\alpha_2)E1)^{-n_{aft}} - 1}{1 - cos(\alpha_2)E1} \right\} \quad \textit{Eq. 13}$$

where EC = exp(-TC/T_1) and n_{aft} is the number of excitations after the k-space center.

By being highly T_{1w}, MP2RAGE images are intrinsically suitable for T_1 mapping [8]. By inserting all acquisitions parameters and time delays necessary in addition to a predefined range of T_1 values to Eq. 12Eq. 13, it is possible to calculate the MP2RAGE signal value associated with every T_1 value given in input. In other words, it is possible to create a lookup table of MP2RAGE signal-T_1 values. This lookup table is then used with linear interpolation to find the T_1 values associated with every MP2RAGE signal values found in the image. This T_1 mapping process is considerably fast in computing time.

The lookup table between T_1 and MP2RAGE signal values is determined by the combination of MP2RAGE acquisition parameters. More precisely, the flip angle values of both RAGE blocks, the TIs, the number of excitations, the TR and $TR_{MP2RAGE}$ influence the resulting T_1-MP2RAGE signal lookup table. Thus, it is possible to create specific lookup tables for every combination of acquisition parameters.

To reduce widening of the T_1 point-spread function (PSF), which results in blurring in the images, the number of excitations inside RAGE blocks is normally the smallest number between the number of phase-encodes and slices [8]. Moreover, inversion pulses are not perfect. Imperfect inversion pulses result in an inversion of the magnetization that can be slightly different than 180º. The value of invEff depends on the type of inversion pulse used and it can be calculated beforehand with numerical simulations.

Other MPRAGE-based T_1 mapping techniques exist. For instance, T_1 maps can be produced from MPRAGE images directly [29]. By keeping MPRAGE acquisition parameters constant and repeating the acquisition at three different TIs, the MPRAGE signal becomes linear to $e^{-TI/T1}$ and

T_1 maps can be produced. The drawbacks of the 3-TI MPRAGE T_1 mapping technique are considerable acquisition time for volumetric datasets, remaining dependencies on proton density (PD) and T_2^*, sensitivity to motion due to acquisitions separated by minutes and the intrinsic widening of the T1 PSF along the phase-encoding direction [29].

Moreover, MP3RAGE acquisitions have been developed [30]. In MP3RAGE acquisitions, a third RAGE block is added after the first two. This additional RAGE block allows the calculation of the inversion efficiency of every voxel in the volume with the goal of providing T_1 values corrected for inversion inhomogeneities. One of the main advantages of MP3RAGE is that the third RAGE block does not increase scan time since it normally fits between the second RAGE block and the next inversion pulse. MP3RAGE requires a non-linear least square fitting process to find the inversion efficiency and T_1 values simultaneously for every voxel.

The first T_1 mapping results from the MP3RAGE sequence reported in the literature [30] showed lower precision levels than MP2RAGE for the T_1 values calculated in addition of showing that invEff is highly uniform and close to 1.00.

Ultimately, all MPRAGE-based T_1 mapping techniques shown in this section can be gathered under the name of "MPnRAGE" T_1 mapping techniques where n stands for the number of RAGE blocks used. The rest of this work will be entirely focused on MP2RAGE T_1 mapping.

2.3 Fat-Water Separation

2.3.1 Chemical Shift (δ)

As stated in section 2.1, MR signal is due to ^{1}H nuclei (or protons) present in remarkably large quantities in the human body (~ 10^{28} hydrogen nuclei). ^{1}H nuclei are found in different molecular environments. More precisely, ^{1}H nuclei are surrounded by electron clouds that modify the local magnetic field felt by hydrogen nuclei [31]. These electron clouds around ^{1}H nuclei induce small magnetic fields that oppose $\mathbf{B_0}$. Thus, the local magnetic field ($\mathbf{B_{loc}}$) felt by the ^{1}H nuclei is slightly inferior to $\mathbf{B_0}$. In other words, the electron clouds are acting as shields against $\mathbf{B_0}$ for

hydrogen nuclei. Molecular environments with different electron clouds will produce different shielding levels to ^{1}H nuclei.

Knowing the Larmor frequency equation (Eq. 2), one can remember that the precession frequency of spins depends on the magnetic field strength. Ultimately, it is the local magnetic field ($\mathbf{B_{loc}}$) felt by the spins that determines the precession frequency of the spins and not $\mathbf{B_0}$ solely. Thus, the precession frequency of the spins will vary slightly based on the value of $\mathbf{B_{loc}}$ produced by the electron shielding of their molecular environment. This difference in precession frequency between hydrogen nuclei from two chemical species is known as the chemical shift (or δ) and is normally expressed in parts per million (ppm) of the Larmor frequency [32].

For instance, water and fat ^{1}H nuclei precess at slightly different frequencies due to the differences in their respective chemical environments. Water ^{1}H nuclei are less protected by their electron cloud resulting in a larger $\mathbf{B_{loc}}$ (and ω *de facto*) than fat ^{1}H nuclei [33]. The chemical shift between water and fat ^{1}H nuclei is on average equal to 3.5 ppm or 420 Hz at 3T [32]. The chemical shift is given on average because fat molecules in the human body are complex molecules known as triglycerides that contain several ^{1}H nuclei with different atomic neighbors. Having different atomic neighbors results in fat ^{1}H nuclei being affected differently by electron cloud shielding inside the fat molecule. Consequently, ^{1}H nuclei inside the fat molecule do not possess the same precession frequency relative to water ^{1}H nuclei. The different precession frequencies of hydrogen nuclei inside the fat molecules are expressed as a spectrum of frequencies. Three examples of spectra measured from MR Spectroscopy (MRS) for subcutaneous fat, dairy cream, and a safflower oil emulsion are shown in Figure 2.10. The remarkably large peak for dairy cream and safflower oil emulsion at ~4.7 ppm represents the water peak since both emulsions contain water, which is technically not part of the fat spectrum. The water peak is not present for subcutaneous fat spectrum since it does not contain water. The second largest peak visible on Figure 2.10 (peak B) is the methylene peak of the fat spectrum and represents most of the fat hydrogen nuclei. The methylene fat peak has a chemical shift of 3.5 ppm with water approximately (at ~4.7 ppm). The rest of the fat protons are scattered in smaller secondary peaks with different chemical shifts. As visible from Figure 2.10, fat spectra vary slightly from different types of fat (e.g., dairy fat vs. vegetable fat vs. human fat). Different types

of fat show similar overall fat spectra but have slight variations in relative amplitudes of secondary fat peaks.

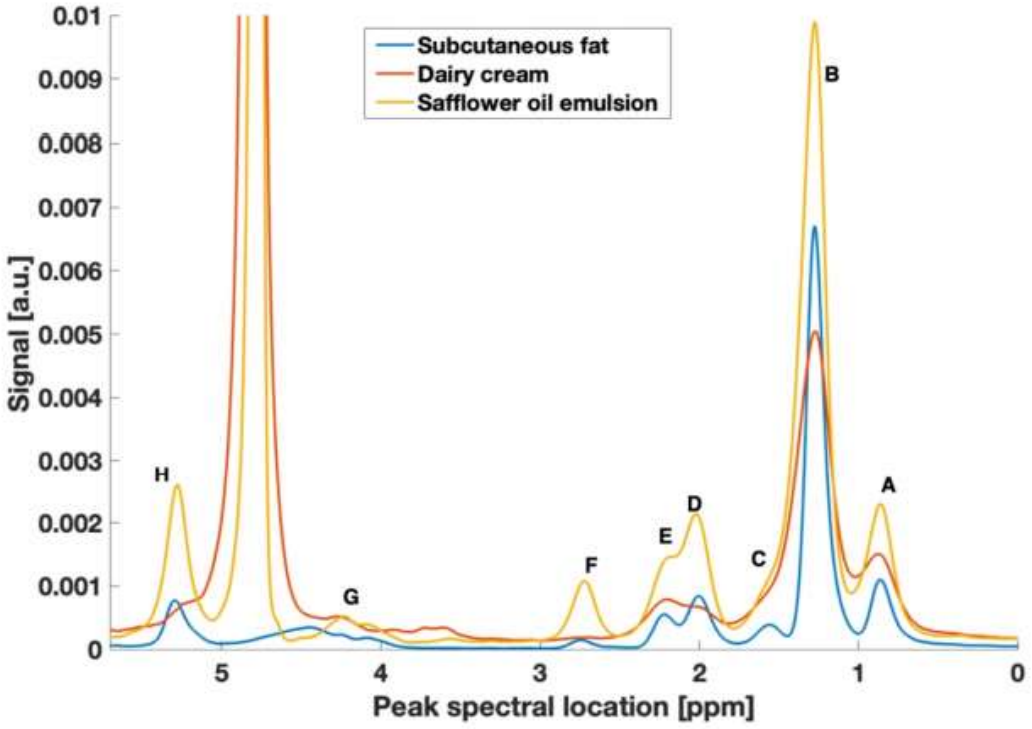

Figure 2.*10 - Fat spectra measured with MRS from three types of fat: subcutaneous fat (blue spectrum), dairy cream (orange spectrum) and safflower oil emulsion (yellow spectrum). The noticeably large peak at ~4.7 ppm for dairy cream and safflower oil emulsion spectra represents the water peak. The cream and safflower emulsion both contain water in opposition with subcutaneous fat. The letters A to H represent the discernable fat peaks in the safflower emulsion. Figure reproduced from* [36]*, with permission.*

Since the chemical shift between fat and water molecules is known, it is possible to use that information to separate MR signal coming from fat and water ^{1}H nuclei. Several techniques exist to separate fat and water signals and they are known as fat-water separation techniques. The technique used in this work to separate fat and water signals is named 3-point Dixon and is presented section 2.3.2.

2.3.2 Dixon techniques

Since fat and water ^{1}H nuclei possess slightly different precession frequencies, the spins go in-phase (IP) and out-of-phase (OP) through time. The duration of the phase-cycling is determined by the value of the chemical shift. For instance, at 1.5 T, it takes 1/(3.5 ppm x 63.87 MHz) or ~4.4 ms for water and fat ^{1}H nuclei to complete one cycle (i.e., IP, OP, and IP again) [32]. This process is shown with Figure 2.11. The phase-cycling of fat and water spins is two times faster at 3 T (since 63.87 MHz becomes 127.74 MHz) and even faster for larger $\mathbf{B_0}$.

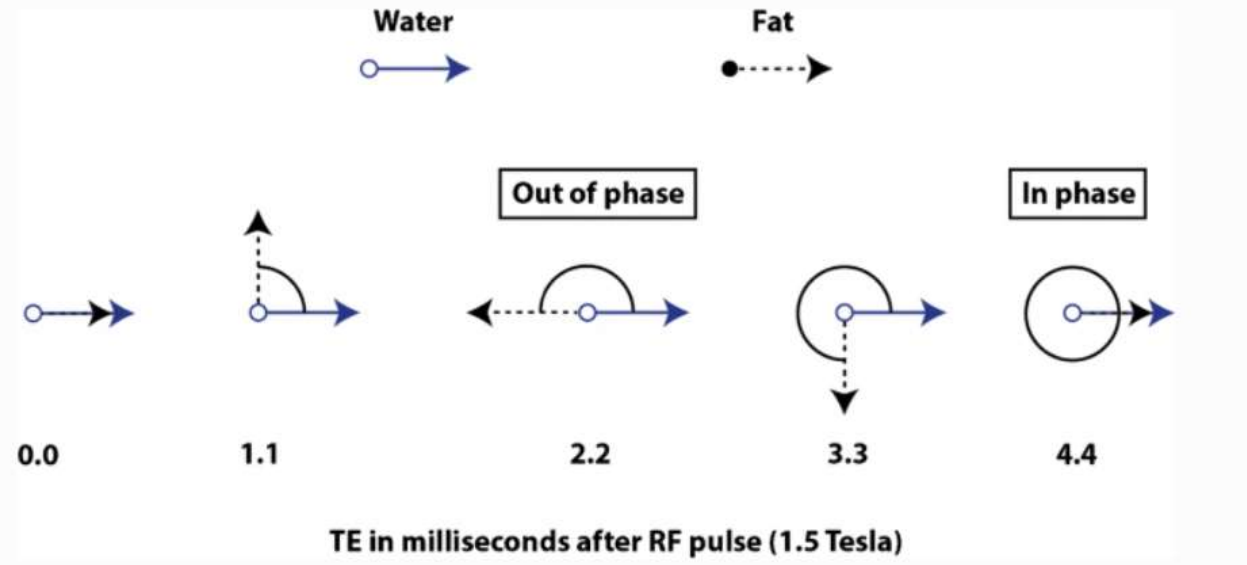

Figure 2.*11 - Phase-cycling between fat and water ^{1}H nuclei at 1.5T. After being excited, fat and water hydrogen nuclei are in phase (IP) in the transverse plane. However, both chemical species rapidly lose their phase coherence to become out of phase (OP) after 2.2 ms. Figure reproduced from* [32]*, with permission.*

Thus, by acquiring MR images at two echoes with different TEs, it is possible to produce IP and OP images of fat and water protons. For IP images, the signal measured comes from fat and water ^{1}H nuclei added together (Water [W] + Fat [F] signals) whereas for OP images, signal comes from fat and water ^{1}H in complete opposition (Water – Fat signal). Consequently, IP images have more signal than OP images. By doing the average of the sum and difference of the

IP and OP images, it is possible to create "water-only" and "fat-only" images as shown with Eq. 14Eq. 15.

$$0.5 \times [\mathrm{IP} + \mathrm{OP}] = 0.5 \times [(\mathrm{W} + \mathrm{F}) + (\mathrm{W} - \mathrm{F})] = 0.5 \times [2\mathrm{W}] = \mathbf{W\ only\ image} \quad \textit{Eq. 14}$$

$$0.5 \times [\mathrm{IP} - \mathrm{OP}] = 0.5 \times [(\mathrm{W} + \mathrm{F}) - (\mathrm{W} - \mathrm{F})] = 0.5 \times [2\mathrm{F}] = \mathbf{F\ only\ image} \quad \textit{Eq. 15}$$

This technique to produce water- and fat-only images is known as 2-point Dixon [33]. Nowadays, several variations of the original 2-point Dixon technique exist and they are regrouped in a category of fat-water separation techniques named Dixon techniques.

Originally developed in the mid-1980s, the original 2-point Dixon technique (2-point because two echoes are acquired) suffered from many technical challenges that made its clinical implementation difficult [34]. Nevertheless, substantial technical advancements made in the early 2000s in MRI helped implementations of Dixon techniques experience a "renaissance". Nowadays, Dixon techniques are considered as the standard in fat suppression for abdominal imaging at 3 T and are available with every manufacturer [32]. Dixon techniques can be used for other anatomy regions as presented with Figure 2.12 showing images produced from 2-point Dixon in the upper leg [32].

The most commonly used Dixon technique nowadays, due to its robustness to $\mathbf{B_0}$ inhomogeneities, is the 3-point Dixon [10]. Instead of two echoes like 2-point Dixon, three echoes are acquired. The third echo is acquired with a phase shift of -180° (OP) or 360° (IP) and is used to correct for $\mathbf{B_0}$ inhomogeneities before recombing IP and OP images [34]. $\mathbf{B_0}$ inhomogeneities introduce errors in the phase between fat and water ^{1}H nuclei. This phase error modifies the exact timing when fat and water hydrogen nuclei are IP and OP. If this phase error is not taken in account (as in 2-point Dixon), water and fat protons will have a phase shift slightly different from the predicted 0° and 180° shifts at the selected TEs. Ultimately, the quality of the resulting fat-water separation will be affected.

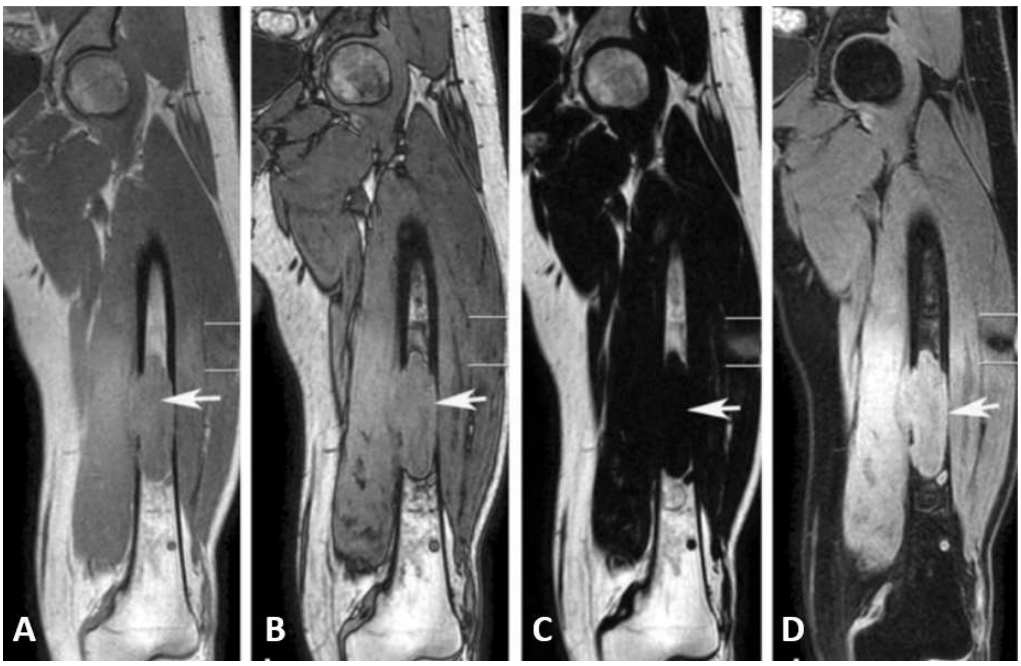

Figure 2.*12 - 2-point Dixon results from GRE T_{1w} coronal images of a femur. A: IP image. B: OP image. C: Fat-only image. D: Water-only image. A femoral lesion is shown with the white arrow and a small tumor nodule is shown between the two horizontal lines on the right. Figure reproduced from* [32]*, with permission.*

In general, the success of Dixon techniques will depend on the quality of phase unwrapping [34]. Phase values are inherently limited between 0 and 2π (or – π to π) radians. Thus, if a phase larger than 2π is measured, the value will be "wrapped" between 0 and 2π and vice-and-versa for values smaller than 0. Phase wrapping in the phase images used for fat-water separation with Dixon techniques can introduce swaps between fat and water signals in the final separated images. If no phase wrapping is present, fat-water swaps are not a problem. However, MR images without phase wrapping requires a level of $\mathbf{B_0}$ homogeneity that is considerably difficult to achieve in most clinical situations [34]. Thus, the use of a phase unwrapping algorithm is required for most of the cases. A solid approach to phase unwrapping is known as quality-guided unwrapping [35]. Phase unwrapping is a complete research field in itself and will not be covered in this work. More details are available in [34]. Even if a solid phase unwrapping algorithm is used, phase wrapping can still remain and produce fat-water swaps between the resulting water and fat images. In general, 3-point Dixon technique is known to be less affected by phase unwrapping errors than 2-point Dixon [34].

Chapter 3

Materials and Methods

This chapter presents the methodology and material used for the completion of this project. This chapter is divided in sections presenting different portions of the project accomplished to produce the main conclusions drawn later in Chapter 5. The chapter starts with the methods used to develop the short T_1 MP2RAGE protocol with qualitative and quantitative assessments followed by its validation with experimental acquisitions. After that, the methodology used to assess the ME-MP2RAGE protocol experimentally and quantitatively for fat-water separated T_1 mapping is presented.

3.1 Optimization of MP2RAGE acquisition for short T_1

The first stage of the project was to design, by trial and error, a new version of the MP2RAGE protocol, initially optimized for brain T_1 values between 1000 ms and 2000 ms approximately [8]. The T_1 range of interest for the new MP2RAGE protocol was defined between 200 ms and 800 ms based on fat T_1 values measured from individual fat peaks in [36]. As explained in section 2.2.3, several different MP2RAGE-T_1 lookup tables can be produced by modifying acquisition parameters of the MP2RAGE sequence. The design process had to respect two main conditions for the general shape of the new MP2RAGE lookup table: the MP2RAGE lookup table had to be as (1) monotonic and (2) linear as possible in the predefined T_1 range of interest. The rationale behind condition (1) is that a non-monotonic curve creates ambiguities between two different T_1 values associated to one single MP2RAGE signal value without the possibility to know which T_1 value is appropriate. A linear behavior inside the T_1 range of interest was desired because errors in MP2RAGE signal values are linearly translated to errors in T_1 estimates and because linear interpolation was used to calculate T_1 values [8].

After finding a new MP2RAGE lookup table optimized for short T_1 mapping with trial-and-error, a qualitative analysis of the impact of individual acquisition parameters on the MP2RAGE lookup table was performed. The newly designed MP2RAGE-T_1 lookup table for short T_1 mapping was used as a starting point to assess how individual acquisition parameters modified the calculated lookup table. By keeping all acquisition parameters constant except one, it was possible to assess the impact of that parameter by selecting different values and calculating the MP2RAGE-T_1 lookup table for the variations selected. The qualitative assessment gave the possibility to examine which parameters were the main ones impacting the lookup table.

Before calculating the MP2RAGE lookup table, the user could decide to keep only the monotonic part of the resulting MP2RAGE lookup table before calculating the T_1 values or keep the complete MP2RAGE lookup table calculated from the minimum to the maximum T_1 value given in input to the algorithm. The process of keeping only the monotonic part of the lookup table was done by "clipping" the calculated lookup table when the minimum and maximum MP2RAGE signal values (i.e., -0.5 and +0.5 respectively) were reached. Thus, the resulting range of T_1 values available was different for every combination of acquisition parameters. Moreover, the resulting T_1 range available could only be shorter or equal to the original T_1 range given in input to the lookup table. Enabling the clipping option removed ambiguities due to overlapping of T_1 values. For the qualitative assessment and design of the short T_1 MP2RAGE protocol (i.e., this section), the "clipping" option of the MP2RAGE lookup table was disabled to visualize the overlapping. However, for the rest of the project (i.e., numerical simulations and experimental acquisitions), clipping of the MP2RAGE lookup tables was enabled to be consistent with the original MP2RAGE technique [8]

3.2 Quantitative assessment of MP2RAGE for short T_1 mapping with numerical simulations

After the qualitative design and assessment of the newly optimized MP2RAGE protocol for short T_1 values, a quantitative assessment with numerical simulations was done for two purposes. First, numerical simulations were done to assess the theoretical accuracy and precision of the new MP2RAGE protocol when noise was added to MP2RAGE signal values. Second,

simulations were used to tweak the acquisition parameters to find the most optimal protocol for the predefined T_1 range of interest. Numerical simulations were done on two different MP2RAGE protocols simultaneously: one for short T_1 mapping (the newly designed MP2RAGE protocol) and the other for brain T_1 mapping (the original MP2RAGE protocol). In addition to assessing the theoretical accuracy and precision of the newly designed MP2RAGE protocol, numerical simulations gave the possibility to compare its accuracy and precision against the original MP2RAGE protocol for brain T_1 mapping. Ultimately, the goal was to design a new MP2RAGE protocol that is more accurate and precise than the original brain T_1 MP2RAGE protocol over the T_1 range of interest. All numerical simulations were performed with scripts written in-house in MATLAB version R2020b (The MathWorks, Natick, Massachusetts, USA). The acquisition parameters found from the qualitative assessment and used for the numerical simulations are shown in Table 3.1.

Table 3.1 *- Acquisition parameters of MP2RAGE protocols used in numerical simulations.*

MP2RAGE protocol	TIs [s]	TR [ms]	$TR_{MP2RAGE}$ [ms]	FAs [°]	Nb. Of Excitations
Short T_1: Protocol A	[0.5 , 1.5]	6	2500	[5, 5]	150
Short T_1: Protocol B	[0.45 , 1.5]	4.5	2700	[5, 5]	150
Brain T_1	[0.8 , 2.2]	5.5	6250	[4, 5]	150

Two variations of short T_1 MP2RAGE protocols were used for numerical simulations. Versions A and B of the short T_1 MP2RAGE were two combination of parameters found from the qualitative assessment of the MP2RAGE protocol for optimization of short T_1 values.

Simulations were conducted only with linear k-space encoding. Linear encoding corresponds to an encoding scheme where one of the extremities of k-space is acquired with the first readout. When the center of k-space is acquired at the first excitation, this is known as centric encoding.

Centric encoding was not implemented in the custom MP2RAGE pulse sequence and therefore not available for the acquisitions of this project.

Numerical simulations used a range of T_1 values from 50 to 5000 ms with 5 ms steps. Independent Gaussian (or normal) noise was added in quadrature (i.e., added to the real and imaginary channels) to both RAGE real-only signal equations (Eq. 12Eq. 13) before inserting them into the MP2RAGE signal equation. By selecting a value for the SNR, it was possible to scale the noise level added to RAGE signals. By dividing the average signal of RAGE block #2 by the selected SNR value, the level of Gaussian noise to be added was calculated. RAGE block #2 was used for noise scaling since it corresponded to the RAGE block with the highest average signal. Several SNR values were chosen to performed noise simulations (10, 15, 20 and 25). A total of 10 000 simulated noisy versions of the noiseless MP2RAGE lookup table were calculated for each SNR value. In other words, the simulations generated 10 000 noisy MP2RAGE signals (for every noiseless MP2RAGE signal value), that ultimately correspond to 10 000 noisy output T_1 values. 10 000 was chosen to ensure a normal distribution of the simulated signal values. Moreover, an inversion efficiency of 0.96 was assumed for numerical simulations.

As mentioned in the first paragraph of this section, the accuracy and precision of the output T_1 were calculated for every T_1 value inputted to the simulation. Accuracy was defined as the difference between the mean of the 10 000 T_1 values estimated from noisy simulated signal values and the corresponding theoretical noiseless T_1 value. Precision corresponded to the standard deviation of the 10 000 T_1 values estimated from simulated signal values spread out around the corresponding T_1 value. The quality of MP2RAGE protocols designed for short T_1 values was defined by the accuracy and precision measured inside the short T_1 range of interest in comparison with the original MP2RAGE brain protocol. The numerical simulations were used to verify if the observations of the qualitative assessment explained in section 3.1 were translated quantitatively.

The numerical simulations also helped in the final tweaking of acquisition parameters of the newly design MP2RAGE protocols for short T_1 values. For instance, numerical simulations were

run a second time exclusively between version A and B of the short T_1 MP2RAGE protocol to see if the slight variations in TIs or $TR_{MP2RAGE}$ were producing detectable differences in accuracy and precision. Then, the version with the highest accuracy and precision between the two was kept for the next experimental acquisition of the project.

An examination of the theoretical B_1^+ sensitivity was performed for the three MP2RAGE protocols used in numerical simulations. Variations up to ± 40% of the expected excitation flip angle values were used to see the effects on MP2RAGE lookup tables, in line with previous observations with [8]. MP2RAGE lookup tables were calculated for ± 20% and 40% variation of the flip angles and plotted on the same figure to assess the impact of B_1^+ inhomogeneities for every MP2RAGE protocol.

3.3 Experimental validation of the short T_1 MP2RAGE protocol

Once an optimized MP2RAGE protocol for short T_1 mapping was developed from in depth qualitative and quantitative evaluations, the MP2RAGE protocol was evaluated experimentally and validated with a homemade phantom. The phantom was composed of seven 50 ml vials positioned circularly inside a large compartment containing a NaCl solution with GBCA (gadobutrol, Gadovist®, Bayer Inc.). The NaCl solution brought the electric conductivity of the compartment to similar levels as seen in human tissues to increase B_1^+ uniformity [37]. A concentration of NaCl of 85 mM was used in approximately 1.5 L of deionized distilled water. A volume of 2.4 mL of a GBCA solution at 62.5 mM was added to decrease the T_1 value of the large compartment. The seven vials contained different volumes of deionized distilled water with GBCA solution. The volume of GBCA solution was measured with a micropipette accurate down to 100 µL. The volume of water was then added to reach the 50 mL line shown on the vial. The phantom used with the estimated concentrations of GBCA inside vials is shown in Figure 3.1.

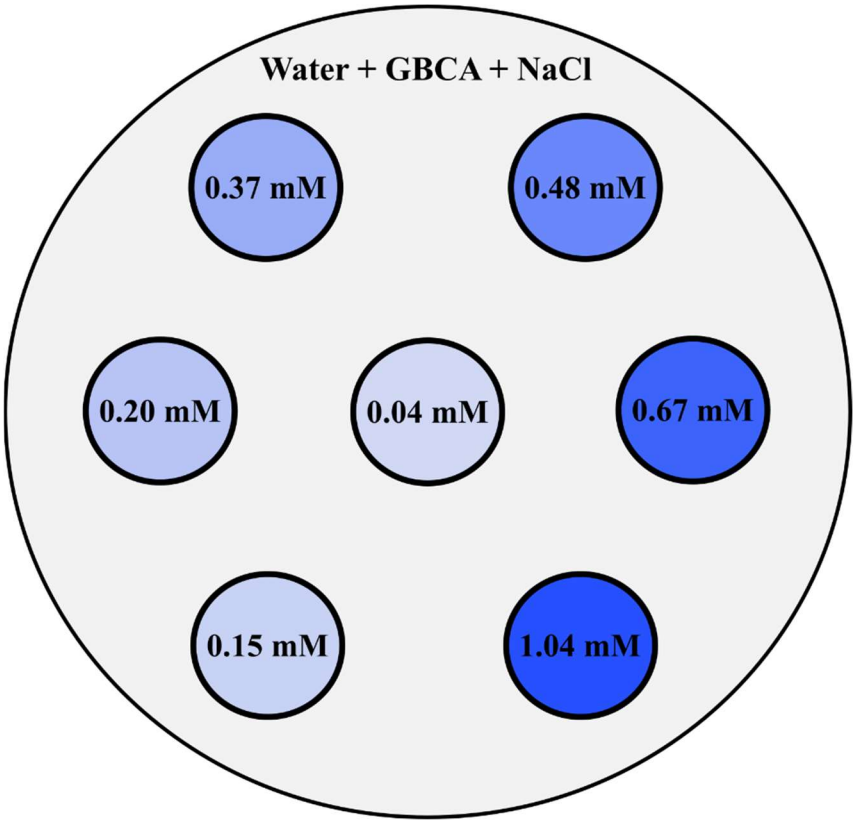

Figure 3.1 *- Schematic of phantom #1 used for experiment #1. Concentrations of GBCA are written inside each vial.*

From basic calculations with the theoretical relaxivity value of the gadolinium-based contrast agent used for dilutions (i.e., 4.5 $s^{-1}mM^{-1}$ [38]) and the different concentrations, it was possible to obtain different approximate T_1 values expected for each vial with a short script written in-house (Anaconda 3/Python 3.7) written by a former colleague of the research group. The estimations of the T_1 values from the theoretical concentration of the GBCA solution inside each vial and the corresponding volumes are shown in Table 3.2.

Table 3.2 *- Expected T_1 values, [GBCA], volume of GBCA solution at 6 mM and water inside the seven 50 mL vials with the large compartment (identified with a star) for phantom #1.*

Vial	Expected T_1 value [ms]	Target [Gd^{3+}] in the vial [mM]	Volume GBCA solution [mL] at starting concentration of 6 mM	Volume Water [mL]
1	~200	1.04	8.7	41.3
2	~300	0.67	5.6	44.4
3	~400	0.48	4.0	46.0
4	~500	0.37	3.1	46.9
5	~800	0.20	1.7	48.3
6	~1000	0.15	1.3	48.8
7*	~1277*	~0.10*	-	-
8	~2000	0.04	0.3	49.7

A convention was established to identify the different MP2RAGE protocols acquired experimentally. Each protocol was identified by two successive letters followed by a number and another letter if required. The first letter identifies which T_1 range the MP2RAGE protocol is optimized for: either short (S) (i.e., between 200 ms and 800 ms) or long (L) (i.e., between 1000 ms and 2000 ms) T_1 range. The second identifies either it was a single echo (S) sequence or a multi-echo (M) sequence. The number refers to the experiment number (e.g., 1, 2, or 3). If variations of a given protocol were acquired during an experiment, they were individually identified by an additional letter after the number (e.g., A, B, C, etc.). This convention was used for all acquisitions during the project.

For the first experiment, four single echo MP2RAGE protocols, one multi-echo MP2RAGE (ME-MP2RAGE) protocol and one IR-SE protocol were acquired. The ME-MP2RAGE protocol was a custom sequence provided as part of a research agreement with the Athinoula A. Martinos Center for Biomedical Imaging at the Massachusetts General Hospital. All acquisitions were done on a 3 T Siemens MAGNETOM Prisma system (Siemens Medical Solutions, Erlangen, Germany) with software version VE11C, a 20-channel receiver-only head-and-neck coil,

TrueForm B_1 shimming and standard Siemens B_0 shim mode. The IR-SE was the standard single-slice acquisition available on the Siemens MRI platform and was considered as the reference T_1 mapping technique. The inversion pulse used was an adiabatic hyperbolic secant pulse. Acquisition parameters for MP2RAGE and IR-SE protocols acquired during experiment #1 are shown in Table 3.3 and Table 3.4 respectively.

All protocols had the same following characteristics: (1) PF was not applied, (2) parallel imaging (GRAPPA) was used with an acceleration factor of 2 and 32 reference lines, (3) non-selective excitation, and (4) a linear encoding scheme.

Table 3.3 *- Acquisition parameters of MP2RAGE protocols used during experiment #1.*

Protocol	SS1A	SS1B	SS1C	LS1	SM1
Voxel size [mm^3]	1.13×1.13×1.10	$(1.33)^3$	1.33×1.33×3.47	$(1.33)^3$	$(2)^3$
$TR_{MP2RAGE}$ [s]	2.7	2.7	2.7	4	2.7
TIs [s]	(0.45, 1.5)	(0.45, 1.5)	(0.45, 1.5)	(0.6, 1.8)	(0.45, 1.5)
α [^{O}]	(5, 5)	(5, 5)	(5, 5)	(4, 5)	(5, 5)
TR [ms]	4.5	4.2	4.2	5.5	6
TE [ms]	1.79	1.71	1.71	2.32	(1.04, 2.81 & 4.58)
Band-width [Hz/px]	500	500	500	300	1515
Nb. of Slices	144	144	48	144	88
FOV [mm^2]	170×175	200×204	200×204	200×204	200×204
Scan time [min]	4:11	4:11	4:11	6:12	3:01

Table 3.4 *- Acquisition parameters for reference T_1 mapping technique for all experiments.*

Reference	Voxel size [mm^3]	TR [ms]	TIs [ms]	TE [ms]	Bandwidth [Hz/px]	FOV [mm^2]	Scan Time [min/TI]
IR-SE	0.9×0.9×5	5000	50, 100, 200, 500, 1000 and 3000	13	501	170×170	16:05

SS1 protocols (i.e., SS1A, SS1B, and SS1C) represented the same protocols for the MP2RAGE lookup table for T_1 mapping (i.e., same acquisition parameters relevant for the calculation of the lookup table). However, the three variations had different voxel sizes. These variations were acquired to see how voxel size influenced the resulting SNR and T_1 mapping result. Based on the results of the qualitative and quantitative analyses explained in subsections 3.1 and 3.2, the values of TIs and $TR_{MP2RAGE}$ for SS1 and SM1 protocols were directly taken from version B of the short T_1 MP2RAGE protocol. Version B showed slightly higher theoretical precision and lower B_1^+ sensitivity than version A. The TR was automatically minimized by the MR system at the console based on the selected TE . The MRI system software also fixed the number of phase-encoding steps to a value representing 102% of the number of frequency-encoding steps, explaining the unequal FOV dimensions. For the current implementation of the MP2RAGE (and ME-MP2RAGE) sequence used in this project, the number of excitations corresponded to the number of slices.

The SM1 protocol was acquired to demonstrate its experimental feasibility. Three monopolar readouts were used with high bandwidth to produce TEs suitable for fat-water separation with 3-point Dixon.

LS1 was an MP2RAGE protocol developed for fast brain T_1 mapping reproduced from [8]. LS1 was acquired to compare the T_1 map produced against SS1 and SM1. In addition, LS1 was used to compare the experimental accuracy and precision results with the theoretical predictions from numerical simulations.

The reference T_1 mapping technique used was an IR-SE sequence. IR-SE is considered the gold standard for T_1 mapping [20]. The TI and TR values were selected to optimize the T_1 accuracy and minimize the total acquisition time [21]. A large slice thickness was used to increase the SNR of IR-SE images. The in-plane voxel size was minimized to reduce Gibbs ringing artifacts.

T_1 maps of all protocols acquired were produced and analyzed with in-house MATLAB scripts written for T_1 mapping. The location of the IR-SE single slice protocol was noted from the DICOM header, and the same slice location was used for the quantitative comparison with MP2RAGE protocols. Circular regions of interests (ROIs) were created by manually selecting the center of each vial and fixing a radius value of ~8 mm. Due to variations in voxel size across protocols, it was not possible to have ROIs with the same radius value for all protocols. Thus, the closest radius value to 8 mm was chosen when it was not possible to have exactly 8 mm. The ROI for the large compartment was positioned away from the edges of the vials to avoid undesirable effects like ringing artifacts or partial volume. For all T_1 maps, the mean, standard deviation, and 95% confidence interval (CI) were calculated inside the ROIs of every vial (including the large compartment) and protocols. The three quantitative metrics were then compared between MP2RAGE protocols and with the reference.

The accuracy and precision levels calculated experimentally were compared to the predicted values from the numerical simulations for every MP2RAGE protocol. The theoretical predictions of accuracy and precision from numerical simulations were recalculated with the same SNR value as measured experimentally. The comparison between experimental and theoretical results allowed to evaluate the agreement between the theoretical model and experimental acquisitions.

With protocol SM1, fat-water separation was performed with a 3-point Dixon implementation in MATLAB obtained elsewhere [39]. For both RAGE blocks, the 3-point Dixon algorithm required to give in input two parameters named c_1 and c_2 in addition to water and fat spectra. c_1 and c_2 determined the number of seed points used for the fat-water separation algorithm [39] and had to be determined for every RAGE block and ME-MP2RAGE protocol. Values of 0.1 and 2.75 were selected for c_1 and c_2 for RAGE block #1 whereas 0.1 and 2.0 were used for RAGE block #2. These c_1 and c_2 values were chosen with the sole goal of removing all visible fat-water

swaps. c_1 and c_2 values could vary and more than one combination could produce fat-water separated images without swaps [39]. The values used for SM1 were determined from an ad hoc qualitative assessment of the resulting separated MP2RAGE images. The same ad hoc qualitative assessment to determine c_1 and c_2 was used for every fat-water separation process performed during this project. The relative amplitudes and spectral locations of the peaks inside water and fat spectra used were taken from [36]. More precisely, the fat spectrum used corresponded to the fat spectrum of a safflower oil emulsion measured from a STimulated Echo Acquisition Mode (STEAM) MRS sequence [36]. The same fat spectrum was used for all experiments.

The experimental feasibility of the fat-water separation was investigated from SM1. In addition, the noise level inside the fat-only MP2RAGE images calculated from SM1 was calculated for every vial with the ROIs. As shown with Figure 3.1, phantom #1 did not contain any fat. Thus, any signal classified as fat by the 3-point Dixon algorithm was associated with noise.

Furthermore, from fat-water separated MP2RAGE images produced with 3-point Dixon, it was possible to produce fat- and water-specific T_1 maps for SM1. The water-specific T_1 maps correspond to T_1 maps produced from MP2RAGE images containing signal exclusively from water protons (water-only MP2RAGE images). The same principle was applied for fat T_1 maps and the images were called fat-specific MP2RAGE images. The T_1 mapping process for global and fat-water separated T_1 values was the same (i.e., a lookup table was created from MP2RAGE signal values and acquisition parameters). For experiment #1, the fat-specific T_1 map produced was meaningless except for noise level measurement since there was no fat inside phantom #1.

The distinction between global, fat, and water T_1 maps has not yet been specified but is now relevant. Global T_1 maps are T_1 maps produced from images where water and fat protons have not been separated. For instance, IR-SE produces global T_1 maps only because the sequence cannot differentiate between fat and water signals. Conversely, when fat and water signals are separated with a fat-water separation technique like 3-point Dixon, specific T_1 maps can be created. Thus, for the rest of this thesis, T_1 maps are clearly identified as global, water, or fat T_1 maps.

For all protocols acquired in experiment #1, the relaxivity of the GBCA used in phantom #1 was calculated and compared between all protocols. The relaxivity corresponds to the slope of the linear fit of the mean global R_1 values against the corresponding concentrations of GBCA used in vials. The standard deviations reported correspond to the standard errors (SE) of the slopes calculated from the linear fits multiplied by the root square of the number of datapoints used for the fit. The mean global R_1 values measured in the large compartment were not used for relaxivity measurements since uncertainties related to the exact concentration of GBCA were realized after the experiment. Relaxivity values were used as a sanity check for the T_1 maps calculated from MP2RAGE (and ME-MP2RAGE) protocols in this project in comparison with standard values reported in the literature.

3.4 Experimental assessment of the fat-water separated ME-MP2RAGE protocols

Following experiment #1, a second acquisition was done to experimentally assess the fat-water separated T_1 mapping process from ME-MP2RAGE protocols. Two variations of the ME-MP2RAGE protocol were acquired to assess the impact of B_1^+ inhomogeneities on T_1 maps. One protocol was optimized for fast scan time (SM2A) and the other for lower B_1^+ sensitivity (SM2B). The acquisition parameters affecting B_1^+ sensitivity were the $TR_{MP2RAGE}$, TIs, and flip angles [40]. In addition, the impact on accuracy and precision of making minor changes of TIs and TR values for the single echo short T_1 MP2RAGE protocol was measured. Moreover, the slightly modified version of the short T_1 MP2RAGE protocol (SS2) was compared to a new version of the brain T_1 MP2RAGE protocol (LS2).

As mentioned in the paragraph above, SS2 had slightly different TIs and $TR_{MP2RAGE}$ values than SS1. The new TIs and $TR_{MP2RAGE}$ corresponded to the values used for version A of the short T_1 MP2RAGE for numerical simulations. This modification of the TIs and $TR_{MP2RAGE}$ was done to assess if the minor differences in theoretical accuracy and precision observed in numerical simulations between version A and B were measurable experimentally.

For experiment #2, LS2 was substantially different from LS1. After investigations, protocol LS1 used in experiment #1 ended up not being the most representative version of a MP2RAGE protocol for brain T_1 mapping. Indeed, the LS1 protocol had been optimized for fast scan time and not for accurate brain T_1 mapping [8]. The acquisition parameters for all protocols acquired during acquisition #2 are shown in Table 3.5. A reference global T_1 mapping technique was again acquired for experiment #2. The reference T_1 mapping technique used was the same IR-SE sequence as in experiment #1. Acquisition parameters of the IR-SE reference protocol are shown in Table 3.4.

Table 3.5 *- Acquisition parameters of MP2RAGE protocols used for experiment #2.*

Protocol	SM2A	SM2B	LS2	SS2
Voxel size [mm^3]	$(2)^3$	$(2)^3$	$(1.33)^3$	$(1.33)^3$
$TR_{MP2RAGE}$ [s]	2.5	4	6.25	2.5
TIs [s]	(0.5, 1.5)	(0.5, 2.2)	(0.8, 2.2)	(0.5, 1.5)
α [°]	(5, 5)	(4, 4)	(4, 5)	(5, 5)
TR [ms]	5.9	5.9	5.5	4.5
TE [ms]	(1.03, 2.79, 4.55)	(1.03, 2.79, 4.55)	2.32	1.86
Bandwidth [Hz/px]	1720	1720	300	420
Nb. of Excitations	88	88	144	144
FOV [mm^2]	200×204	200×204	200×203	200×205
Scan time [min]	2:48	4:28	9:04	3:53

For acquisition #2, the same phantom as in experiment #1 was used apart from three 50 mL vials that were replaced with vials containing different quantities of fat. A safflower oil emulsion

(Microlipid®, Nestle Health Science) with an initial fat fraction of 50% (weight per volume) was used to produce different fractions of fat inside vials. All fat fractions mentioned in this work are expressed in percentage of weight per volume. Vials #4, 6, and 8 used in experiment #1 were replaced by vials containing 50% fat , 50% fat and 100µL of GBCA solution at 62.5 mM, and 25% fat, respectively. To produce a vial with a fat fraction of 50%, only safflower oil emulsion was added in the vial. To obtain a fat fraction of 25%, 25 mL of safflower oil emulsion and 25 mL of deionized distilled water were mixed. Due to the presence of dust inside the large compartment solution, the solution was replaced between experiments #1 and #2. The same concentrations of NaCl and GBCA solution as stated in subsection 3.3 were used in the large compartment. The four remaining 50 mL vials were untouched and reused from experiment #1. The phantom used for experiment #2 is shown on Figure 3.2. As for experiment #1, global T_1

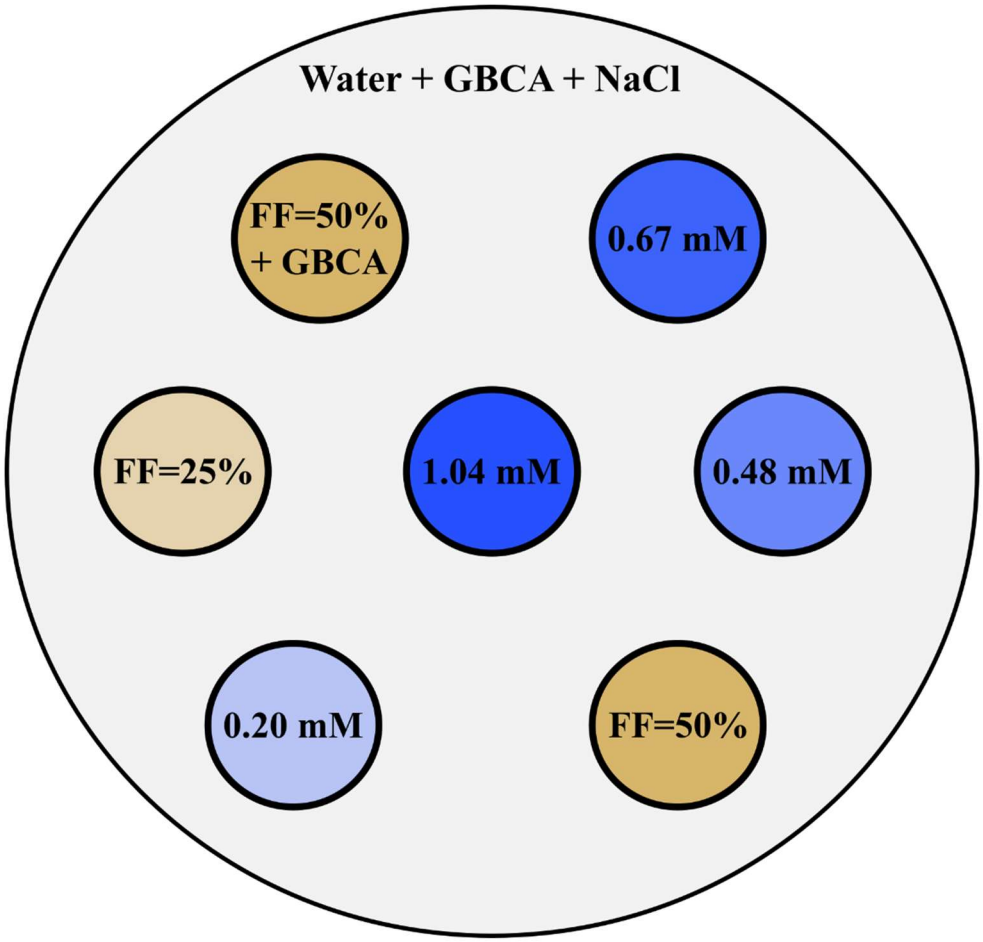

Figure 3.2 *- Schematic of phantom #2 used for experiment #2. The [GBCA] and FFs inside each vial are shown.*

maps were produced and compared between MP2RAGE protocols and the reference technique. The same slice location as the single-slice IR-SE sequence was used for quantitative comparison with MP2RAGE protocols. The same quantitative analyses (i.e., ROI-based calculation of mean, standard deviations and 95% CI inside vials) as for experiment #1 were performed on the global T_1 maps.

The 3-point Dixon implementation from [39] was used to create fat-water separated MP2RAGE images from SM2A and SM2B. Values of 0.5 and 2.0 were selected for c_1 and c_2 for both RAGE blocks for SM2A. For SM2B, 0.5 and 2.5 were chosen for c_1 and c_2 respectively for both RAGE blocks. From the fat-water separated MP2RAGE images, fat and water separated T_1 maps were calculated. The mean T_1 and standard deviations were calculated inside all vials. Fat and water specific T_1 maps produced from SM2A and SM2B were compared between each other. For vials with water only in phantom #2, the water-specific T_1 maps were compared to the reference global T_1 mapping technique.

For all protocols acquired in experiment #2, the relaxivity of the GBCA used for phantom #2 was calculated and compared between all protocols acquired of experiments #1 and #2. The mean global R_1 values from the five water-only vials were used for calculation of relaxivity values. Again, relaxivity measurements were used as a sanity check for the global T_1 maps calculated in experiment #2.

3.5 Quantitative assessment of fat-water separated T_1 mapping from ME-MP2RAGE protocols across a wide range of T_1 values.

A third experiment was acquired with a new phantom to quantitatively assess how water and fat specific T_1 values calculated from ME-MP2RAGE protocols varied across a range of fat fractions and concentrations of GBCA. A phantom containing 20 vials of 15 mL was used. The phantom used for experiment #3 is shown in Figure 3.3. The same concentrations of NaCl and GBCA as stated in section 3.3 were used to produce the large compartment solution surrounding the vials.

The 20 vials inside phantom #3 were arranged in a rectangular fashion of four different concentrations of GBCA by five fat fractions. To produce different fat fractions, safflower oil emulsion (with original 50% fat fraction [weight per volume]) was mixed with deionized distilled water. The five fat fractions used were: 0%, 12.5%, 25%, 37.5% and 50%. To obtain a fat fraction, the volume of safflower oil emulsion required in a vial was calculated with basic dilution calculations and the rest of the vial was filled with water up to the 15 mL line indicated on the vial. For instance, for a fat fraction of 25%, 7.5 mL of safflower oil emulsion was added inside the vial and the rest of the volume was filled with water. The same principle was followed for all fat fractions. For the addition of GBCA, volumes added were small and required a micropipette. The four concentrations of GBCA calculated for the total solution volume (i.e., 15 mL) were: 0 mM, 0.05 mM, 0.104 mM, and 0.156 mM. The goal was to have different concentrations of GBCA able to modulate water T_1 values to reproduce the T_1 values seen *in vivo* measurements. Thus, from a mother solution of GBCA at 7.81 mM, 0 µL, 100 µL, 200 µL, and 300 µL were added to obtain the four concentrations mentioned above respectively.

Two ME-MP2RAGE protocols were acquired for experiment #3. These protocols were the same as in experiment #2 (i.e., SM2A and SM2B) that were described in section 3.4. To be coherent with the naming convention, these two protocols were named SM3A and SM3B while both protocols shared the same acquisition parameters of SM2A and SM2B respectively, except that 96 excitations (or slices) were used instead of 88 (See Table 3.5 for details).

For both ME-MP2RAGE protocols, 3-point Dixon was used to calculate fat-water separated MP2RAGE images. For SM3A, c_1 was 0.5 and c_2 3.0 for $RAGE_1$ with 0.8 and 3.0 for c_1 and c_2 of $RAGE_2$. For SM3B, c_1 and c_2 of 0.9 and 3.0 were chosen for $RAGE_1$ whereas 0.5 and 3.0 for c_1 and c_2 of $RAGE_2$. The fat-water separated MP2RAGE images were then used to produce fat and water specific T_1 maps for both protocols. The mean and standard deviations were calculated from ROIs created as explained in section 3.3 for fat and water specific T_1 maps. However, because the vials were smaller than those used in experiments #1 and #2, a radius of 4 mm was used instead of 8 mm. Moreover, relaxivity measurements were performed with the mean water R_1 values across the concentrations of GBCA corrected for the real volume of water inside vials for all fat fractions.

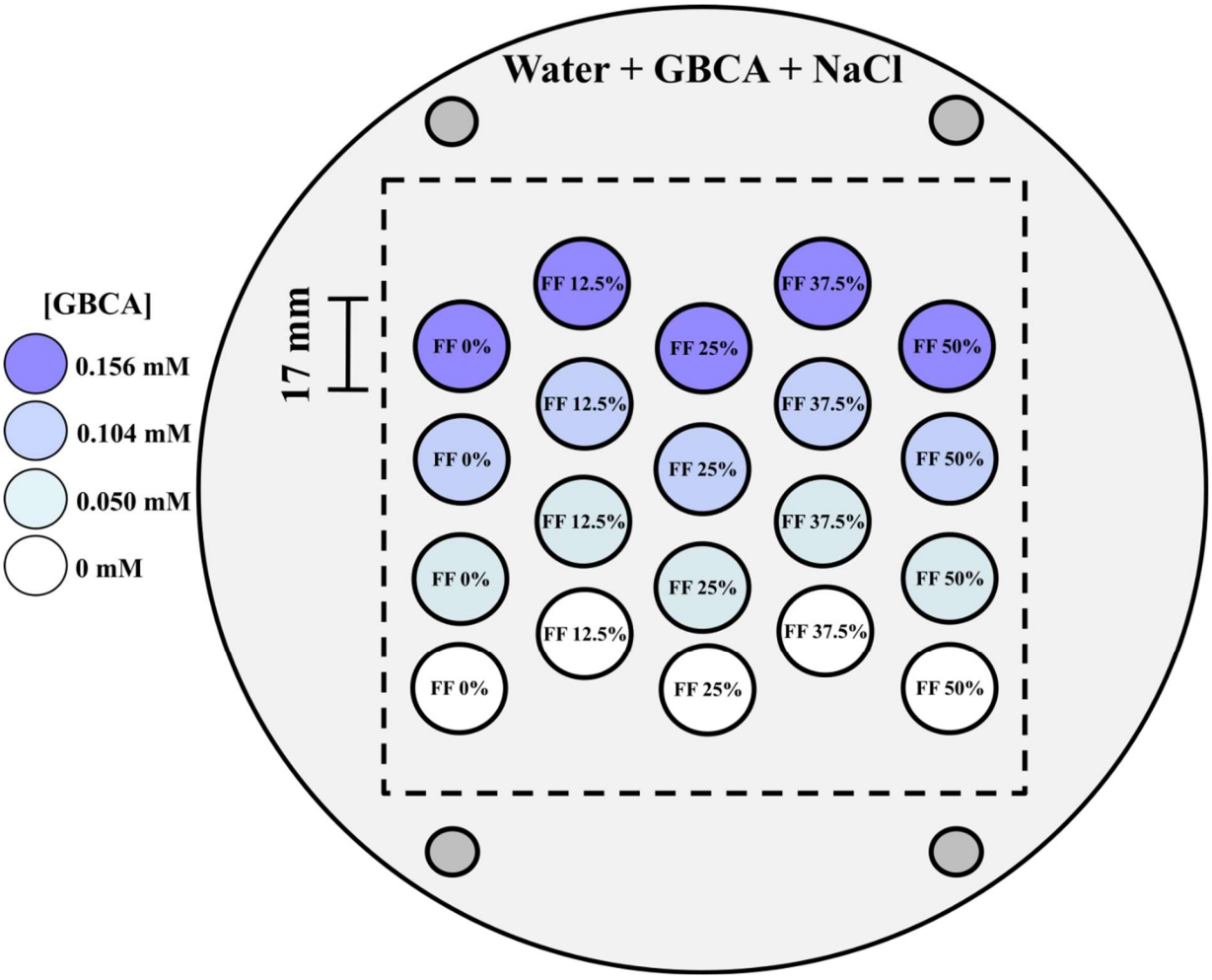

Figure 3.3 *- Phantom #3 containing 20 vials of 15 mL with different concentration of GBCA and fat fractions (FF) used in experiment #3. The concentrations of GBCA were calculated for the total vial volume and are associated with a shade of blue shown on the left. Fat fractions are written inside each vial and are expressed in weight per volume. The large compartment contained water with NaCl and GBCA.*

Chapter 4

Results

Section 4.1 presents the results from the qualitative assessment of the MP2RAGE protocol. The impact of individual acquisition parameters on the MP2RAGE lookup table and the newly designed short T_1 MP2RAGE protocols are presented. Section 4.2 presents the results from numerical simulations. Global T_1 maps produced from experiment #1 and relaxivity measurements are presented in section 4.3. In section 4.4, the global, fat and water T_1 maps produced from all ME-MP2RAGE protocols are presented in addition to the relaxivity measurements. Finally, section 4.5 presents the quantitative assessment of the two fat-water separated ME-MP2RAGE protocols acquired for a wide range of T_1 values and fat fractions.

4.1 Qualitative assessment of MP2RAGE protocol for short T_1 mapping

Through trial-and-error and visual assessment, several combinations of acquisition parameters were tested to design a MP2RAGE protocol for the T_1 range of interest between 200 and 800 ms. Ultimately, two highly similar short T_1 MP2RAGE protocols respecting the two design conditions for short T_1 optimization were found. Version A of the newly designed short T_1 MP2RAGE protocol and an example of a MP2RAGE protocol optimized for brain T_1 mapping are shown on Figure 4.1 a). The look-up tables from two versions of the new short T_1 MP2RAGE protocols are shown in Figure 4.1 b). From Figure 4.1 b), it can be observed that the two newly designed MP2RAGE protocols for short T_1 mapping are (1) monotonic across all T_1 values and (2) as linear as possible inside the T_1 range of interest. Minor "clipping" is seen for T_1 values longer than 4.5 s for version B of the short T_1 protocol whereas version A did not reach the minimum MP2RAGE signal value of -0.5. Moreover, version B of the short T_1 protocol had a slightly higher MP2RAGE signal resolution since a larger range of MP2RAGE signal values described the same short T_1 range of interest. The monotonic condition is also met for the MP2RAGE protocol designed for brain T_1 values as seen with Figure 4.1 a). However, the brain

T_1 MP2RAGE protocol is monotonic because of the clipping process. Without the clipping process, the brain T_1 MP2RAGE protocol would have considerable overlapping for T_1 values longer than approximately 2.8 s. The clipping process considerably reduced the available T_1 range for the brain T_1 protocol. Regarding design condition #2, the brain T_1 MP2RAGE protocol was linear between 1000 and 2000 ms approximately which is beyond the short T_1 range of interest defined for this project.

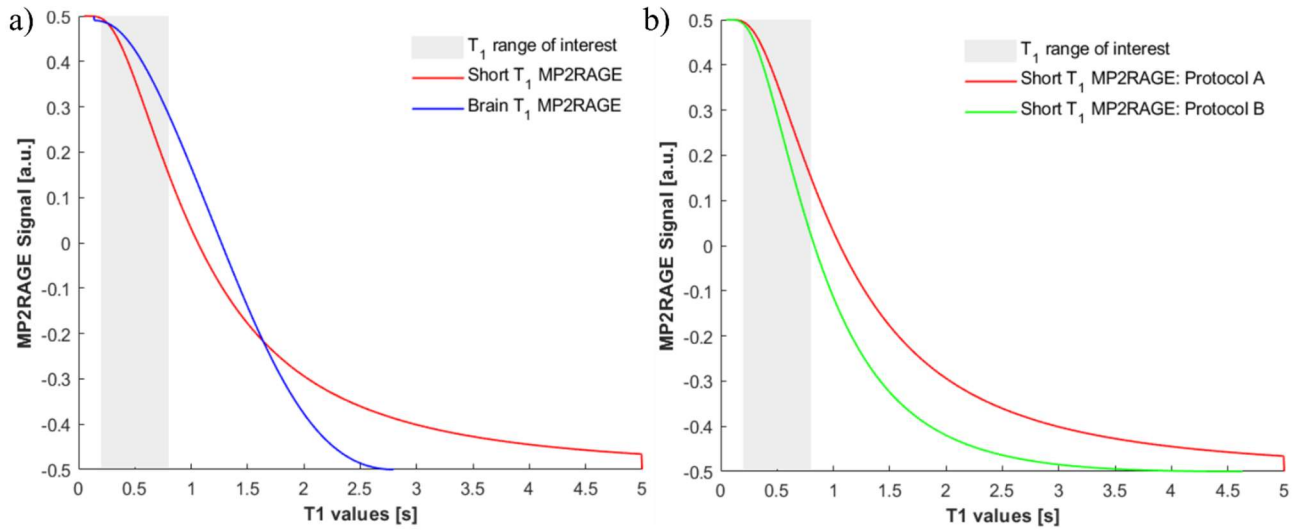

Figure 4.1 *- Visual comparison of the MP2RAGE-T_1 lookup tables produced from combinations of acquisition parameters for short T_1 (protocol A) and brain T_1 MP2RAGE protocols (a). Visual comparison of two MP2RAGE-T_1 lookup tables designed for short T_1 protocols (b). The short T_1 range of interest is shown with a grey area.*

For the qualitative assessment of individual acquisition parameters on MP2RAGE lookup tables, version A of the short T_1 protocol was used as the starting point as presented with Figure 4.2 a). The impact of varying both TIs (b), TI_1 (c) and TI_2 only (d) are also shown on Figure 4.2. The TR used for these TI variations had to be decreased to 3 ms (instead of 6 ms) because short TI_1 values could not be reached due to timing constraints in the sequence.

By increasing the values of both TIs while keeping the difference between the TIs constant (Figure 4.2 b)), the MP2RAGE signal values increased for a constant T_1 value. The increase in MP2RAGE signal values was larger for longer T_1 values and minimal for the maximum MP2RAGE signal value at +0.5 where the differences between the different curves were null. For the black curve on Figure 4.2 b), once the MP2RAGE-T_1 lookup table reached the minimum signal value, the curve started increasing again and the curve began to be larger than the blue and red curves. The black curve is an example of a MP2RAGE lookup table with no clipping of the overlap. Once the minimum signal value is reached, the impact of modifying both TIs described earlier was inverted.

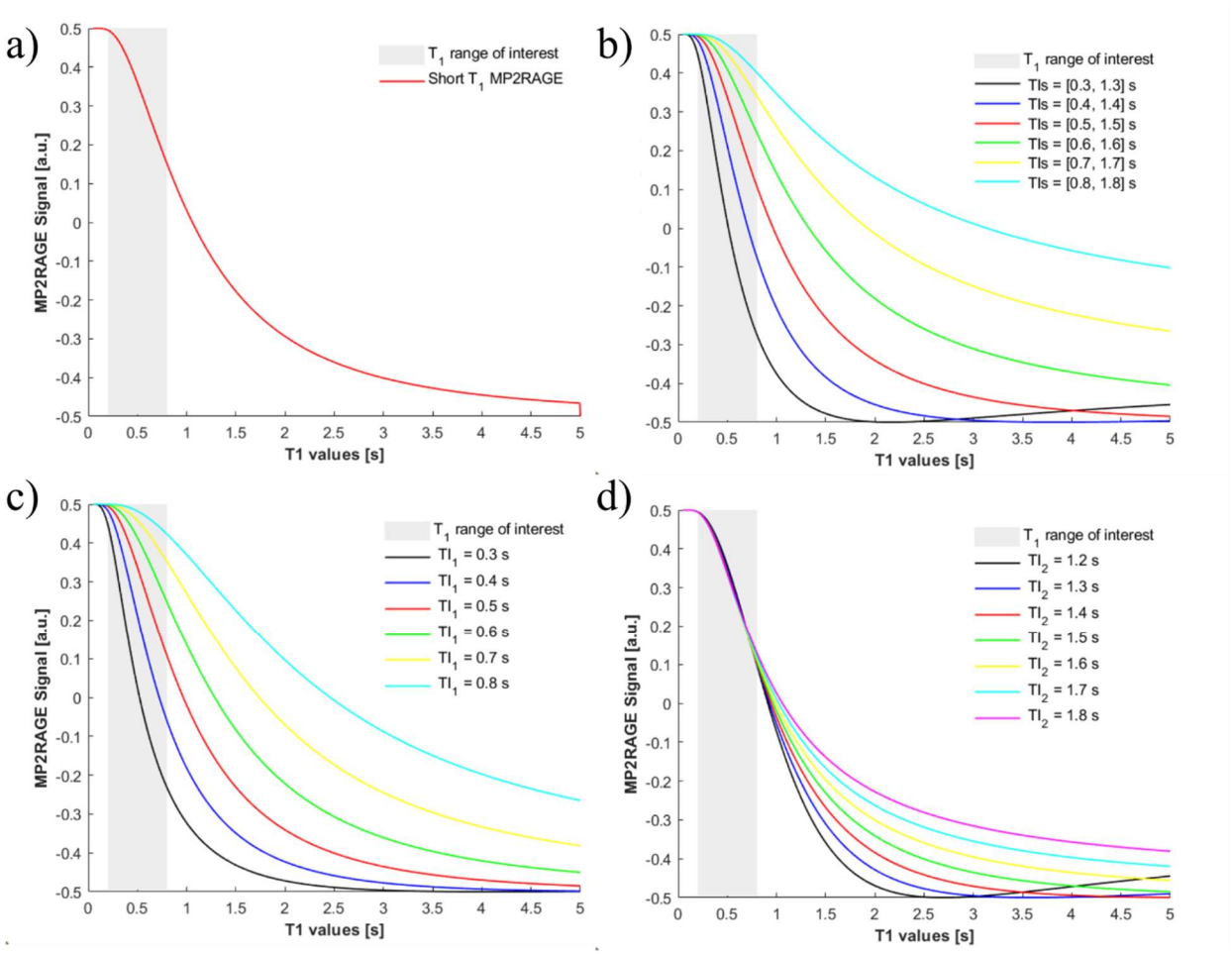

Figure 4.2 *- Impact of varying one input parameter while keeping the other parameters constant for both TIs (b), TI_1 (c) and TI_2 (d). In a), the red curve represents version A of the short T_1 protocol. The TR used for these figures required to be reduced to 3 ms (instead of 6 ms) because otherwise, combinations of input parameters were not feasible.*

Increasing one of the TIs while keeping the other constant also increased the MP2RAGE signal value for a given T_1 value, as seen in Figure 4.2 c) and d). The impact was larger for TI_1 compared to TI_2. The increase in T_1 values created by increasing TI_1 was similar as the increase seen by modifying both TIs but slightly inferior. For variations in TI_2, the short T_1 values under 800 ms were substantially less affected. In fact, a very limited decrease in MP2RAGE signal was observed for short T_1 values under 800 ms. However, for T_1 values longer than 800 ms, MP2RAGE signal values increased as the TI_2 value increased for a constant T_1 value. That increase was also observed for TI_1 and both TIs. Nevertheless, the T_1 increase for TI_2 was significantly lower than TI_1 and both TIs.

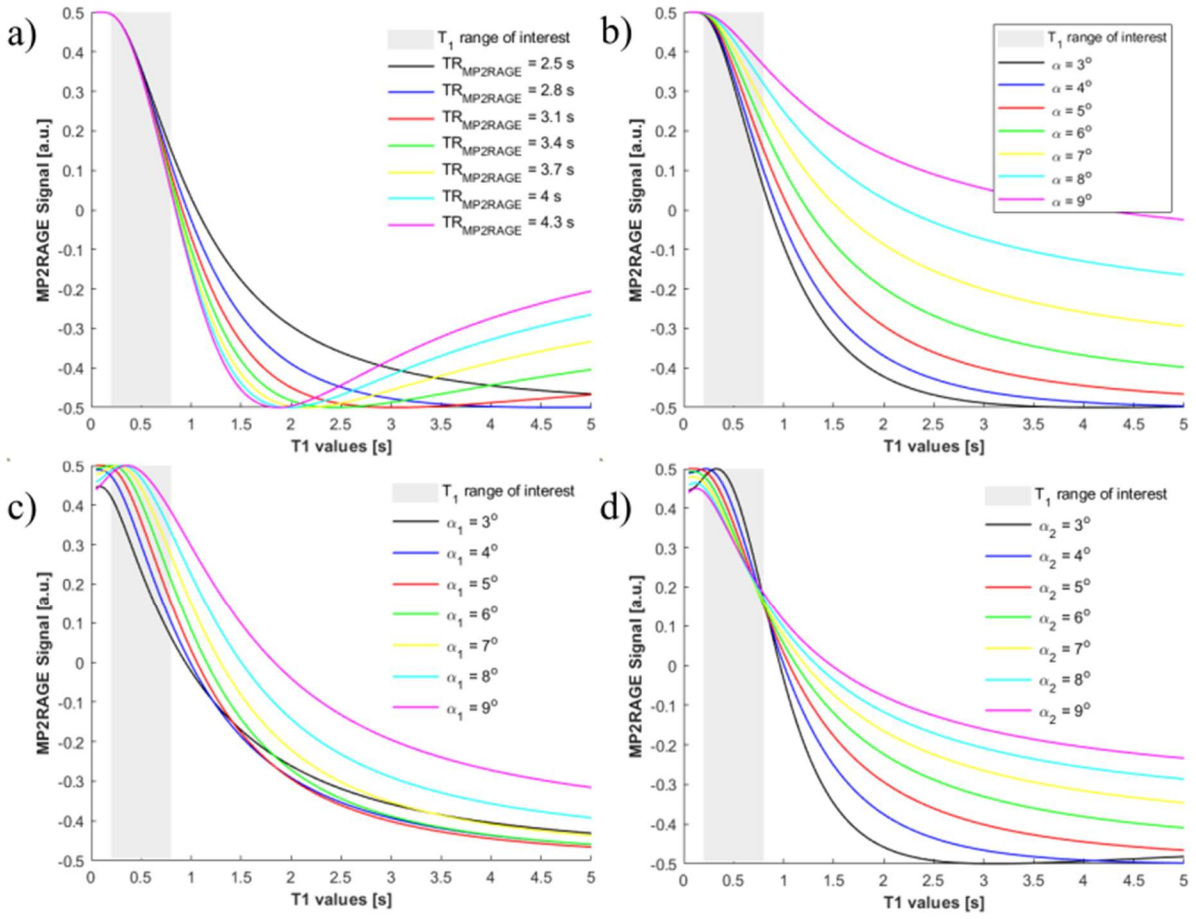

Figure 4.3 *- Effects on the MP2RAGE lookup table by varying one input parameter while keeping the other parameters constant for $TR_{MP2RAGE}$ (a), both FAs (b), FA_1 (c) and FA_2 (d).*

As visible from Figure 4.3, varying both FAs (b) revealed to be the parameter with the largest impact on the MP2RAGE lookup table. The impact of varying the $TR_{MP2RAGE}$ (a), only FA_1 (c) and only FA_2 (d) are also shown on Figure 4.3. Increasing the $TR_{MP2RAGE}$ value resulted in smaller MP2RAGE signal values for a constant T_1 values. The increase of $TR_{MP2RAGE}$ considerably reduced the T_1 value where the minimum MP2RAGE signal value is reached and consequently increased the curve overlap. Moreover, the impact of variations of $TR_{MP2RAGE}$ on the MP2RAGE-T_1 lookup table was minimal at short T_1 values.

Modifying both FAs affected the lookup table in a similar fashion to modifying both TIs. Larger FAs resulted in a growth of the T_1 values for a constant MP2RAGE signal value. The difference between the different lookup tables produced by different pairs of FAs increased as smaller MP2RAGE signal values were reached.

By modifying FA_1 only, the opposite was observed for the largest MP2RAGE signal values. Indeed, the maximum MP2RAGE signal value was reached at a longer T_1 value with increasing FA_1. The impact of varying FA_1 only was inferior to the impact of FA_2 alone or both FAs across all MP2RAGE signal values. For variations in FA_1 only, the impact on the lookup tables was not evident for $FA_1 < 7^o$. The lookup tables produced for $FA_1 < 7^o$ evolved with a behavior difficult to pin down exactly across MP2RAGE signal values smaller than 0.

When only FA_2 was modified and FA_1 was kept constant, an increase in MP2RAGE signal values was observed for T_1 values longer than 800 ms approximately. The effect was inverted for T_1 values shorter than 800 ms where increasing FA_2 resulted in a decrease of MP2RAGE signal values for a constant T_1. The T_1 value where the maximum signal value (+0.5) was reached was slightly reduced with larger FA_2.

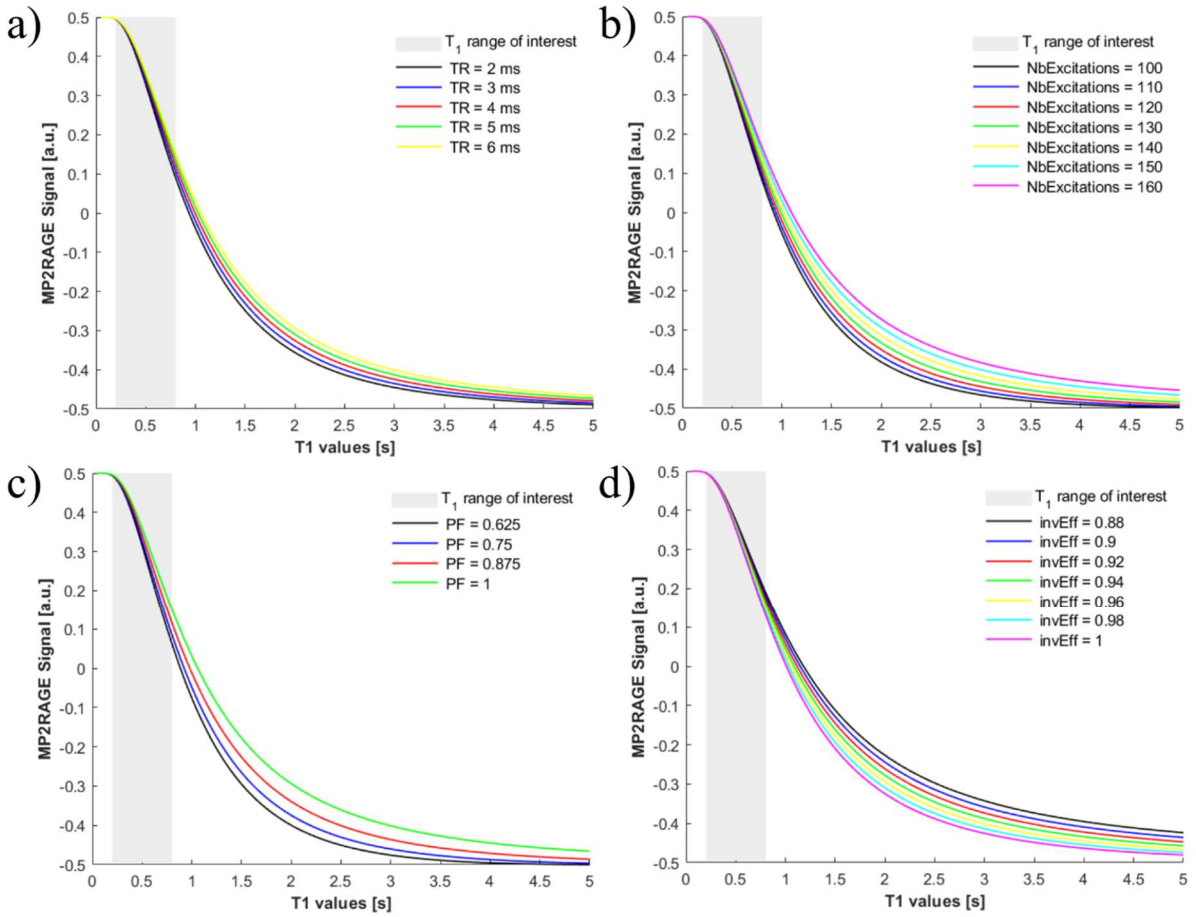

Figure 4.4 *- Input parameters with limited impact on the MP2RAGE lookup table. Effects of varying the TR (a), number of excitations (b), PF factor (c) and invEff (d) while keeping the other parameters constant are shown.*

The three acquisition parameters and inversion efficiency of the adiabatic inversion pulse presented on Figure 4.4 showed the least impact of the MP2RAGE lookup table. The four acquisition parameters with limited impact on the lookup table were the TR (a), number of excitations (b), PF (c) and invEff (d) respectively. By increasing the TR, MP2RAGE signal values were increasing for a constant T_1 value. The impact was limited but still noticeable. The TR values used were constrained by the TIs selected for version A of the short T_1 MP2RAGE protocol. For the number of excitations (b), the same behavior as TR was observed: a limited MP2RAGE signal value increase for a constant T_1 value. Regarding PF (c), an increase in PF value resulted in a slight increase of the MP2RAGE signal values for a constant T_1 value like the

two previous parameters. Finally, for invEff, an increase of the inversion efficiency resulted in a decrease of the T_1 values for a constant MP2RAGE signal value. These last four acquisition parameters had a negligeable impact at larger MP2RAGE signal values (or equivalently short T_1 values).

4.2 Quantitative assessment of MP2RAGE protocol optimized for short T_1 mapping with numerical simulations

After finding two combinations of acquisition parameters that visually seemed optimized for short T_1 values and investigating the impact of every parameter individually on the MP2RAGE-T_1 lookup table, numerical simulations were performed. Since the two short T_1 MP2RAGE protocols gave extremely similar results, only the results from version A of the short T_1 MP2RAGE protocol are shown in comparison with the brain T_1 protocol. However, when noticeable differences between version A and B were observed, results from both versions of the short T_1 protocol are shown. Moreover, the results calculated from a SNR value of 25 only are shown because the SNR value only affected the scaling of the accuracy and precision calculated while not affecting the overall behavior of the results.

As seen in Figure 4.5, the 10 000 noisy lookup tables of version A of the short T_1 protocol (a) showed less T_1 variability than the noisy lookup tables calculated for the brain T_1 protocol (b) inside the T_1 range of interest between 200 ms and 800 ms. Moreover, version A of the short T_1 protocol produced T_1 estimates dispersed in a smaller range than T_1 estimates of brain T_1 protocol up to somewhere between 1.0 s and 1.5 s. However, for longer T_1 values, the noisy lookup tables calculated from the short T_1 protocol version A were distributed across a wider range of MP2RAGE signal values in comparison with the brain T_1 protocol. Beyond a T_1 of approximately 2.8 s, comparisons between the short and brain T_1 protocols could not be done due to the clipping of the brain T_1 lookup table. For both protocols shown on Figure 4.5, the variability of T_1 estimates increased as T_1 values increased.

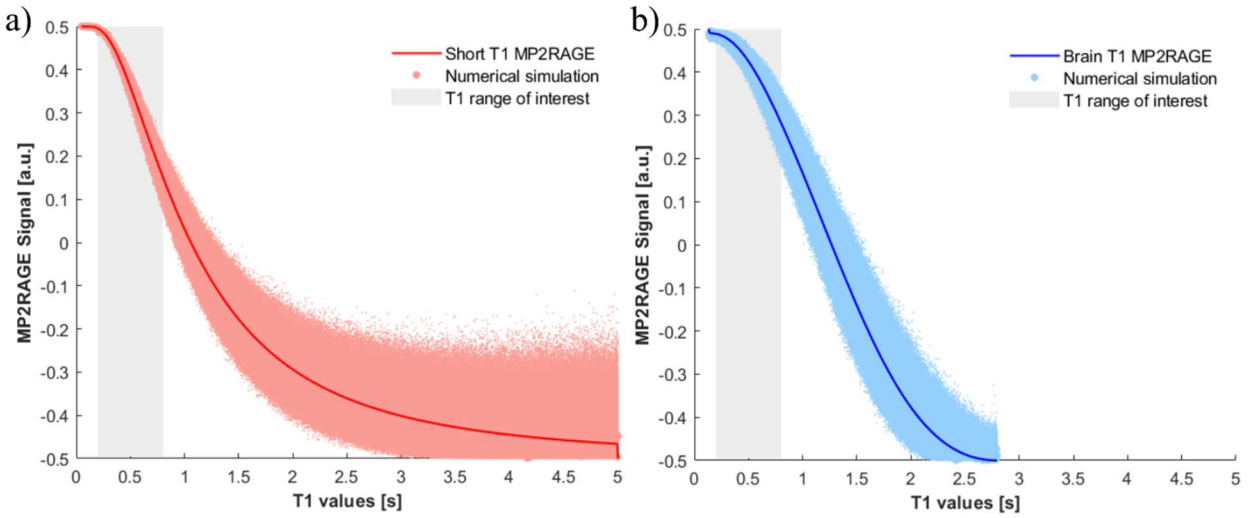

Figure 4.5 *- Results of numerical simulations for version A of the short T_1 MP2RAGE protocol (a) and the brain T_1 MP2RAGE protocol (b). The two noiseless MP2RAGE-T_1 lookup tables are shown with the thick red and blue lines respectively. The dots represent the 10 000 noisy variations of the noiseless lookup table (thick line).*

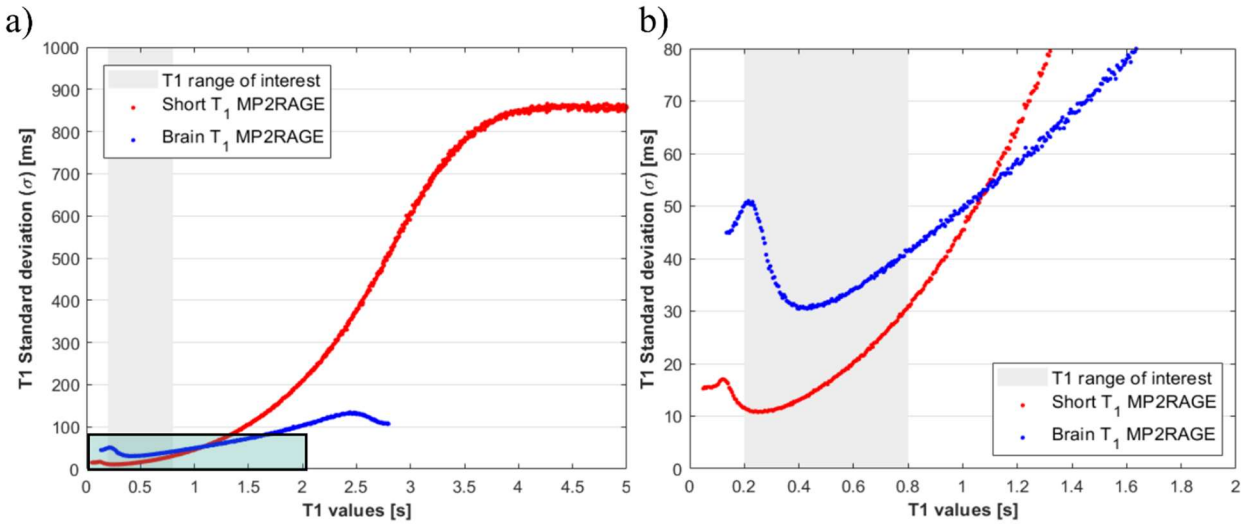

Figure 4.6 *- Precision measurements from numerical simulations for the short T_1 (red) and brain T_1 (blue) protocols. Subfigure b) corresponds to the light blue square portion of subfigure a). Precision corresponded to the standard deviation of the 10 000 normally distributed points with noise.*

From the precision calculated from numerical simulations shown on Figure 4.6 a), the visible increase in T_1 variability on Figure 4.5 with increasing T_1 values was confirmed. Overall, the precision decreased with increasing T_1 values. However, for a narrow range of T_1 values at the beginning and end of the T_1 range (i.e., shortest, and longest T_1 values), the standard deviations decreased with increasing T_1 values for both protocols. Moreover, the short T_1 protocol was more precise than the brain T_1 protocol up to 1.0 s approximately. For T_1 values longer than 1.0 s, the short T_1 protocol became rapidly less precise than the brain T_1 protocol. The minimum standard deviation calculated for the short T_1 protocol was 11 ms at a T_1 of 250 ms in comparison with 31 ms at 440 ms for the brain T_1 protocol. In summary, the short T_1 protocol had a better precision than the brain T_1 protocol up to 1 s where the brain T_1 protocol was considerably more precise for higher T_1 values.

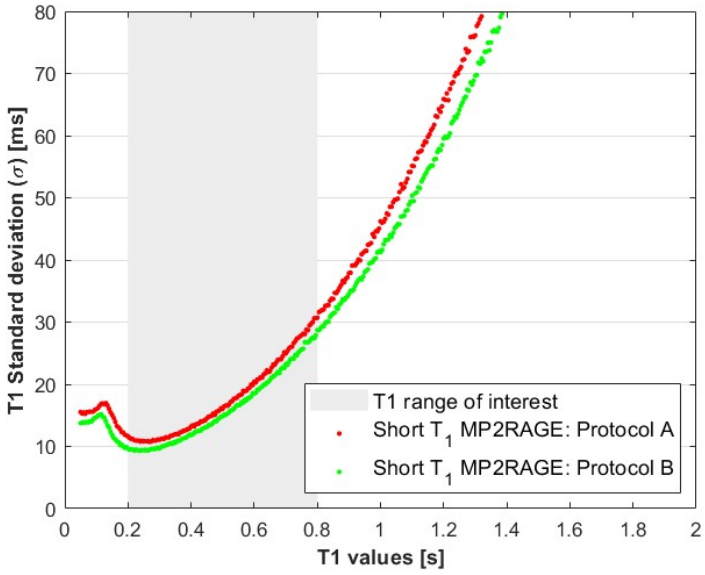

Figure 4.7 *- Standard deviations calculated from numerical simulations for version A (red) and B (green) of the short T_1MP2RAGE protocol. Version A is the short T_1 protocol used for all figures where short T_1 protocol is compared against the brain T_1 protocol.*

The standard deviations calculated from numerical simulations varied sightly between the two versions of the short T_1 protocols as presented with Figure 4.7. Version B was slightly more precise than version A. The increase in MP2RAGE "signal resolution" of version B of the short T_1 MP2RAGE protocol in comparison with version A was barely noticeable from the results of

numerical simulations. For accuracy, no difference was measured between the two versions of the short T_1 protocol.

Figure 4.8 b) shows that the short T_1 protocol was more accurate for T_1 values shorter than 0.8 s and had comparable accuracy between 0.8 s and 1.0 s with the brain T_1 protocol. Beyond 1.0 s, the short T_1 protocol started to overestimate the mean T_1 values calculated from simulations until it reached a maximum value around 3.5 s. Once the maximum T_1 overestimation was reached, the T_1 overestimation started to considerably decrease to reach a T_1 region at the end of the T_1 range where the mean T_1 values were underestimated. A similar underestimation of the mean T_1 values was also present for the longest T_1 values of the brain T_1 protocol. Moreover, a short

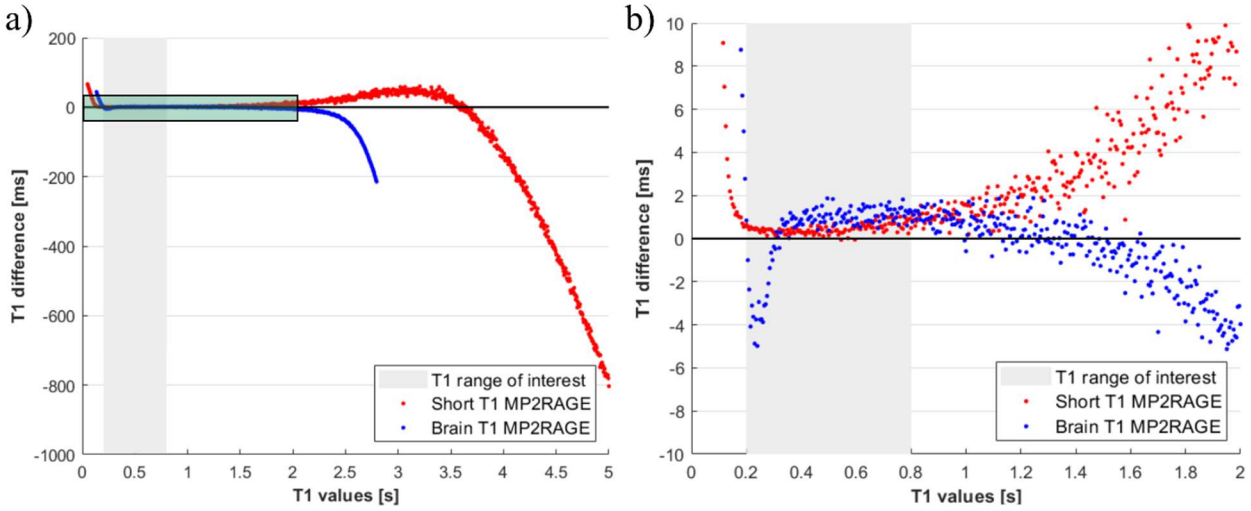

Figure 4.8 *- Accuracy measurements from numerical simulations (a). In b), a zoomed version of a) is shown corresponding to the light green square on a). Accuracy corresponded to the difference between the mean of the 10 000 simulated T_1 values and the theoretical noiseless T_1 value.*

region of T_1 overestimation at very short T_1 values (i.e., $T_1 < 0.2$ s) could be observed for both protocols. For the brain T_1 protocol, the T_1 overestimation was slightly shifted towards longer T_1 values. By looking at Figure 4.8 b), it is possible to see that the small T_1 overestimation region at very short T_1 values was followed by a narrow T_1 range of underestimation for the brain T_1 protocol. The underestimation region at short T_1 values was not present for the short T_1 protocol. In summary, the short T_1 protocol was more accurate than the brain T_1 protocol for T_1 values shorter than 0.8 s approximately. For T_1 values between 0.8 and 1.0 s, both protocols had highly

similar accuracy levels. After T_1 of 1.0 s, the brain T_1 protocol showed a better accuracy than the short T_1 protocol.

The numerical simulations successfully demonstrated that the short T_1 MP2RAGE protocol had a better or comparable theoretical accuracy and precision up to T_1 values around 1.0 s than the brain T_1 MP2RAGE protocol.

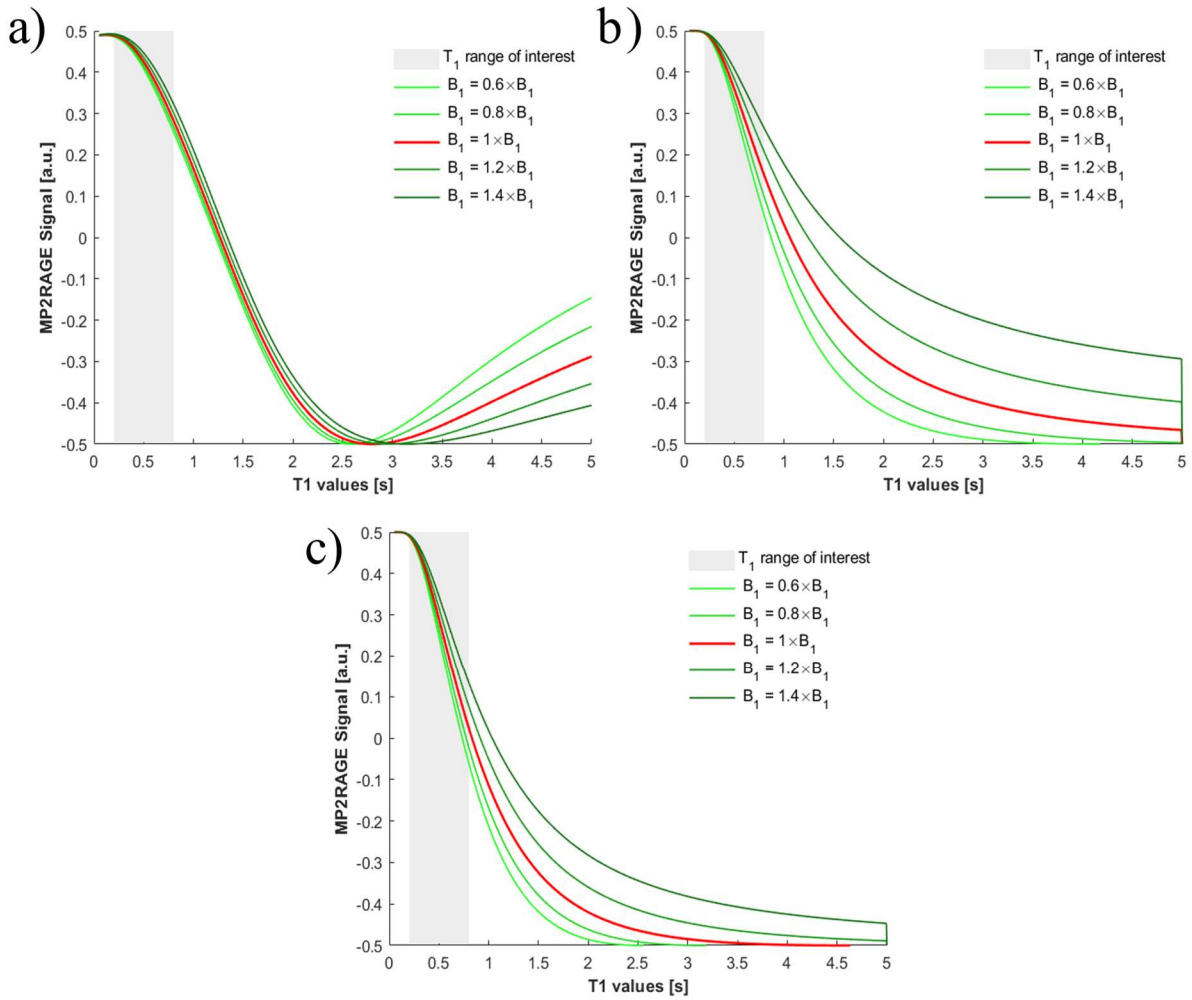

Figure 4.9 *- B_1^+ theoretical sensitivity of the brain T_1 protocol (a), short T_1 protocol version A (b) and short T_1 protocol version B (c). B_1^+ variations of +/- 20% and 40% were used.*

Overall, the brain T_1 protocol (a) was by far the least sensitive MP2RAGE protocol to variations in B_1^+ values in comparison with both versions of the short T_1 MP2RAGE protocols (b and c). The B_1^+ sensitivities are shown in Figure 4.9. Version A of the short MP2RAGE protocol (b) was

the most sensitive MP2RAGE protocol. Indeed, version B of the short T_1 protocol (c) was slightly less affected by B_1^+ variations than the other short T_1 MP2RAGE protocol. A common feature for the three protocols was that the discrepancies due to B_1^+ variations increased with increasing T_1 values. Thus, for all protocols, the impact of B_1^+ inhomogeneities were less important for the short T_1 values. In other words, the T_1 range of interest of this work was theoretically less affected by B_1^+ variations than the rest of the T_1 values.

4.3 Experimental validation of the short T_1 MP2RAGE protocol.

With experiment #1, the newly developed MP2RAGE protocol for short T_1 mapping showed high accuracy and precision levels similar or even better than the brain T_1 MP2RAGE protocol for global T_1 mapping. The global T_1 maps produced for the six different protocols acquired are presented in Figure 4.10. All global T_1 maps produced were visually similar to the reference (a). One visible characteristic was that protocol SS1A (b) produced the noisiest global T_1 maps. Overall, the global T_1 values inside the large compartment across all MP2RAGE protocols were noisier than the reference large compartment. Another noticeable aspect was the slight Gibbs' ringing artifacts near high contrast regions between the vials and the large compartment for the global T_1 maps produced from SM1 (f, g and h). Visually, SS1C (d) and LS1 (e) produced the most uniform T_1 values inside the large compartment. The global T_1 maps produced from the three echoes of SM1 were highly similar visually.

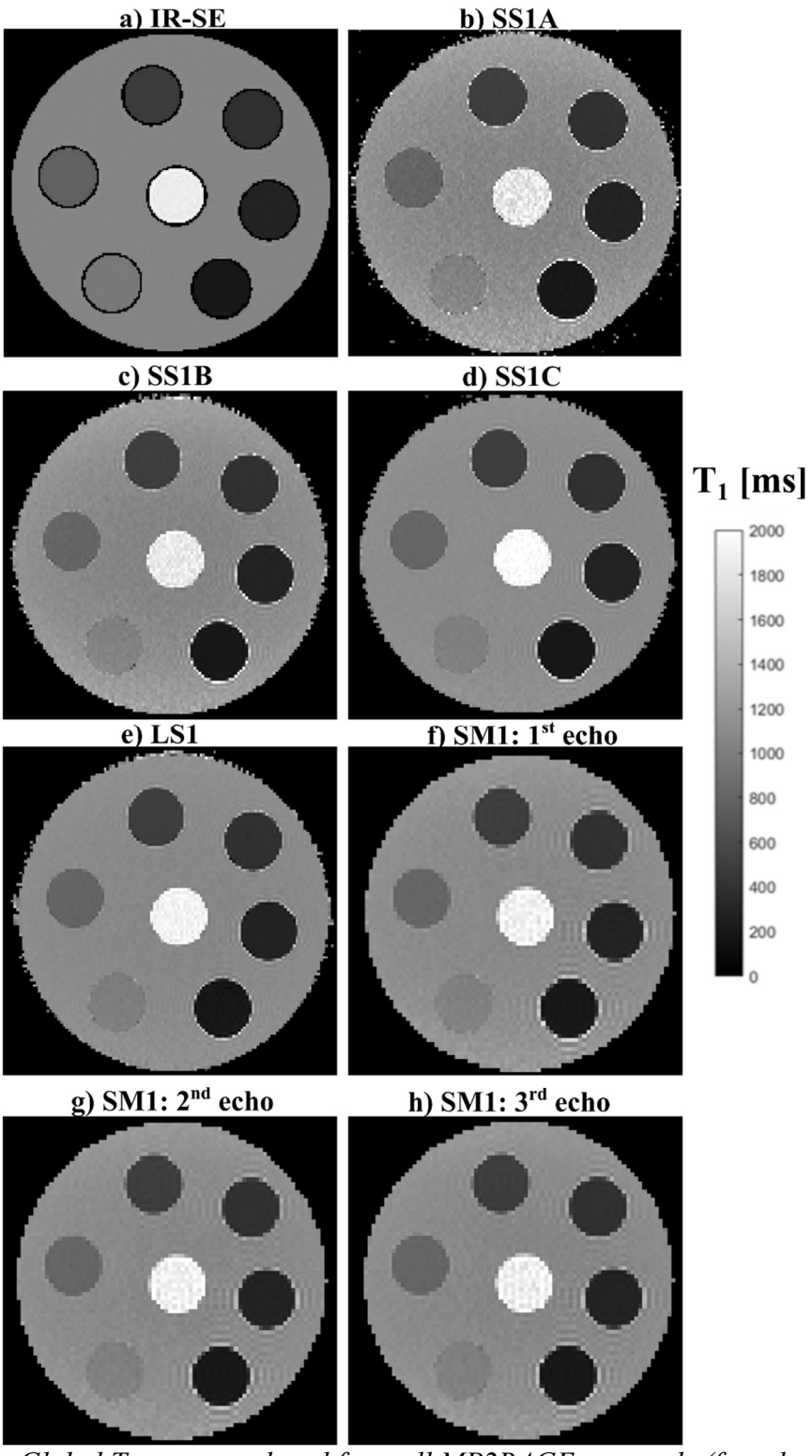

Figure 4.10 *- Global T_1 maps produced from all MP2RAGE protocols (from b to h), and the reference technique (a) acquired during experiment #1. All global T_1 maps shown represent the same slice location as the reference and have the same T_1 scale.*

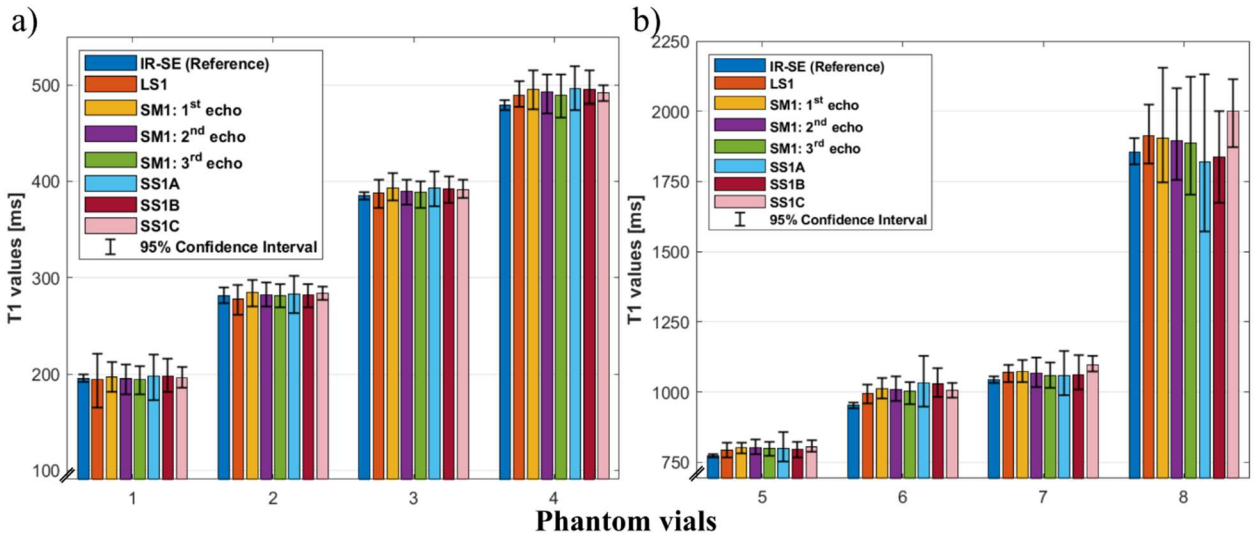

Figure 4.11 *- Bar plots showing the mean global T_1 and 95% confidence interval of all voxels inside the ROI of each vial for experiment #1. The T_1 axis are cut on both subfigures for better visualization.*

By calculating the 95% CIs, it was found that the mean global T_1 values calculated inside ROIs from all MP2RAGE protocols overlapped with the reference technique for vials #1, #2, #3, #4 and #8. The mean global T_1 values and their corresponding 95% CIs for every vial and protocol acquired during experiment #1 are shown on Figure 4.11. For vial #5, all protocols overlapped with the reference except the first two echoes of SM1 and SS1C. Only LS1, SM1 3rd echo and SS1A overlapped with the reference for vial #6. Vial #6 was the vial with the least MP2RAGE protocols overlapping with the reference technique. For vial #7, all MP2RAGE protocols overlapped with the reference except SS1C. SS1C was the protocol with the fewest mean global T_1 values overlapping with the reference, without overlap for vials #5, #6 and #7. However, SS1C was the most precise MP2RAGE protocol through all vials. Conversely, SS1A was the least precise MP2RAGE protocol. LS1, SM1: 3rd echo and SS1A were the only MP2RAGE protocols that overlapped with the reference technique for all vials. Overall, no outliers were observed among MP2RAGE protocols. Table 4.1 shows the mean global T_1 values and standard deviations calculated inside vials for protocols acquired during experiment #1.

SM1 produced highly similar mean global T_1 values and 95% CIs across the three echoes. In fact, the mean global T_1 calculated decreased in a very limited fashion with increasing TE. As

predicted from numerical simulations, LS1 was the least precise protocol for vial #1. This was not the case for the other vials, however. Moreover, LS1 was the most accurate MP2RAGE protocol only for vial #5 and #6 whereas it would have been expected that LS1 would be the most accurate for the vials with the longest T_1 values (i.e., vials #7 and #8).

Table 4.1 *- Mean global T_1 values and standard deviations for all vials and protocols acquired during experiment #1.*

Vial	IR-SE	SS1A	SS1B	SS1C	LS1	SM1 (echo 1)	SM1 (echo 2)	SM1 (echo 3)
1	196 ± 2	198 ± 11	198 ± 9	196 ± 6	195 ± 14	197 ± 8	196 ± 8	194 ± 8
2	281 ± 6	283 ± 9	282 ± 6	284 ± 4	278 ± 8	285 ± 7	282 ± 7	282 ± 6
3	385 ± 2	393 ± 10	392 ± 7	391 ± 5	388 ± 8	393 ± 7	390 ± 6	389 ± 7
4	479 ± 3	496 ± 11	495 ± 8	492 ± 4	490 ± 7	495 ± 11	492 ± 11	489 ± 11
5	772 ± 3	799 ± 27	796 ± 16	806 ± 9	792 ± 12	801 ± 10	803 ± 14	799 ± 13
6	953 ± 5	1034 ± 46	1031 ± 27	1005 ± 15	995 ± 18	1011 ± 20	1010 ± 22	1003 ± 20
7 (Large compt.)	1045 ± 6	1060 ± 40	1061 ± 31	1097 ± 13	1069 ± 17	1075 ± 23	1067 ± 25	1058 ± 23
8	1856 ± 25	1819 ± 142	1836 ± 84	2000 ± 64	1912 ± 51	1904 ± 90	1896 ± 87	1887 ± 103

Figure 4.12 shows the high correlation of the global T_1 values calculated from protocol SM1: 3rd echo with the reference technique. A R^2 value of 0.9995 was measured. Moreover, the average difference between the mean global T_1 values of SM1: 3rd echo and IR-SE was 16.63 ms with the 95% limits of agreement from -17.69 ms to 50.95 ms as observed with the Bland-Altman plot on Figure 4.12 b). A small overestimation bias can be observed with the Bland-Altman plot with increasing mean global T_1 values. Thus, the global T_1 values calculated from SM1: 3rd echo showed great agreement with the reference. For LS1, a R^2 value of 0.9999 with an average difference of 18.88 ms (95% limits of agreement: -22.61 ms and 60.37 ms) with IR-SE were

calculated (not shown). These results were performed to compare with values reported in the literature [41].

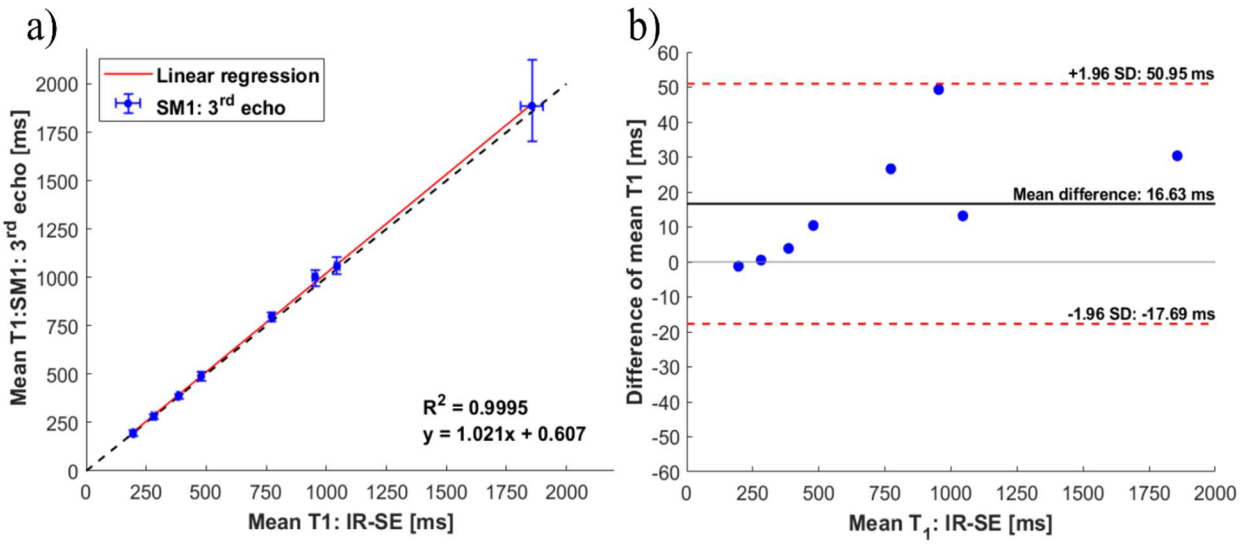

Figure 4.12 *- Correlation (a) and Bland-Altman (b) plots for the global T_1 map produced from protocol SM1: 3rd echo against the reference technique. On subfigure a), the blue dots and error bars correspond to the mean global T_1 values and standard deviations. The black dashed line corresponds to the identity line. On subfigure b), the blue dots correspond to the difference between the mean global T_1 from SM1: 3rd echo and the IR-SE.*

Figure 4.13 shows that the theoretical model used in numerical simulations could not explain the experimental accuracy (a & c) and precision (b & d) levels measured experimentally. Accuracy and precision measured experimentally and predicted from the numerical simulations are shown for two MP2RAGE protocols (SM1: 1st echo and LS1) only because all protocols showed highly similar results. For a) and c), black diamonds correspond to the difference between the mean global T_1 values calculated experimentally inside vials and the mean global T_1 measured from IR-SE inside the corresponding vials. The red (a) and blue (c) lines correspond to the difference between the mean T_1 values of the 10 000 simulated T_1 values calculated from numerical simulations and the corresponding theoretical noiseless T_1 value. For b) and d), the black diamonds correspond to the standard deviations calculated experimentally. The red (b) and blue (d) lines correspond to the theoretical standard deviation measured from numerical simulations.

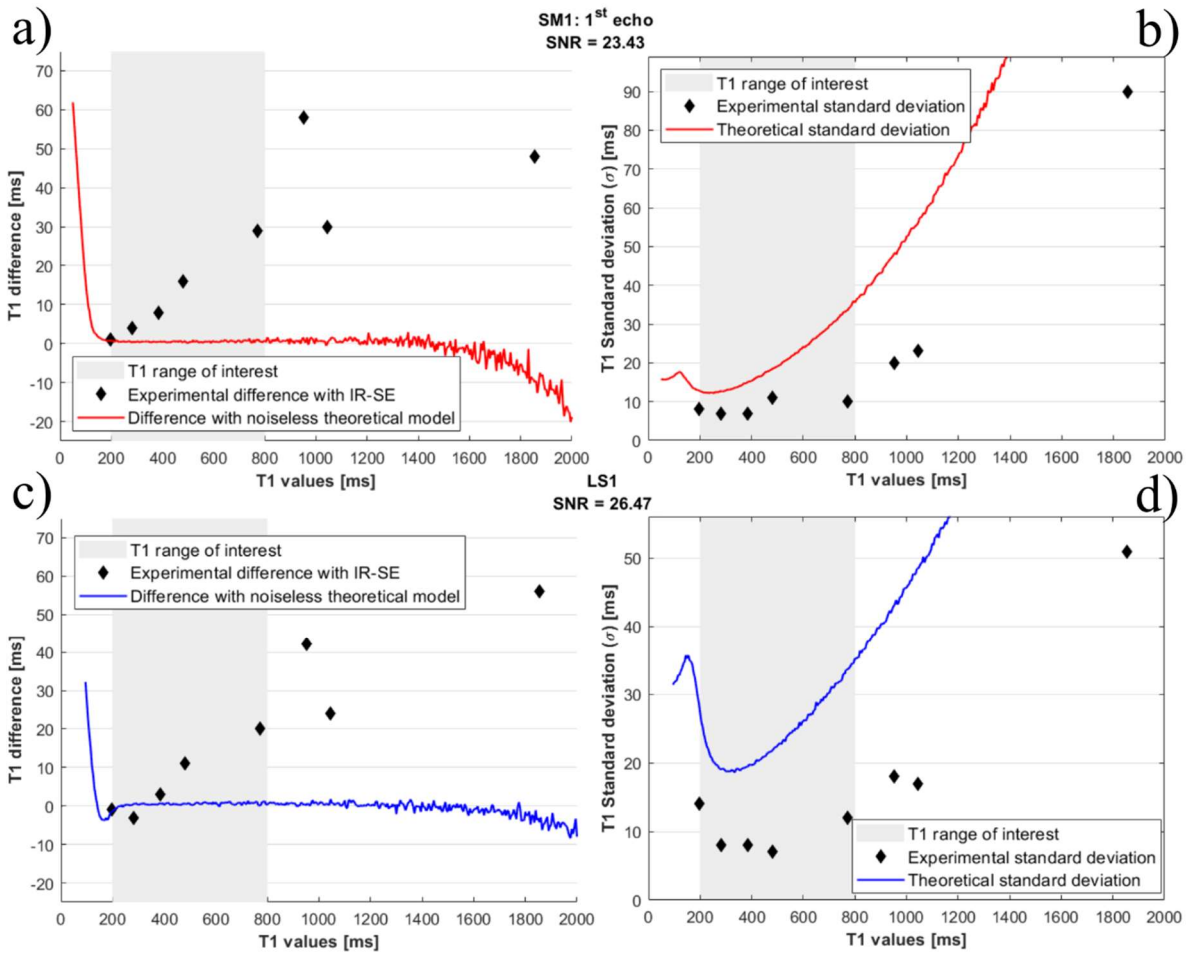

Figure 4.13 *- Comparison of experimental results of accuracy (a & c) and precision (b & d) against theoretical predictions from numerical simulations for protocol SM1 (1st echo) [a & b] and LS1 [c & d].*

The numerical simulations did not explain the deviations in accuracy measured experimentally. For both protocols, the theoretical model predicted considerably smaller discrepancies than seen experimentally for the same SNR value. In other words, the numerical simulations considerably overestimated the accuracy of both protocols. For precision, the theoretical model did not correctly predict the experimental standard deviations calculated for both protocols. In opposition with accuracy, the model predicted lower precision (i.e., larger standard deviations) and the precision measured experimentally was higher.

SM1 successfully produced a water T_1 map highly similar to the global T_1 map. The water-only T_1 map is shown and compared with the average global T_1 map on Figure 4.14. Visually, both T_1

maps were identical. The mean T_1 values and standard deviations calculated for both T_1 maps shown on Figure 4.14 are presented in Table 4.2.

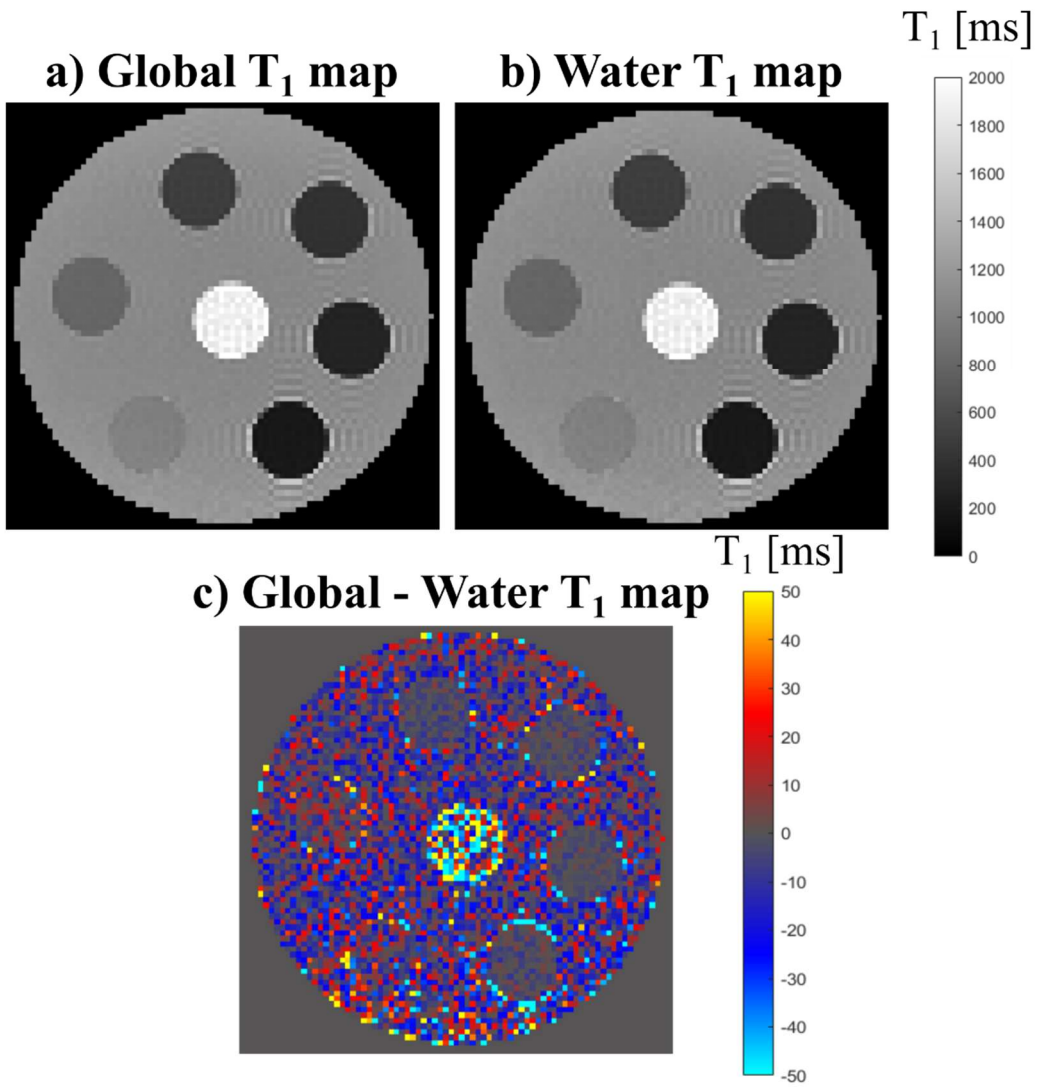

Figure 4.14 *- Global T_1 map (average of three echoes) (a) and water-only T_1 map (b) both from SM1 protocol. The two T_1 maps have the same T_1 scale and slice location. The T_1 difference map between the global and water T_1 maps is shown with a bipolar colormap in (c).*

For the water T_1 map, the four vials with the shortest mean T_1 values had the same mean T_1 values as the global averaged T_1 map. The three global T_1 maps calculated from individual echoes were averaged together to compare with the water T_1 map. For the four vials with the longest mean T_1 values, the mean T_1 values were highly comparable with a maximum difference of 4 ms between the global and water mean T_1 values. The standard deviations for the water T_1

map were always shorter or equal (for vial #4 only) to the corresponding standard deviations of global T_1 values. In other words, the water T_1 map was more precise than the global T_1 map overall. Since phantom #1 did not contain fat, the fat-only MP2RAGE images and the fat-only T_1 map looked like pure noise. The mean and standard deviations calculated from the fat-only T_1 map were meaningless and are not shown. Any signal identified as fat signal from the 3-point Dixon algorithm in phantom #1 was associated to noise in the images. On average among all vials inside the fat-only RAGE image #2, a mean fat fraction of 0.52% ± 0.83% was measured.

Table 4.2 *- Comparison between the global (average of three echoes) and water-only mean T_1 values and corresponding standard deviations calculated from protocol SM1.*

Vial	SM1: Global T1 (Average) [ms]	SM1: Water T1 [ms]
1	196 ± 8	196 ± 7
2	283 ± 7	283 ± 6
3	391 ± 7	391 ± 6
4	492 ± 11	492 ± 11
5	801 ± 13	797 ± 9
6	1008 ± 21	1004 ± 16
7 (Large compt.)	1066 ± 24	1064 ± 16
8	1895 ± 93	1889 ± 78

For experiment #1, the measured relaxivity values showed high similarity and uniformity across all protocols. The global R_1 values against the concentrations of GBCA are shown in Figure 4.15. Global R_1 values measured for all protocols showed a strong linear behavior across concentrations of GBCA. Mean global R_1 values were hardly distinguishable between protocols. The largest concentration of GBCA showed the lowest T_1 precision. The resulting slopes (i.e., relaxivity), standard deviations and R^2 values from the linear fits are shown in Table 4.3. All

relaxivity values calculated were highly comparable with similar standard deviations as well. For instance, the largest and smallest relaxivity values calculated were 4.68 ± 0.22 $s^{-1}mM^{-1}$ for LS1 and 4.59 ± 0.23 for SS1B. The maximum and minimum R^2 values calculated were 0.9993 for SM1: 3rd echo and 0.9982 for SS1B respectively.

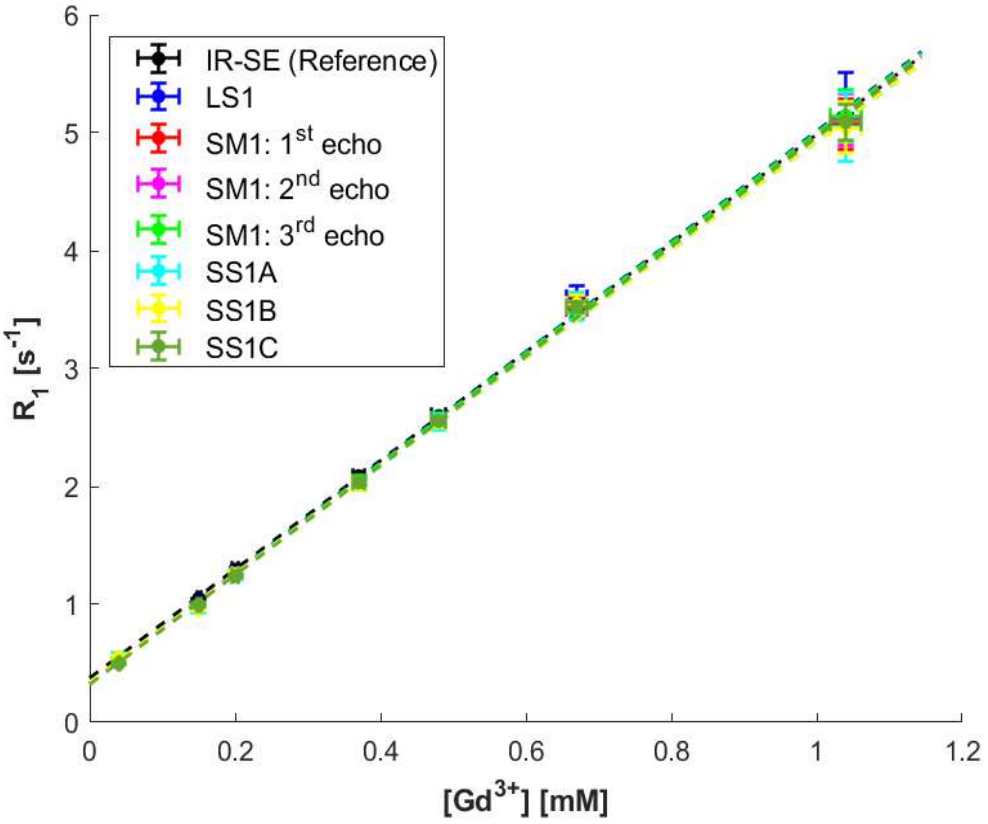

Figure 4.15 *– Global R_1 values against the concentrations of GBCA inside vials for experiment #1. The dashed lines correspond to the results of the linear fit of global R_1 values against concentrations of GBCA. The large compartment was excluded from the measurements because the concentration of GBCA was not known precisely.*

Table 4.3 *– Relaxivity values calculated from the linear fit of global R_1 values against concentrations of GBCA solution inside vials.*

Protocol	Relaxivity ± std. dev. [$s^{-1}mM^{-1}$]	R^2
IR-SE	4.61 ± 0.16	0.9992
LS1	4.68 ± 0.22	0.9985
SS1A	4.59 ± 0.21	0.9986
SS1B	4.59 ± 0.23	0.9982
SS1C	4.64 ± 0.16	0.9992
SM1 (1st echo)	4.61 ± 0.16	0.9991
SM1 (2nd echo)	4.65 ± 0.17	0.9991
SM1 (3rd echo)	4.67 ± 0.15	0.9993

4.4 Experimental assessment of fat-water separated ME-MP2RAGE protocols

Once the accuracy and precision levels of short T_1 MP2RAGE protocols were validated and the feasibility of ME-MP2RAGE protocols for fat-water separated T_1 mapping assessed experimentally, the second acquisition focused on the experimental assessment of the fat-water separated T_1 mapping from ME-MP2RAGE protocols.

The global T_1 maps produced from all protocols showed a larger variability across protocols and echo times than experiment #1 as shown by Figure 4.16. The global T_1 values inside the large compartment were highly comparable across MP2RAGE protocols. LS2 produced the least noisy large compartment among MP2RAGE protocols. As for experiment #1, both ME-MP2RAGE

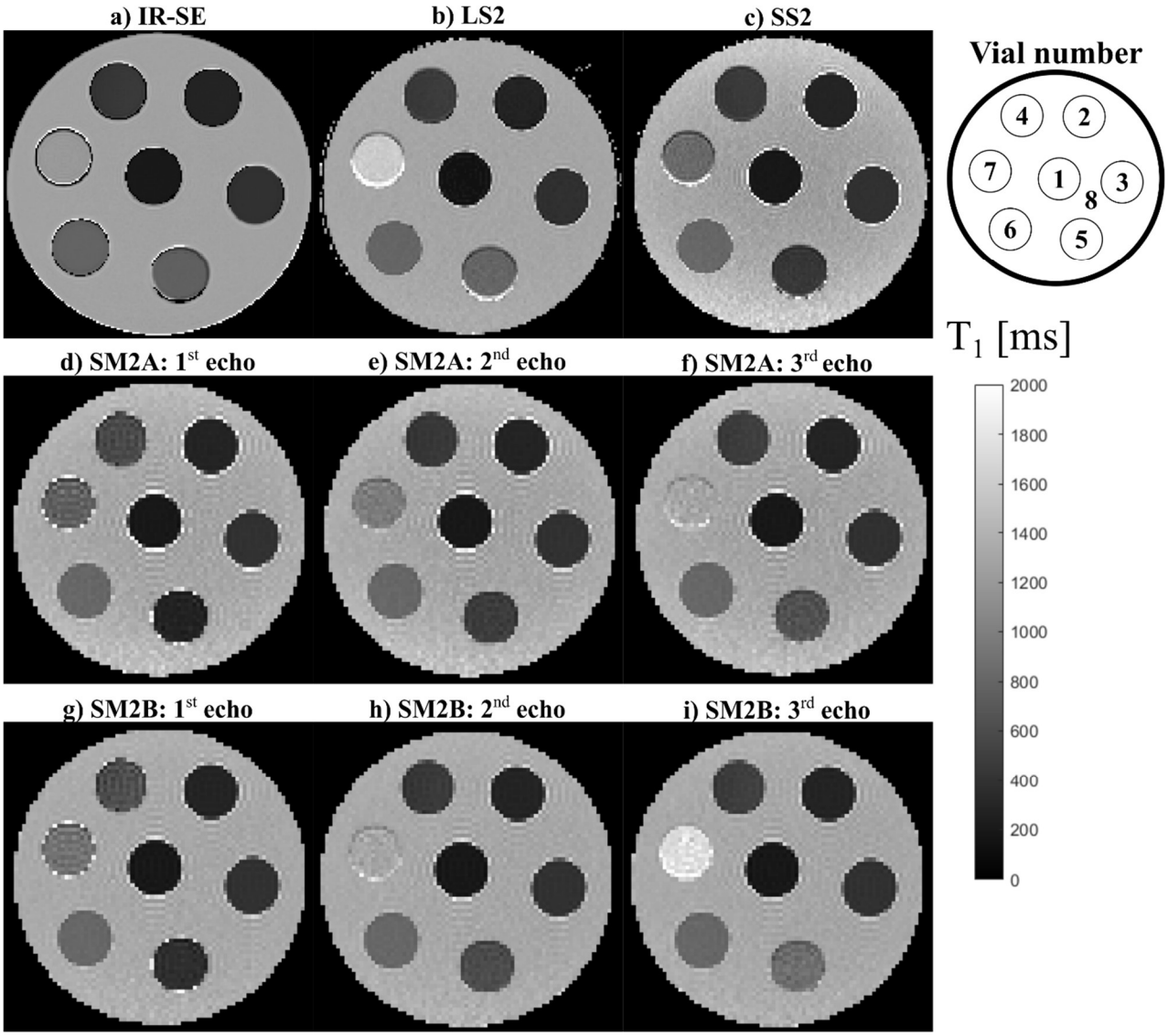

Figure 4.16 *- Global T_1 maps produced from all protocols acquired during experiment #2. All T_1 maps shown represent the same 2D slice inside the phantom and have the same T_1 scale. A small diagram to help identify vial is shown on the top right.*

protocols (SM2A and SM2B) had minor Gibbs' ringing artifacts in high contrast regions. The five vials that did not contain fat were vials #1, #2, #3, #6 and #8 (large compartment). These five vials showed great uniformity across the global T_1 maps produced from the different MP2RAGE protocols and were highly similar to the reference in addition as seen with Table 4.4.

Table 4.4 *- Mean global T_1 values and the corresponding standard deviations calculated inside all vials and protocols acquired during experiment #2*

Vial	IR-SE (Reference)	SS2	LS2	SM2A			SM2B		
				1st echo	2nd echo	3rd echo	1st echo	2nd echo	3rd echo
1	197 ± 2	193 ± 8	154 ± 25	196 ± 9	194 ± 10	194 ± 8	198 ± 15	195 ± 14	195 ± 14
2	284 ± 5	285 ± 7	282 ± 13	286 ± 11	284 ± 9	285 ± 9	286 ± 12	285 ± 10	285 ± 10
3	389 ± 3	388 ± 9	382 ± 10	393 ± 9	391 ± 11	389 ± 10	393 ± 11	392 ± 10	391 ± 13
4 (FF=50% + Gd)	441 ± 12	458 ± 16	469 ± 16	593 ± 53	441 ± 19	488 ± 23	629 ± 61	455 ± 23	494 ± 24
5 (FF=50%)	758 ± 7	442 ± 27	804 ± 33	275 ± 28	484 ± 37	648 ± 53	372 ± 31	609 ± 36	883 ± 53
6	786 ± 4	816 ± 19	797 ± 13	818 ± 20	812 ± 18	814 ± 19	817 ± 16	815 ± 18	813 ± 15
7 (FF=25%)	1207 ± 14	839 ± 47	1589 ± 34	770 ± 84	982 ± 50	1299 ± 77	909 ± 73	1302 ± 60	1768 ± 113
8 (Large compt.)	1268 ± 11	1268 ± 46	1294 ± 19	1303 ± 53	1300 ± 47	1284 ± 43	1315 ± 37	1312 ± 34	1306 ± 39

Global T_1 values inside vials with fat showed considerable variations across MP2RAGE protocols. Global T_1 values inside vial #7 (i.e., FF = 25%) varied considerably between MP2RAGE protocols. For instance, LS2 overestimated the global T_1 values whereas SS2 underestimated the global T_1 values when compared with IR-SE. For SM2A and SM2B, the global T_1 values considerably increased with echo time. Both protocols showed the same behavior with the exception that global T_1 values calculated from SM2B were longer than SM2A for each respective echo. A similar increasing pattern across echo time was observed for vial #5 (i.e., FF = 50%) for SM2A and SM2B. For LS2, the global T_1 values were similar to the reference whereas for SS2 the global T_1 values were underestimated. The global T_1 values inside vial #4 (i.e., FF = 50% + Gd) were similar to the reference for LS2 and SS2. For SM2A and

SM2B, the 1st echo overestimated the global T_1 values in comparison with the reference. Nevertheless, for the 2nd and 3rd echoes, the global T_1 values were comparable with the reference and among the two echoes. The increase pattern of global T_1 values with increasing TE observed for the two other vials with fat was not observed for vial #4. These observations about the mean global T_1 values and their 95% CIs can be further observed by looking at the bar plots shown with Figure 4.17.

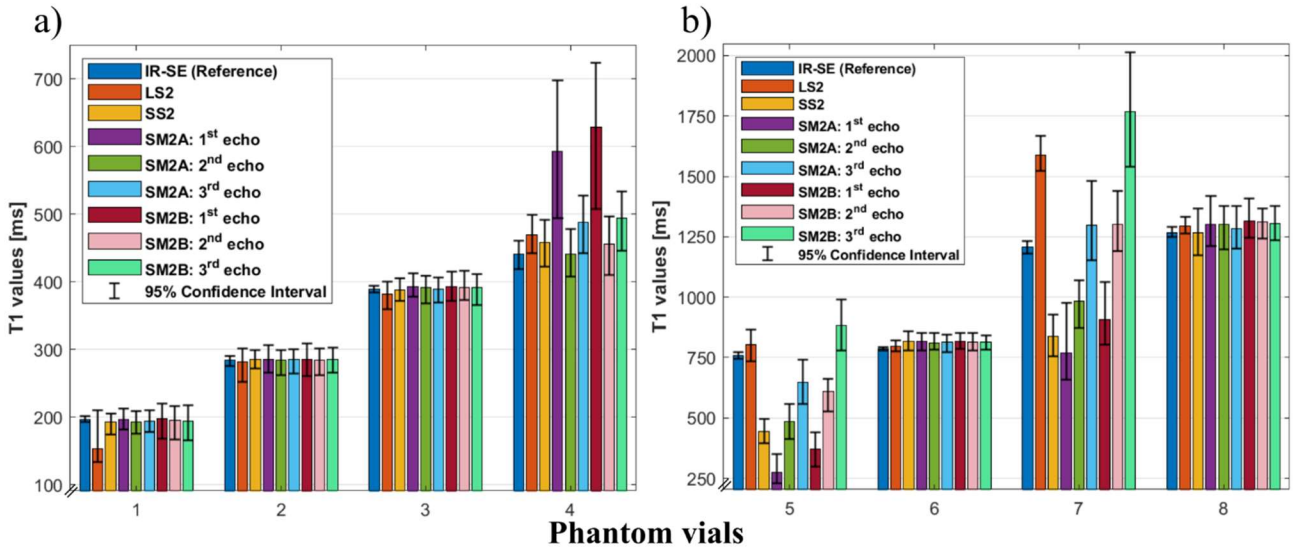

Figure 4.17 *- Bar plots of the mean global T_1 values and corresponding 95% CIs for all vials and protocols acquired during experiment #2. Global T_1 axis are cut for better visualization.*

Figure 4.17 shows that all mean global T_1 values calculated from MP2RAGE protocols overlapped with the reference for vials #1, 2, 3, 6 and 8. These five vials are in fact the vials without fat content and the large compartment as mentioned above. For vial #4, only the 1st echo of SM2A and SM2B did not overlap with IR-SE. For vial #4, LS2 and SS2 showed comparable mean global T_1 values. However, LS2 and SS2 showed considerable variations for the two other vials with fat (#5 & 7) where LS2 overestimated and SS2 underestimated the mean global T_1 values calculated in comparison with IR-SE. LS2 was the unique MP2RAGE protocol that the mean global T_1 value overlaps with IR-SE for vial #5. For vial #7, SM2A: 3rd echo and SM2B: 2nd echo were the only protocols to overlap with the reference. For experiment #2, no MP2RAGE protocol overlapped with the reference through all vials for global T_1 maps.

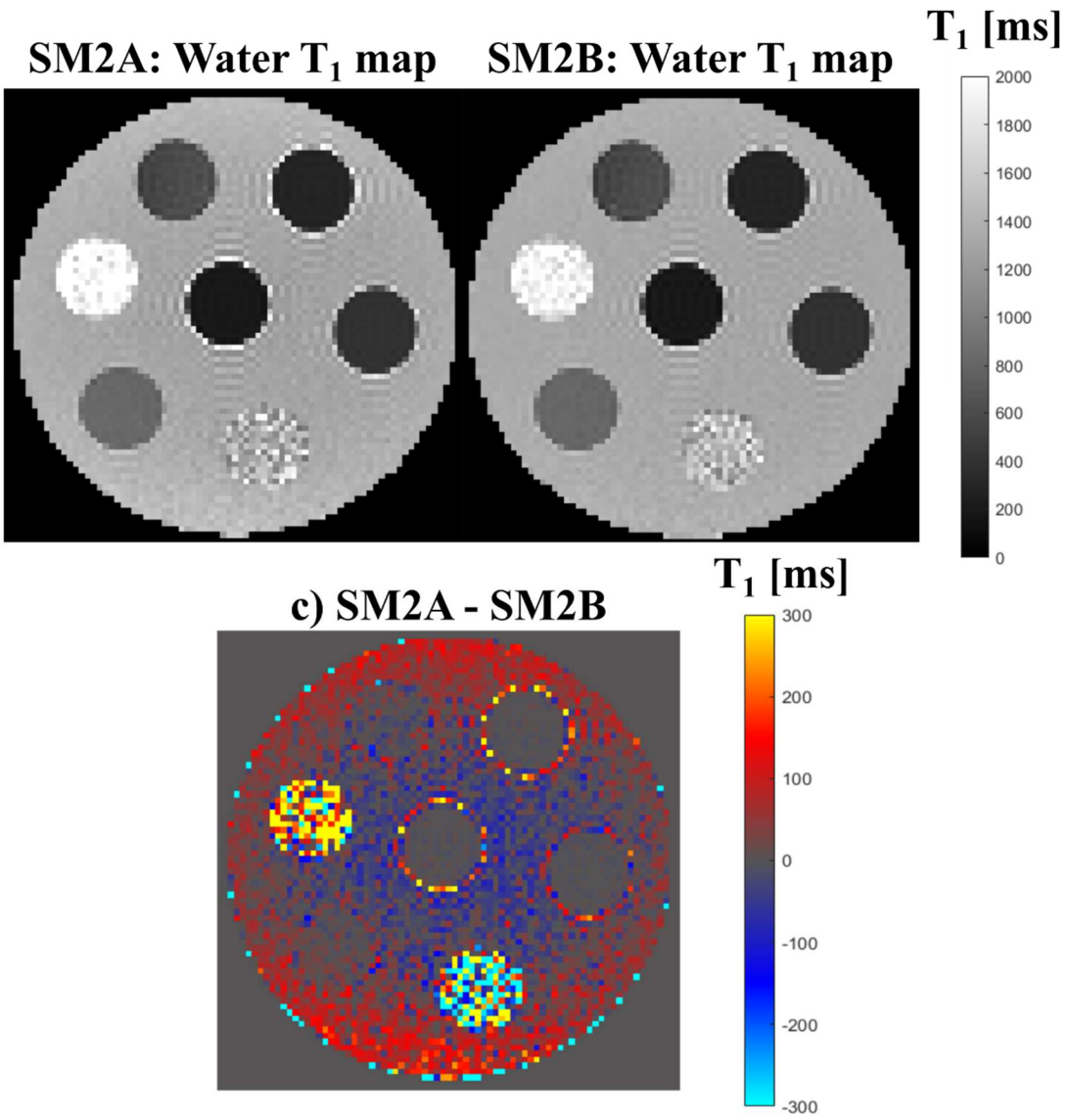

Figure 4.18 *- Water-only T_1 maps from both ME-MP2RAGE protocols acquired during experiment #2. The difference water T_1 map between SM2A and SM2B is shown in (c) with a bipolar colormap. The main differences are observed in vials #5 and #7. Shading in the large compartment is likely due to differences in sensitivity to transmit B_1^+ inhomogeneity between the protocols. The T_1 maps shown correspond to the same slice location as the global T_1 maps shown on Figure 4.16.*

Even if LS2 overlapped with the reference for vial #1, #2 and #3, LS2 was the least accurate protocol for these vials. As seen from Table 4.4, there was a difference of 43 ms between the mean global T_1 values calculated from the reference and LS2 for vial #1. In comparison, the

maximum difference among other MP2RAGE protocols was 4 ms (for SS2) for vial #1. Moreover, LS2 was the least precise protocol for vials #1 and #2. On the other hand, LS2 was the most precise MP2RAGE protocol for vial #6, #7 and #8.

The water-only T_1 maps calculated for SM2A and SM2B protocols showed great similarity. The water T_1 maps for SM2A and SM2B are presented on Figure 4.18. Vials #1, 2, 3, 6 and 8 (i.e., vials without fat) were highly similar between both ME-MP2RAGE protocols. One minor visual difference between both protocols was the slightly less intense Gibb's ringing artifacts for SM2B in the large compartment compared to SM2A. For vials with fat (i.e., #4, #5 and #7), both protocols produced similar water T_1 values. For vial #5, poor water T_1 uniformity across the vial was measured for both protocols. Vial #7 had comparable water T_1 values between SM2A and SM2B whereas vial #4 had highly similar water T_1 values for SM2A and SM2B. The mean water T_1 values and corresponding standard deviations calculated inside each vial for SM2A and SM2B are shown in Table 4.5. For vial #5 and #7, a difference of -99 ms and 223 ms were measured between the mean water T_1 values calculated from SM2A and SM2B respectively. In opposition, for the six other vials, the largest difference measured between the two protocols was 20 ms (vial #8). SM2A had slightly smaller standard deviations for the first four vials than SM2B. However, the values were still highly comparable between the two protocols. For the last four vials, SM2B had smaller standard deviations. Standard deviations calculated for vials #5 and 7 for SM2B were considerably smaller than the standard deviations calculated of SM2A. Overall, SM2B was slightly more precise mostly due to the considerable differences observed in vials #5 and #7.

Table 4.5 *- Mean water T_1 values and standard deviations calculated from water-only T_1 maps of SM2A and SM2B in comparison with the reference IR-SE.*

Vial	IR-SE Global T1	SM2A Water T1	SM2B Water T1
1	197 ± 2	196 ± 8	196 ± 13
2	284 ± 5	286 ± 9	286 ± 11
3	389 ± 3	391 ± 8	392 ± 11
4 (FF=50% + Gd)	441 ± 12	592 ± 31	597 ± 33
5 (FF =50%)	758 ± 7	1403 ± 311	1502 ± 236
6	786 ± 4	820 ± 16	808 ± 14
7 (FF=25%)	1207 ± 14	2200 ± 416	1977 ± 182
8 (Large compt.)	1268 ± 11	1287 ± 38	1307 ± 29

The fat T_1 maps produced from fat-only MP2RAGE images for SM2A and SM2B were highly similar. The two fat T_1 maps are shown in Figure 4.19. The fat T_1 values inside the three vials were highly uniform among the two protocols. Two (or three) voxels that produced fat T_1 values considerably greater than the rest were visible in the bottom left corner of vial #4 for protocol SM2B. The mean fat T_1 values and corresponding standard deviations calculated for every vial are shown in Table 4.6. All mean fat T_1 values calculated are in a narrow T_1 range. For instance, the minimum and maximum mean fat T_1 values calculated among FFs and protocols were 260 ms and 296 ms respectively. Standard deviations were also distributed inside a narrow range. The smallest and largest standard deviations were 19 ms for vial #5 and 37 ms for vial #7 both for SM2A respectively.

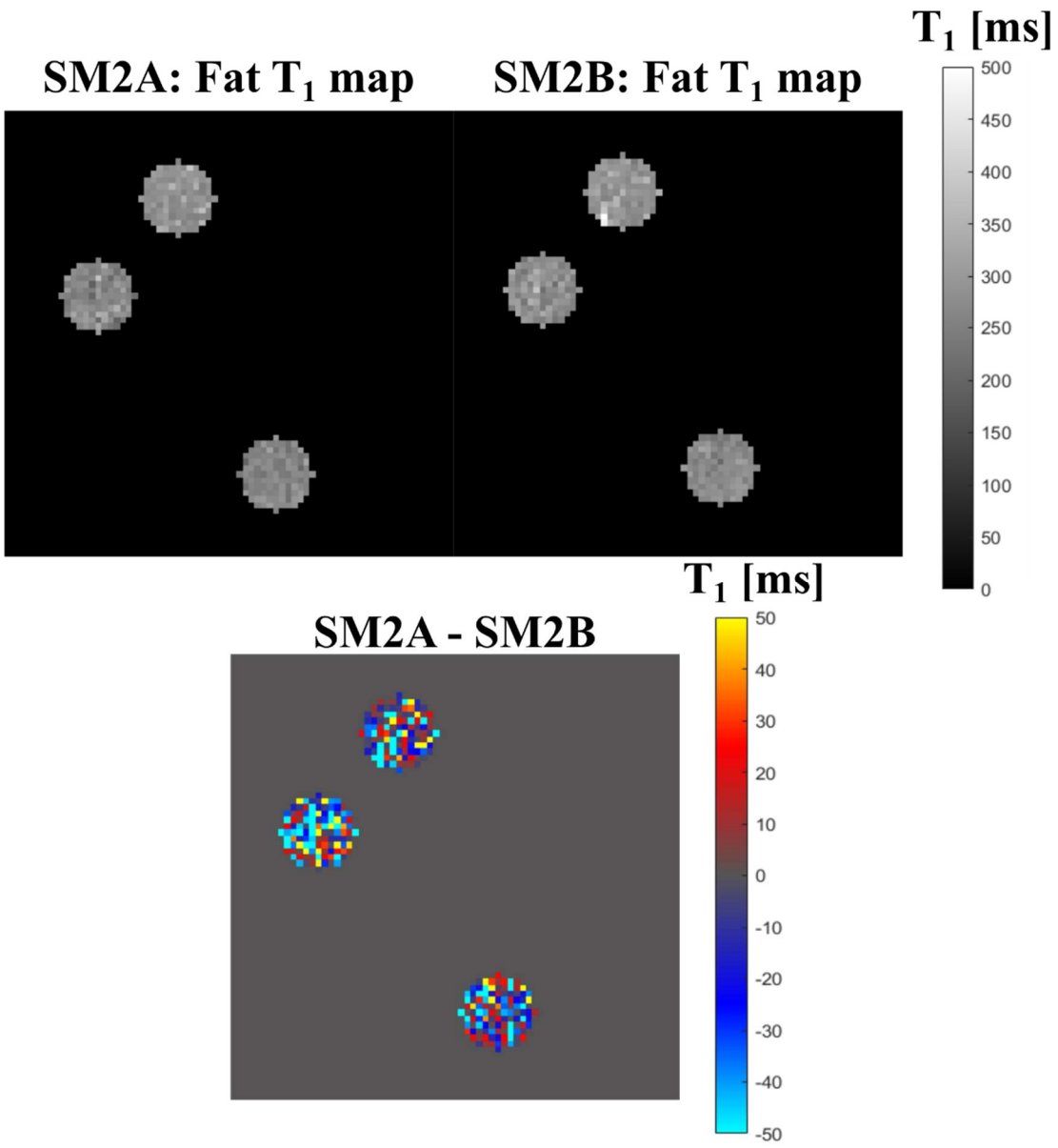

Figure 4.19 *- Fat-only T_1 maps produced from both ME-MP2RAGE protocols acquired during experiment #2. The 2D T_1 maps shown here possess the same slice location as Figure 4.16. The difference fat T_1 map between SM2A and SM2B is shown with a bipolar colormap below the two fat T_1 maps.*

Table 4.6 *- Fat mean T_1 values and their respective standard deviations calculated for SM2A and SM2B for the three vials with fat inside phantom #2.*

Vial	SM2A Fat T_1	SM2B Fat T_1
FF=25%	268 ± 37	286 ± 36
FF=50%	260 ± 19	272 ± 22
FF=50% + Gd	288 ± 25	296 ± 30

The relaxivity values of the GBCA calculated for experiment #2 were highly comparable among all protocols acquired and with the values calculated in experiment #1 with the exception of LS2. The global R_1 values plotted against the concentrations of GBCA are shown on Figure 4.20. For LS2, the largest concentration of GBCA showed a considerably larger global R_1 value than the rest. The relaxivity values calculated from every global T_1 maps are shown in Table 4.7. Except for protocol LS2, which was an outlier, all other protocols gave highly similar relaxivity values. Other protocols gave a minimum relaxivity value of 4.59 ± 0.17 $s^{-1}mM^{-1}$ for IR-SE and a maximum of 4.72 ± 0.08 $s^{-1}mM^{-1}$ for SS2. LS2 expectedly showed the lowest R^2 value at 0.9818 whereas SS2 showed the largest R^2 with 0.9998. Standard deviations calculated were also highly similar among protocols.

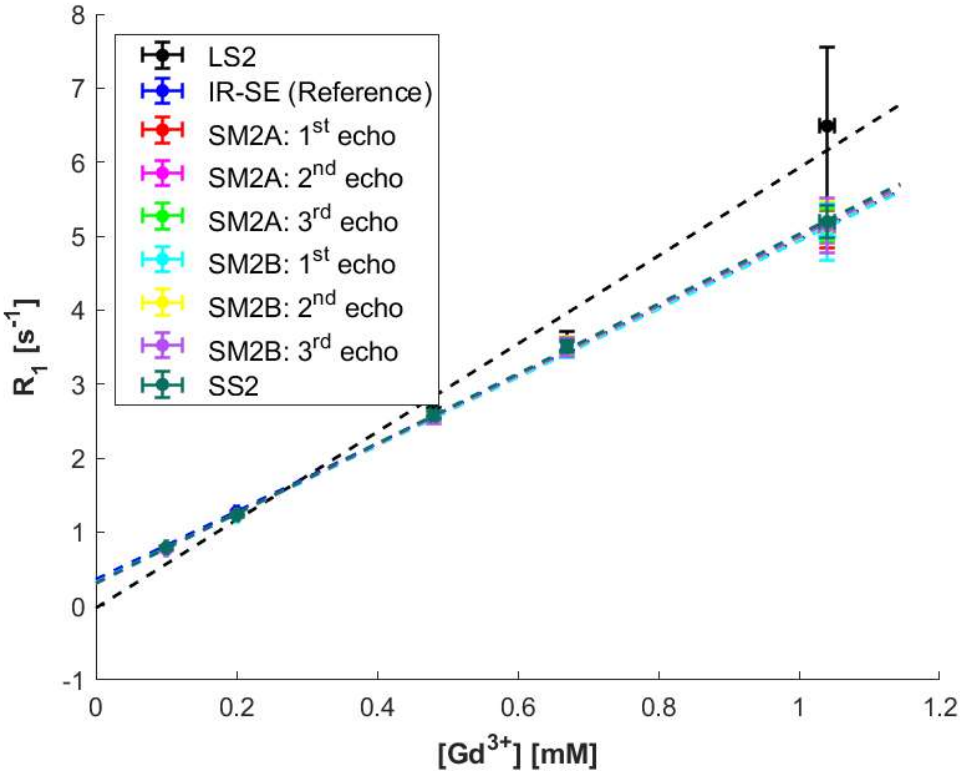

Figure 4.20 *- Global R_1 values against the concentrations of GBCA inside vials for experiment #2. The dashed lines correspond to the result of the linear fit of global R_1 values. Only vials without fat were used for calculations.*

***Table 4.7** - Relaxivity values calculated from linear fit of global R_1 values against concentrations of GBCA solution inside vials of phantom #2. Vials with fat were excluded from these measurements.*

Protocol	Relaxivity ± std. dev. [$s^{-1}mM^{-1}$]	R^2
IR-SE	4.59 ± 0.17	0.9992
LS2	5.95 ± 1.05	0.9818
SS2	4.72 ± 0.08	0.9998
SM2A (1st echo)	4.64 ± 0.15	0.9994
SM2A (2nd echo)	4.71 ± 0.12	0.9996
SM2A (3rd echo)	4.68 ± 0.12	0.9996
SM2B (1st echo)	4.61 ± 0.19	0.9990
SM2B (2nd echo)	4.67 ± 0.15	0.9994
SM2B (3rd echo)	4.68 ± 0.13	0.9996

4.5 Quantitative assessment of fat-water separated T_1 mapping from ME-MP2RAGE protocols across a wide range of T_1 values.

The global T_1 maps produced from ME-MP2RAGE protocols acquired during experiment #3 varied considerably across echoes and protocols as shown on Figure 4.21. The global T_1 maps shown are in reflection from left to right from the diagram of the phantom as shown on Figure 3.3 which means that column #1 is the FF = 50% column whereas column #5 corresponds to the FF = 0%. The concentrations of GBCA are unchanged as the positioning shown on Figure 3.3 (i.e., increasing from row D to A). Air bubbles were present inside some vials. Specifically, in column #2, vials A, B and D contained air bubbles at the top of the vial. The other vial with an air bubble is vial 4-D. SM3A and SM3B showed a similar behavior where global T_1 maps

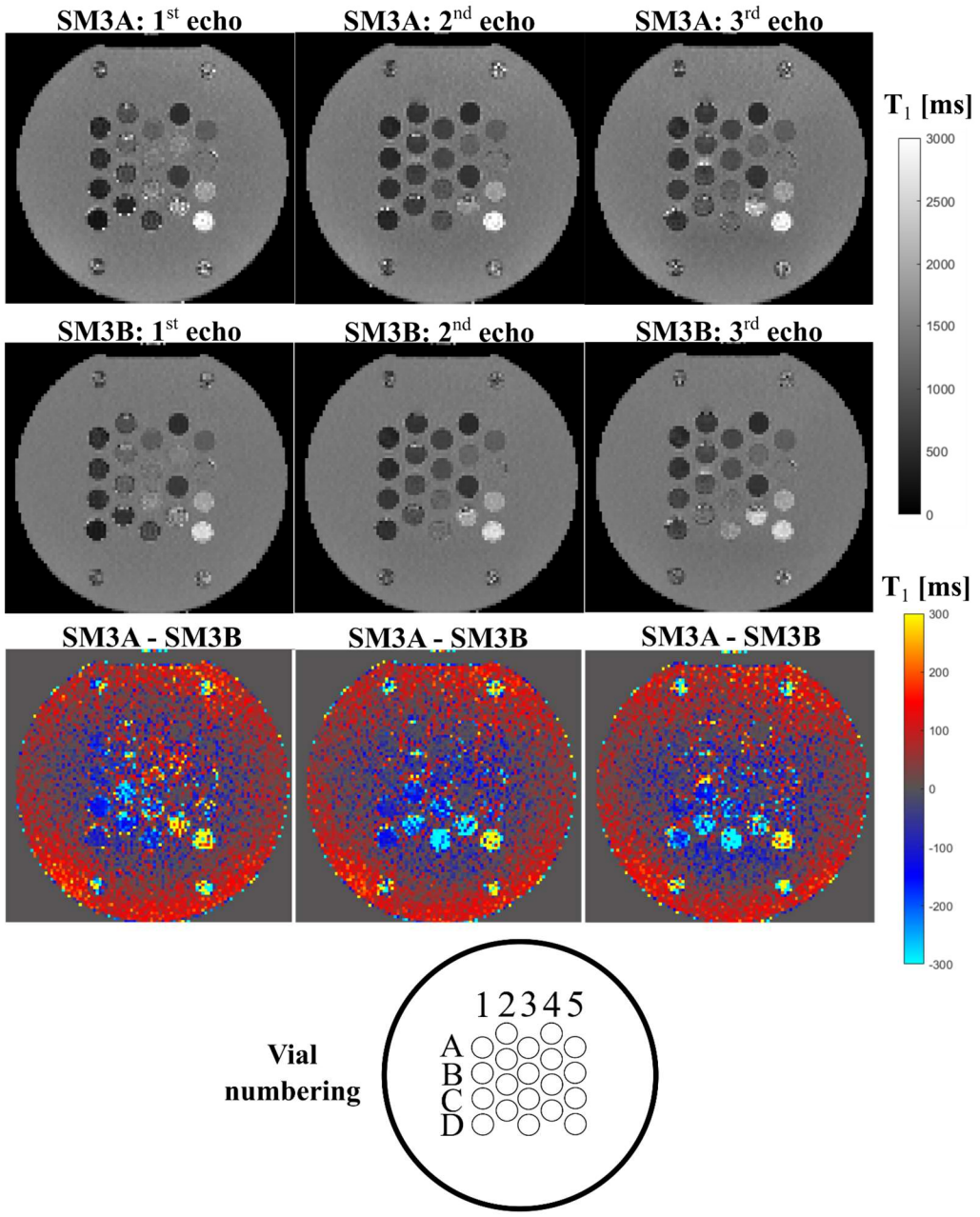

Figure 4.21 *- Global T_1 maps calculated from both ME-MP2RAGE protocols acquired during experiment #3. All 2D T_1 maps shown corresponds to the same slice location. The global T_1 maps shown are a reflection from left to right from the diagram of the phantom shown on Figure 3.3. Thus, the FF = 50% is the column on the left and FF = 0% the one on the right. The difference global T_1 maps between SM3A and SM3B are shown under each echo respectively with a bipolar colormap. The main T_1 differences are observed in row D. The differences observed in the large compartment are likely due to differences in sensitivity to transmit B_1^+ inhomogeneity between both protocols. A small diagram is shown below the difference T_1 maps to simplify vial identification.*

calculated from the 1st echo showed higher T_1 variability than the other echoes. Column #5

produced the most uniform global T_1 values across echoes for both protocols. However, for the four other columns, the global T_1 maps produced from the 1st echo had more noise compared to the two other echoes. The level of noise in the global T_1 maps from the two last echoes were comparable.

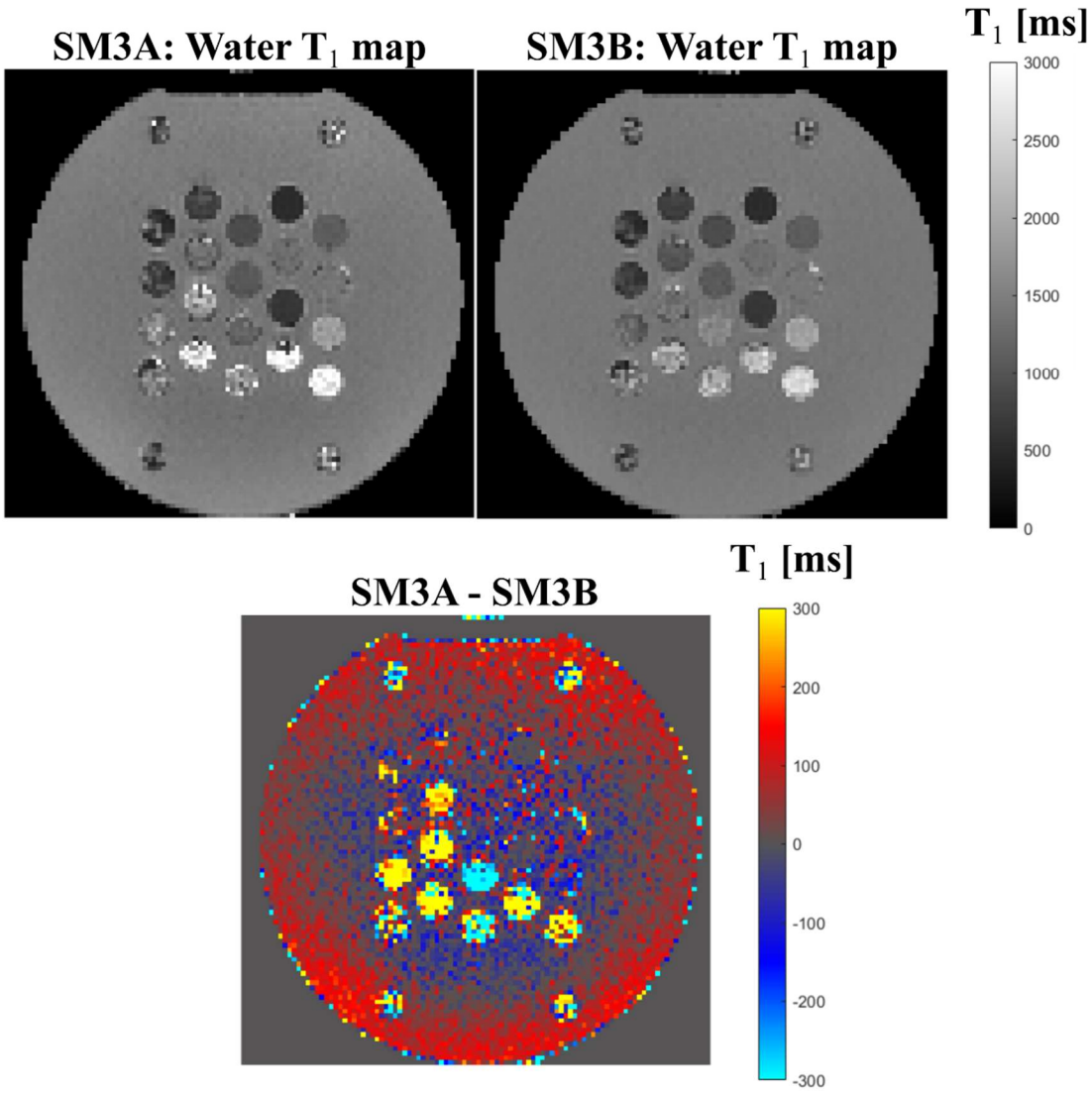

Figure 4.22 *- Water-only T_1 maps calculated from both ME-MP2RAGE protocols acquired for experiment #3. The difference water T_1 map between SM3A and SM3B is shown under the two respective water T_1 maps with a bipolar colormap. The main differences are observed in columns 1 and 2 in addition to rows C and D. The differences observed in the large compartment are likely due to differences in sensitivity to transmit B_1^+ inhomogeneity between the protocols. These 2D T_1 maps have the same slice location as the global T_1 maps shown in Figure 4.21.*

The water-only T_1 maps showed variability between both ME-MP2RAGE protocols acquired. The water-only T_1 maps are shown in Figure 4.22. Overall, the water T_1 map from SM3A had lower T_1 homogeneity compared to SM3B. That was more noticeable for columns #1, #2 and #3. These differences in T_1 uniformity can also be observed with the mean water T_1 values and standard deviations calculated inside each vial shown with .

For a constant FF, mean water T_1 values calculated from SM3A decreased with increasing [GBCA] except for FFs of 12.5% and 50%. Columns with FFs of 37.5% and 50% showed the lowest precision levels. However, the least precise mean water T_1 value was the vial with a [GBCA] of 0 mM and a fat fraction of 12.5%. Water T_1 values calculated for a fat fraction of 25% showed the highest precision level for SM3A. For a constant [GBCA], the mean water T_1 values calculated did not follow a general trend across FFs. The least precise row of mean T_1 values was the row with [GBCA] = 0 mM. The precision level seemed to increase with larger [GBCA] but still suffered from poor precision levels at the two largest FFs.

For a constant FF, the mean water T_1 values calculated by SM3B decreased with increasing [GBCA] apart from FF = 12.5%. FF = 50% was the column with the lowest precision level among all FFs whereas FF = 0% had the highest precision level. For a constant [GBCA], 0 mM and 0.104 mM showed a clear decrease in the mean water T_1 values with increasing FF. For 0.05 mM and 0.156 mM, the mean water T_1 also decreased throughout FFs except for FF =12.5% that gave mean water T_1 values considerably shorter than expected. The mean water T_1 values for FF=12.5% and [GBCA] of 0.50 and 0.156 mM were also highly precise. These two mean water T_1 values and standard deviations were quite different from the mean water T_1 values with similar FF or [GBCA]. [GBCA] = 0 mM showed the lowest precision level overall.

Overall, SM3B produced a water T_1 map with a higher precision level than SM3A. Specifically, the mean water T_1 values calculated for 16 of the 20 vials were more precise for SM3B than SM3A. The standard deviations calculated in the four vials where SM3A was more precise than SM3B were still highly comparable to SM3B.

Table 4.8 *- Mean water T_1 values calculated for every vial inside phantom #3 with their corresponding standard deviations.*

SM3A Water T_1					
FF [%] / [GBCA] [mM]	**0**	**12.5**	**25**	**37.5**	**50**
0	3030 ± 361	2836 ± 784	1693 ± 332	2694 ± 530	1590 ± 315
0.050	1856 ± 90	640 ± 17	1207 ± 98	1850 ± 434	1747 ± 304
0.104	1373 ± 50	1289 ± 58	1051 ± 31	1292 ± 164	804 ± 212
0.156	1092 ± 34	518 ± 18	895 ± 19	819 ± 108	851 ± 396
SM3B Water T_1					
0	2551 ± 103	2234 ± 197	1999 ± 313	1879 ± 255	1533 ± 380
0.050	1897 ± 63	645 ± 15	1580 ± 97	1340 ± 122	1274 ± 132
0.104	1400 ± 36	1296 ± 52	1059 ± 44	992 ± 75	730 ± 111
0.156	1103 ± 28	522 ± 26	904 ± 21	755 ± 53	709 ± 215

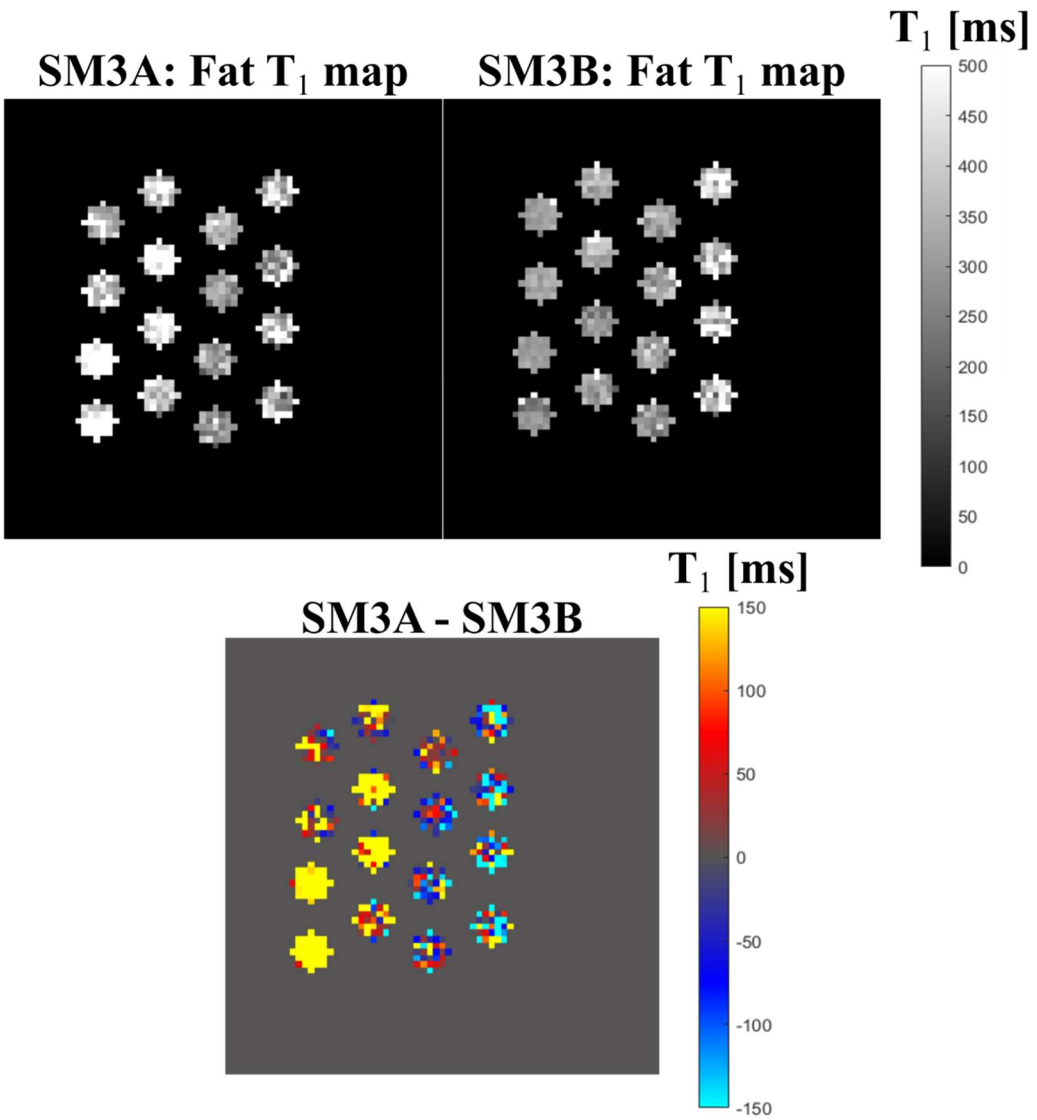

Figure 4.23 *- Fat-only T_1 maps calculated from SM3A and SM3B acquired for experiment #3. The 2D T_1 maps possess the same slice location as Figure 4.21. The difference fat T_1 map between SM3A and SM3B is shown below the two respective fat T_1 maps with a bipolar colormap. Only four columns are visible. The FF=0% column and large compartment are not present since they did not contain fat.*

The fat T_1 map produced from SM3B showed greater T_1 uniformity visually than SM3A overall. The two fat T_1 maps are presented on Figure 4.23. The large compartment and the column #5 visible on the global and water-only T_1 maps were manually masked for better visualization because they did not contain fat. A common characteristic between the two protocols was the

high variability of fat T_1 seen in column #4 (i.e., FF=12.5%) compared to the other columns. For the three other columns, SM3B produced more homogeneous fat T_1 values than SM3A. SM3A gave larger fat T_1 values for columns #1 and #2 in comparison with SM3B. The mean fat T_1 values and standard deviations calculated inside every vial with fat are shown in Table 4.9.

Table 4.9 *- Fat-only mean T_1 values calculated inside all vials with their corresponding standard deviations for SM3A and SM3B acquired at experiment #3.*

SM3A Fat T_1					
FF [%] / **[GBCA] [mM]**	**0**	**12.5**	**25**	**37.5**	**50**
0	-	364 ± 144	306 ± 78	390 ± 56	566 ± 50
0.050	-	424 ± 108	319 ± 61	498 ± 92	546 ± 43
0.104	-	312 ± 113	318 ± 46	555 ± 94	432 ± 123
0.156	-	420 ± 106	373 ± 61	455 ± 143	434 ± 126
SM3B Fat T_1					
0	-	408 ± 128	299 ± 62	322 ± 74	295 ± 27
0.050	-	414 ± 142	331 ± 67	288 ± 44	304 ± 15
0.104	-	428 ± 140	315 ± 46	344 ± 43	318 ± 29
0.156	-	453 ± 101	327 ± 51	343 ± 45	317 ± 15

Overall, SM3B had a higher precision than SM3A for fat T_1 maps. For 11 vials out of the 16 with fat, SM3B was more precise than SM3A. The five other vials had a comparable or equal precision level with SM3A. For both protocols, column #4 was the least precise. The mean fat T_1

values calculated for FF = 25% were the most similar fat T_1 values for a constant FF and among protocols.

SM3A produced larger mean fat T_1 values for FF = 37.5% and 50% than SM3B. The fat T_1 values calculated for FF = 25% were the most precise FF for SM3A. No general trend in the mean fat T_1 values across FFs for a constant [GBCA] was observed. Similarly, no trend was observed for mean fat T_1 values across [GBCA] for a constant FF. However, variations in fat T_1 values across fat fractions were larger than across [GBCA]. The different [GBCA] did not affect the precision level of SM3A. The minimum and maximum mean fat T_1 values calculated for SM3A were 306 ± 78 ms ([GBCA] = 0 mM & FF =25%) and 566 ± 50 ms ([GBCA] = 0 mM & FF = 50%) respectively. A T_1 gap of 260 ms between the maximum and minimum mean fat T_1 values was measured.

No general trend was observed across fat fractions or [GBCA] for the mean fat T_1 values measured by SM3B but variations in mean fat T_1 values were noticeable across fat fractions in opposition with [GBCA]. A considerable difference in mean fat T_1 values calculated from FFs of 12.5% and 50% was observed but the low precision level of FF = 12.5% made it complicated to draw conclusions about this considerable difference. Indeed, FF = 12.5% produced larger mean fat T_1 values in comparison with the other FFs (and not only FF = 50%). The greater fat T_1 uniformity for SM3B seen on Figure 4.23 was also observed with the mean fat T_1 values reported in Table 4.9. Mean fat T_1 values across [GBCA] and a constant FF were constrained in a narrower T_1 range than SM3A. FF = 50% was the most precise FF for SM3B whereas FF = 12.5% was the least precise FF. The different [GBCA] did not affect the precision level for SM3B neither. For SM3B, the gap between the minimum and maximum mean fat T_1 value was 165 ms. The T_1 gap for SM3B was 95 ms smaller than SM3A. The minimum mean fat T_1 value was 288 ± 44 ms ([GBCA] = 0.05 mM & FF = 37.5%) whereas the maximum was 453 ± 101 ms ([GBCA] = 0.156 mM & FF = 12.5%).

For SM3A and SM3B, the relaxivity values calculated from water R_1 values were considerably smaller than the relaxivity measured in experiment #1 and #2 from global R_1 values. The water R_1 values against [GBCA] for the four FFs and both protocols are shown on Figure 4.24. Water

R_1 values for FF = 12.5% were used to calculate the relaxivity but not shown because the poor quality of results was considerably stretching the R_1 axis and reduced visibility. SM3B produced water R_1 values inside a narrower water R_1 range than SM3A. FF = 50% had the largest error bars among all FFs for both protocols. The water relaxivity and R^2 values calculated from the linear fit for all FFs and protocols are shown in Table 4.10.

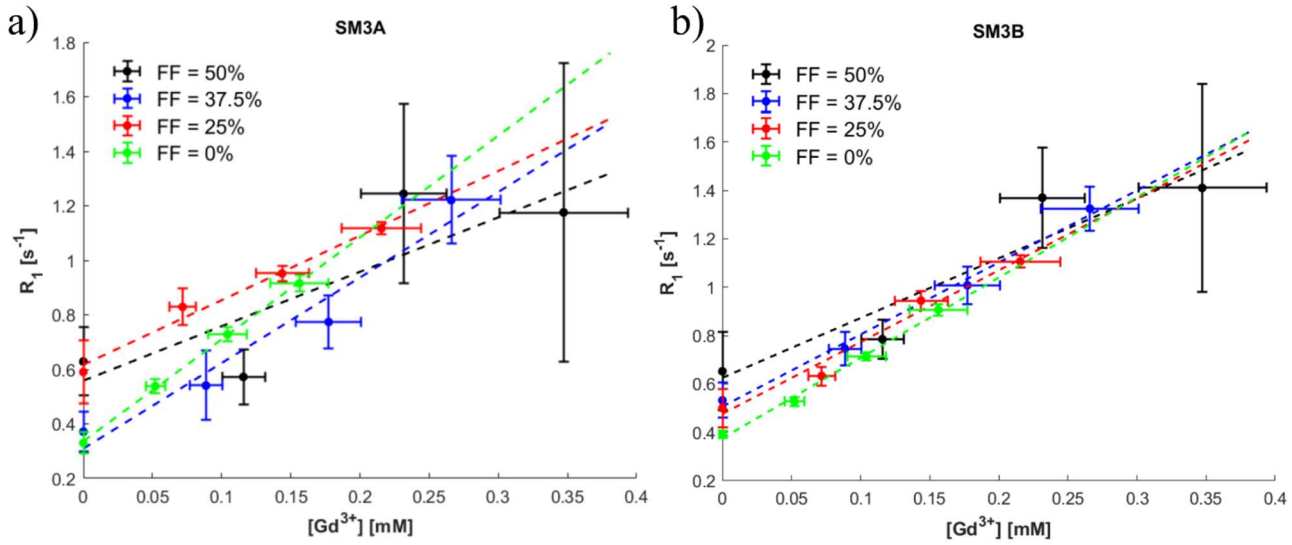

Figure 4.24 *- Water R_1 values against the concentrations of GBCA corrected for the water volume inside vials for different FFs of SM3A and SM3B. The dashed lines correspond to the results of the linear fits of the water R_1 values. FF = 12.5% is not shown due to poor quality of the results.*

Even if not shown on Figure 4.24, GBCA relaxivity values in water for FF = 12.5% were calculated for both protocols. These relaxivities were considerably larger than the values calculated for other FFs while also having excessively large standard deviations. Both linear fits of water R_1 values for FF = 12.5% showed poor linearity as evident from their R^2 values of 0.5011 and 0.4753 for SM3A and SM3B respectively. FF = 50% showed the second lowest R^2 values for both protocols with values smaller than 0.90. The three other FFs had R^2 values larger or equal than 0.95. Apart from FF = 12.5%, SM3A produced a maximum water relaxivity value of 3.74 ± 0.15 $s^{-1}mM^{-1}$ and a minimum of 2.00 ± 2.01 $s^{-1}mM^{-1}$. For SM3B, the minimum water relaxivity value was 2.47 ± 1.39 $s^{-1}mM^{-1}$ and 3.32 ± 0.41 $s^{-1}mM^{-1}$ for the maximum. For both protocols, the minimum and maximum water relaxivity values calculated occur at the same FFs which were 50% and 0% respectively. SM3A and SM3B had the smallest standard deviations

calculated at FF = 0% which also corresponded to the FF with the largest R^2 values measured for the two protocols.

Table 4.10 *- Relaxivity values measured in water and their corresponding R^2 calculated from their respective linear fits as shown on Figure 4.24.*

FF [%]	SM3A		SM3B	
	Relaxivity ± std. dev [$s^{-1}mM^{-1}$]	**R^2**	**Relaxivity ± std. dev [$s^{-1}mM^{-1}$]**	**R^2**
0	3.74 ± 0.15	0.9993	3.32 ± 0.41	0.9939
12.5	6.54 ± 9.23	0.5011	6.00 ± 8.92	0.4753
25	2.37 ± 0.5	0.9826	2.97 ± 0.74	0.9759
37.5	3.14 ± 1.14	0.9500	2.98 ± 0.41	0.9924
50	2.00 ± 2.01	0.7127	2.47 ± 1.39	0.8877

Chapter 5

Discussion

5.1 Qualitative assessment of MP2RAGE protocol for short T_1 mapping

The clipping of the MP2RAGE lookup table did not considerably affect either version of the short T_1 protocol. The clipping had a limited impact on short T_1 protocols because both short T_1 protocols were designed to have as little overlap as possible (design condition #1: as monotonic as possible). Ultimately, the minor difference in the largest T_1 value reached by both short T_1 protocols should not affect the resulting T_1 values since T_1 values longer than 4500 ms are not frequently observed. However, for the brain T_1 MP2RAGE protocol, the clipping process had a considerable impact on the resulting curve which resulted in reducing the max T_1 value of the lookup table from 5000 ms to approximately 2800 ms. While enabling the clipping option removed ambiguities from overlap of signal values, it significantly reduced the accessible T_1 range for T_1 mapping. For the brain T_1 protocol, all T_1 values longer than 2800 ms were "folded back" into shorter T_1 values, and it can be particularly important since T_1 values measured in cerebrospinal fluid (CSF) are frequently longer than 3000 ms [42]. Ultimately, disabling the clipping option is not a suitable alternative for most of the MP2RAGE lookup tables because considerable underestimation of the long T_1 values calculated will happen if disabled. To the best of our knowledge, clipping is always used [8], [40], [43]–[45] for MP2RAGE T_1 mapping. There is currently no solution to remove the ambiguities between two T_1 values and this project was the first where an option without clipping was studied.

Ultimately, to design MP2RAGE protocols for new T_1 ranges of interest, it would be recommended to disable the clipping option while designing the protocol to see to which extent overlapping is present and evaluate its impact. For instance, if the new lookup table produces overlapping between a T_1 value of 1000 ms and 4000 ms, it would be highly unlikely that the

"legitimate" T_1 value would be 4000 ms (T_1 value clipped) and not 1000 ms (T_1 value not clipped). Thus, overlapping would not be a major issue regarding accuracy of the new MP2RAGE protocol. On the other hand, if the new MP2RAGE protocol creates overlapping between a T_1 value of 1000 ms (T_1 value not clipped) and 2000 ms (T_1 value clipped), both T_1 values might be legitimate. Thus, this new MP2RAGE protocol would suffer from poor accuracy and precision. In the end, once the design process and assessment of overlapping completed, the clipping option should be re-enabled for the application of the MP2RAGE protocol for T_1 mapping.

The qualitative assessment of individual acquisition parameters provided great intuition towards which parameters affected the resulting MP2RAGE-T_1 lookup table more severely. Specifically, the TIs (especially TI_1), FAs, and FA_1 were the acquisition parameters that affected the lookup table the most. Regarding the TI values, it would be reasonable to argue that TI_1 drives most of the variations whereas TI_2 had a minor impact for a fixed $TR_{MP2RAGE}$. In fact, TI_1 is a critical parameter to carefully position the MP2RAGE-T_1 lookup table inside the desired T_1 range of interest. Varying TI_2 seems to mainly affect longer T_1 values than the short T_1 values inside the range of interest for this work. Variations in TI values were limited by the number of excitations (or slices) and TR used for the sequence. Shorter TR values with fewer excitations would enable shorter TI_1 values. Less excitations would be possible by applying partial Fourier on the slice dimension. If partial Fourier is applied on the first excitations (e.g., the first quarter of excitations is not acquired with PF = 6/8), even shorter TI_1 values can be reached. However, applying PF on the slice dimension would not result in a decrease of scan time since slices are acquired inside the RAGE blocks (i.e., in the inner loop) and not once every $TR_{MP2RAGE}$ (outer loop).

Reducing the value of $TR_{MP2RAGE}$ is a way to reduce overlapping for the resulting MP2RAGE lookup table while not affecting the shortest T_1 values considerably. The minimum value for this parameter is limited by TI_2 while there is no limitation for the maximum value except reasonable scan time. Varying both FAs seemed to produce a similar impact on the MP2RAGE-T_1 lookup table as varying both TIs. Varying FA_1 and FA_2 individually was possible. However, since applying fat-water separation with 3-point Dixon was one of the next steps to this work, different FAs for each RAGE block was not considered to keep the same T_1 weighting on both RAGE

images. Moreover, FA values $\leqslant 5^{o}$ were used to reduce the T_{1w} of each RAGE block for fat-water separation [46]. However, it is important to mention that the main factor affecting T_1 weighting of RAGE images is the difference between their TI values. The difference in T_1 weighting between RAGE images cannot be avoided and limits the ability of the MP2RAGE sequence to do accurate measurement of fat and water fractions.

Regarding the inversion efficiency of the inversion pulses, it was interesting to assess the impact of assuming the wrong inversion efficiency of the pulses used with the qualitative assessment. The invEff was assumed to be 0.96 as in [8] because a similar experimental setup was used. Specifically, the standard hyperbolic secant adiabatic inversion pulse from Siemens was used in this work. Frequency offset corrected inversion (FOCI) pulses [47] could result in better inversion of the magnetization but were not implemented in this work. Advantages of using FOCI pulses would be definitely more important at 7 T than 3 T since B_1^+ inhomogeneities are stronger at 7 T [8]. Moreover, as presented in Section 2.2.3, a modified version of the MP2RAGE sequence called MP3RAGE could be implemented to calculate the inversion efficiency for every voxel. However, the first implementation of the MP3RAGE sequence at 3T showed a decrease in precision for the T_1 maps calculated in addition of showing excessively uniform inversion efficiency across the volume of interest [30]. Moreover, Bloch simulations were not used to measure the actual inversion efficiency of the inversion pulses used in this work—a value was taken from prior literature instead. Even if a considerably similar experimental setup as the one seen in [8] was used, discrepancies between scanners and transmit coils can have an impact of the inversion efficiency across the imaging volume. For instance, the transmit coil used in this project was the Siemens body coil whereas a head transmit-receive 8-channel head coil was used in [8]. In the end, knowing that the impact of using erroneous inversion efficiency values inside the short T_1 range of interest was fairly negligeable (See Figure 4.4 d)), that experiments were done at 3 T, and that a similar experimental setup as [8] was used, it would be reasonable to assume that the T_1 maps produced in this project were not considerably affected by the imprecision of the inversion efficiency.

Ultimately, the qualitative assessment of the acquisition parameters provided knowledge of the flexibility of the MP2RAGE sequence regarding optimization for different T_1 ranges of interest.

By modifying acquisition parameters like the TIs, FAs and $TR_{MP2RAGE}$, it is possible to adapt the MP2RAGE sequence to practically any T_1 range of interest desired whether it is short T_1 values as in this work, brain T_1 values as originally designed, or even longer T_1 values over 2000 ms. This ability of the MP2RAGE protocol makes it an interesting protocol for any T_1 mapping application. Moreover, the flexibility of the MP2RAGE protocol does not come with increased complexity or additional steps.

The combinations of acquisition parameters tested during this project were chosen based on the known experimental limitations of the pulse sequence as implemented. For instance, centric encoding was not used for numerical simulations because it was not available with this implementation of the MP2RAGE sequence. Centric encoding would allow shorter TI_1 values because the first acquired readout corresponds to the center of k-space whereas, for linear encoding, the shortest possible TI_1 corresponds to the number of excitations divided by two and multiplied by TR. Thus, it is extremely likely that different combinations of parameters than those used in this work exist and could be used for MP2RAGE protocols optimized for short T_1 values as well. Moreover, MP2RAGE is sensitive to motion due to the use of the linear encoding scheme [48]. For instance, MP2RAGE would be particularly sensible to motion in anatomical regions like the chest or abdomen.

Since RAGE blocks are acquired during the T_1 relaxation of the volume of interest and that TI values correspond to the moment the center of k-space is crossed, T_1 PSF widening is inevitable [8], [29]. Some techniques have been proposed in the literature to correct for widening of T1 PSF such as applying a k-space filter on the acquired data [49]. No correction technique based on k-space filtering was used in this work.

Importantly, the MP2RAGE sequence (and ME-MP2RAGE) is not readily available on the vast majority of clinical MRI platforms. This considerably reduces the availability of the technique proposed in this work to be translated easily into clinical environments. Other similar techniques seen in the literature like MP-GRASP [41] and Dixon cardiac Magnetic Resonance Fingerprinting (Dixon-cMRF) [50] that produce fat and water-specific T_1 maps also suffer from the same clinical availability issue. On the other hand, techniques proposed in the literature using

sequences available on most clinical scanners like Saturation Recovery (SR) [51] or VFA [36] were proposed to perform fat T_1 mapping. However, while being available on most clinical scanners, the SR sequence proposed in [51] requires a special asymmetric turbo spin echo sequence not available on most clinical scanner in addition of suffering from single-slice imaging and long acquisition times. VFA depends on imperfect RF spoiling, requires many signal averages that increases scan time (to increase SNR), is limited to magnitude data for fitting rather than complex data and requires additional scan time to acquire a B_1 map and a fat spectrum [36].

5.2 Quantitative assessment of MP2RAGE protocol optimized for short T1 mapping with numerical simulations

The quantitative assessment of the short T_1 MP2RAGE protocol boiled down to modulating the common nonlinear behavior of MP2RAGE protocols to move the optimization range of accuracy and precision inside the T_1 range of interest of this work. The curves describing variations in accuracy (and precision) had common features between the short and brain T_1 MP2RAGE protocols. Ultimately, the numerical simulations could be seen as a way to investigate how the nonlinear effects of the MP2RAGE-T_1 lookup tables could be modulated to displace the optimized T_1 range towards shorter T_1 values from modifications in the acquisition parameters.

The increase in MP2RAGE "signal resolution" of version B of the short T_1 MP2RAGE protocol in comparison with version A was barely noticeable for T_1 accuracy and precision from numerical simulations. Accuracy inside the T_1 range of interest did not increase at all whereas precision slightly increased, by approximately 1 ms. That was an interesting result since it would have been reasonable to assume that having a broader range of MP2RAGE signal values to describe the same T_1 range would result in a better accuracy and precision, which was ultimately not the case.

Assessing the theoretical B_1^+ sensitivity of the MP2RAGE protocols was interesting since no correction technique was applied to the T_1 maps produced in this project. The main acquisition parameters affecting B_1^+ sensitivity in numerical simulations were the number of excitations (or

number of slices), $TR_{MP2RAGE}$, TIs, and the flip angle values [45]. A modification to the original MP2RAGE sequence to account for B_1^+ inhomogeneities has been proposed in the literature [40]. This modification consists of adding a fast sequence called Sa2RAGE to produce a B_1^+ lookup table. This B_1^+ lookup table can then be used to produce T_1 maps corrected from B_1^+ inhomogeneities. However, the work in [40] was focused on 7 T acquisitions where B_1^+ inhomogeneities are a considerable issue in comparison with 3 T [8]. Moreover, the additional Sa2RAGE acquisition results in increased scan time with an additional registration step with the MP2RAGE images [45]. Thus, adding the Sa2RAGE sequence for B_1^+ correction was not considered for this work. In the end, version B of the short T_1 MP2RAGE had a slightly higher theoretical precision and lower B_1^+ sensitivity than version A, which settled the choice of short T_1 MP2RAGE protocol to use for the first experimental acquisition.

Ultimately, the quantitative assessment confirmed the goal of the qualitative assessment: the MP2RAGE protocol can be optimized for a T_1 range of interest of shorter T_1 values than the original implementation for brain T_1 mapping. Higher accuracy and precision levels can be obtained outside of the original MP2RAGE brain T_1 range of interest solely by modifying the MP2RAGE acquisition parameters. Moreover, the quantitative assessment confirmed that the qualitative assessment performed beforehand gave great insights towards which acquisition parameters would produce the optimization for the desired T_1 range of interest. In other words, the initial qualitative assessment was a great way of finding approximately the suitable acquisition parameters for the desired T_1 of interest. Then, numerical simulations allowed to fine-tune these parameters quantitatively to find the most optimal combination over the desired T_1 range.

5.3 Experimental validation of the short T_1 MP2RAGE protocol.

Overall, the newly designed short T_1 MP2RAGE protocols (SS1 and SM1) produced highly similar R^2 values with the brain T_1 protocol with higher agreement with the IR-SE than the original brain T_1 MP2RAGE protocol (LS1) across the complete range of T_1 values. SS1 protocols had comparable correlation with LS1 while being 33% faster to acquire than LS1 whilst SM1 had better correlation and was 51% faster than LS1. In addition, SS1 produced

global and SM1 global and water T_1 maps with higher accuracy and uniformity than global and water T_1 maps produced with another similar technique seen in the literature [41] called Magnetization-Prepared Golden-angle RAdial Sparse Parallel (MP-GRASP), which used a stack-of-stars trajectory with 3-point Dixon to calculate fat-water separated T_1 maps. Thus, the experimental validation of short T_1 MP2RAGE protocols and feasibility of short T_1 ME-MP2RAGE protocols were demonstrated with experiment #1.

Although all MP2RAGE protocols produced highly similar global T_1 maps, minor discrepancies between global T_1 maps were noticeable. For instance, the three variations of the SS1 protocol had exactly the same acquisition parameters inputted into the MP2RAGE lookup table calculation algorithm except for the number of excitations and TR, and they produced highly similar global T_1 maps for short T_1 values. However, discrepancies started to appear at longer T_1 values. The impact of TR on the MP2RAGE-T_1 lookup table for short T_1 values was negligeable as presented in section 4.1. Thus, variations in accuracy and precision levels could not be explained by TR differences between the three variations of SS1. However, the T_1 variability considerably increased with the number of excitations. The increase in T_1 precision could be due to the use of thicker slices for SS1C compared to SS1A and SS1B. Consequently, SS1C produced highly precise T_1 values even outside the short T_1 range of interest. In fact, SS1C was surprisingly more precise than LS1 inside the T_1 range of brain T_1 values. On the other hand, the thicker slices used did not provide a higher T_1 accuracy level for SS1C compared to SS1A and SS1B.

The voxel size was a factor which was not included in the MP2RAGE lookup table calculation that affected T_1 values. SS1A had the smallest voxel size among all MP2RAGE protocols acquired and also the lowest precision level overall. With SS1B that was nearly identical to SS1A except for the 0.3 ms difference in TR and voxel size (1.13x1.13x1.10 mm^3 VS 1.33x1.33x1.33 mm^3 respectively), there was a noticeable difference in precision between the two protocols due to the voxel size difference. Accuracy was not affected by voxel size. As expected, voxel size was a trade-off between precision and resolution which was not taken in account by the MP2RAGE T_1 mapping model. Depending on the desired application of the MP2RAGE protocol for T_1 mapping, voxel size could be adapted. For instance, if small voxel

sizes are required, a smaller number of slice (or partitions) could be acquired to compensate and vice-and-versa.

Essentially, the voxel sizes used in this project were limited by the readout bandwidth which is directly related to maximum gradient output of the scanner. Higher readout bandwidth values were required for multi echo sequence in comparison with single echo sequences due to the acquisition of three echoes instead of one within a similar TR value. Keeping the same voxel size while changing from a single to multi echo protocol would have resulted in prohibitively high readout bandwidth. Oppositely, decreasing the voxel size of single echo acquisition while keeping the same bandwidth value as a multi echo protocol would have been possible. However, that option was not tested in this project.

The TE values did not considerably affect the global T_1 maps calculated by the three different echoes of SM1, except that a minor decrease in mean global T_1 values was observed with increasing TE. Since the MP2RAGE model accounts for variations in TR only and not TE (i.e., the three echoes were considered as the same protocol for the MP2RAGE lookup table calculation), the global T_1 uniformity across echo times was expected. However, the minor decrease in mean global T_1 values with increasing echo time (except for vial #5) might have come from slight T_2^* relaxation. Considering that $\Delta TE = 3.54$ ms between the 1st and 3rd echo, some T_2^* decay would have occurred and resulted in slight decrease of signal intensity with time for RAGE images. Ultimately, this could have resulted in a decrease of the SNR, producing the slight decrease observed in mean global T_1 values. No examination of the impact of T_2^* relaxation on the global T_1 maps was performed during this project but it could be done in future work. For instance, the same MP2RAGE protocol with different TEs (i.e., while keeping the other acquisition parameters constant) could be acquired to see if global T_1 maps would be affected by the TE. However, at some point, long TEs would require longer TRs which would affect the calculated lookup tables.

The ΔTE used for SM1 ($\Delta TE = 1.77$ ms) was not optimal for fat-water separation with the strength of the magnetic field used experimentally because it was limited by the readout bandwidth and the use of monopolar readouts. Optimal ΔTE for the experimental setup used

would have been 1.16 ms for a B_0 of 2.895 T and assuming a chemical shift of 3.5 ppm between water and fat protons [33]. Bipolar readouts can be used for fat-water separation but additional phase corrections are required to avoid phase inconsistencies between odd and even echoes [52]. For this project, monopolar readouts were used to avoid additional correction steps for phase inconsistencies. Consequently, relatively high bandwidth values were required to obtain adequate ΔTE for 3-point Dixon from monopolar readouts. For example, 1515 Hz/px was used for the SM1 protocol compared to 500 Hz/px for the SS1 protocol. Surprisingly, the lower SNR expected from the higher readout bandwidth [12] did not impact the T_1 accuracy and precision for SM1.

Furthermore, it was discovered after experiment #1 from [8] that LS1 was an MP2RAGE protocol designed for fast scanning and not explicitly for accurate brain T_1 mapping at 3 T. Thus, the combination of acquisition parameters used for LS1 was not the best example of parameters used for a typical brain T_1 MP2RAGE protocol. With shorter TIs and $TR_{MP2RAGE}$ compared to the other brain T_1 MP2RAGE protocols at 3 T shown in [8], LS1 was more or less an intermediate protocol between short T_1 and brain MP2RAGE protocols. Consequently, a new brain T_1 MP2RAGE protocol more representative of a protocol acquired for brain T_1 mapping was selected for experiment #2.

The comparison between the theoretical model and experimental results was not conclusive likely due to the use of a theoretical model that was probably overly simple. For instance, the theoretical model used for numerical simulations did not account for B_1^+ inhomogeneities and variations in inversion efficiency across the imaging volume, which probably impacted experimental accuracy and precision. Moreover, the theoretical model was not able to account for variations in the SNR. Experimentally, SNR and noise levels varied between vials. For instance, the TI values selected for the short T_1 MP2RAGE protocol considerably reduced signal inside vials where T_1 values were close to the null point (TI_{null}). The current theoretical model calculated the average signal in RAGE block #2 to calculate the resulting SNR value to use for simulations. However, in experimental acquisitions, all signal values are most likely not present or equally distributed (i.e., some signal values are more present than other) which affects the mean signal value in the image. In the end, a more sophisticated theoretical model would help in

the prediction of experimental values of accuracy and precision for the MP2RAGE protocols used in numerical simulations.

The proposed MP2RAGE protocols in this work for short T_1 mapping gave T_1 values highly comparable or even better than the MP-GRASP approach [41]. First, the correlation of the MP2RAGE protocols proposed in this work against the same IR-SE reference technique was highly similar or even better than MP-GRASP with R^2 values over 0.999. The short T_1 MP2RAGE protocols also produced more uniform global T_1 values visually throughout the large compartment than the MP-GRASP technique [41]. Furthermore, the stability of the global mean T_1 values calculated from SM1 across echoes was higher. For global T_1 values in the same T_1 range, MP-GRASP showed a difference of 13 ms between the mean global T_1 values calculated from two echoes IP and OP whereas SM1 showed a difference of 2 ms. Ultimately, due to the limited presentation of accuracy results in [41], a comprehensive comparison between the MP2RAGE protocols proposed in this work and the novel MP-GRASP technique was difficult.

Relaxivity values calculated for experiment #1 were highly similar to 4.7 ± 0.2 $s^{-1}mM^{-1}$ [53] and 4.35 ± 0.05 $s^{-1}mM^{-1}$ [38] reported in the literature for the same range of temperature. The relaxivity values measured consolidated the overall quality of the global T_1 maps produced for experiment #1 by acting a quality check of the global T_1 maps.

5.4 Experimental assessment of fat-water separated ME-MP2RAGE protocols

The behavior of global T_1 values for the three vials with fat varied considerably among MP2RAGE protocols. The overestimation and underestimation of global T_1 values compared to the reference for LS2 and SS2 in vials #5 and #7 implied that the MP2RAGE signal values were smaller and larger than expected for LS2 and SS2 respectively. On the other hand, no clear discrepancy between LS2 and SS2 was observed for vial #4. Due to the intricate nature of the MP2RAGE combination of complex signals from the two RAGE images, it can be arduous to find the exact reasons explaining the changes observed in MP2RAGE signal values (and global T_1 values ultimately). First, it is important to point out the known difference between the two

TEs of LS2 and SS2. The TE of LS2 corresponded exactly to the first IP condition of the fat and water protons in their phase cycling whereas it corresponded to halfway between the first IP and OP condition for SS2. Thus, the IP condition normally produces more signal since fat and water signals add up whereas less signal is produced from an in-between IP and OP condition. More signal in both individual RAGE images result in larger MP2RAGE signal values which would result in an increase of the global T_1 values. However, the opposite was observed for LS2 which is quite baffling. In the end, variations in global T_1 values calculated with different TE values inside vials with fat and water were expected, but it was not possible to find a clear explanation of the variations observed experimentally.

For SM2A and SM2B, the considerable variations in global T_1 values among echoes were also expected. The TEs were purposely selected to put the fat and water protons into different IP-OP conditions to modify the global signal measured. However, it was not expected that the variations of global T_1 versus TE would be different among vials. Indeed, vial #4 (FF=50% + GBCA) showed a different pattern of variation across echoes compared to vials #5 (FF=50%) and #7 (FF=25%). The only known difference between vial #4 and the two other was the presence of GBCA. The considerable variations for global T_1 values through echoes were also reported in the Supporting Information of [50] and, interestingly, [50] also reported variations between vials with different fat fractions for the behavior of global T_1 values calculated without discussion about possible reasons. If variations in global T_1 values across echoes for SM2A and SM2B could be explained by different IP-OP conditions solely, it would be valid for vial #4 only as explained in the next sentences. More precisely, echo #1 was OP and would have had a lower MP2RAGE signal than echoes #2 and #3, which were IP. Lower MP2RAGE signal values result in longer T_1 values and vice-and-versa. Consequently, variations in global T_1 values seen for vial #4 for SM2A and SM2B could be explained by IP-OP conditions. However, the same reasoning would not be valid to describe the incremental increase of mean global T_1 values with increasing TE for vial #5 and #7. At that point, the relevance of having accurate and precise global T_1 maps from ME-MP2RAGE protocols designed for fat-water separated T_1 mapping of objects containing fat and water was put aside and emphasis was put on fat-water separated T_1 mapping.

For experiment #2, SS2 was modified from experiment #1 (i.e., from SS1) to test version A of the short T_1 protocol tested in numerical simulations. SS2 gave the same accuracy and precision level as SS1 while being is ~8% faster than SS1. Even if slightly more sensitive to B_1^+ inhomogeneities than SS1, SS2 did not show lower accuracy and precision.

Optimizing the MP2RAGE protocol for a range of shorter T_1 values was a clear improvement when comparing the accuracy and precision of the short T_1 protocols with the brain T_1 MP2RAGE protocol for the three first vials. As discussed in section 5.3, LS2 was modified to provide a better example of a brain T_1 MP2RAGE protocol to improve the comparison against short T_1 protocols. The difference in accuracy and precision for vial #1 was undeniable. However, the improvement in accuracy and precision for the short T_1 protocols rapidly disappeared after the three vials with shortest mean global T_1 values. Thus, up to approximately 400 ms, global T_1 maps calculated from SS2, SM2A or SM2B benefited from the short T_1 optimization regarding accuracy and precision. However, as seen with results from experiment #1 also, the advantage in precision predicted from numerical simulations for the short T_1 protocol was not apparent for global T_1 values longer than 400 ms approximately. These experimental results for accuracy and precision showed the relevance of numerical simulations while simultaneously showing their limitations by explaining only part of the observed deviations.

SM2A and SM2B were able to demonstrate feasibility of fat-water separated T_1 mapping from ME-MP2RAGE protocols by producing high quality fat and water T_1 maps. Water T_1 values calculated inside vials with water only were extremely similar to the global T_1 values calculated from IR-SE. The mean water T_1 values calculated for the three vials with fat were different from the reference. That was not surprising since IR-SE could only produce global T_1 maps where water and fat signals were not differentiated. SM2A and SM2B produced similar mean water T_1 values between each other. However, the water T_1 values calculated inside vials #5 and #7 showed larger differences between SM2A and SM2B than vial #4. As known from numerical simulation results, SM2A and SM2B were designed for short T_1 values. Thus, less accurate and precise T_1 values were expected for long T_1 values as the ones calculated for vial #5 and #7. The considerable difference in precision for water T_1 values calculated for vials #5 and #7 might be a

consequence of the difference in B_1^+ sensitivities between SM2A and SM2B. Since SM2B was designed to be less sensitive to B_1^+ inhomogeneities compared to SM2A, it is a possible that B_1^+ inhomogeneities could explain the lower overall precision of the results produced by SM2A.

Regarding fat T_1 values, SM2A and SM2B produced highly similar mean T_1 and standard deviations values across vials. The amount of fat present could have impacted the precision level of the fat T_1 values. For instance, vial #7 with an FF of 25% gave the smallest precision for both protocols, but less fat was present in comparison with the two other vials with an FF=50%. Theoretically, no impact was expected from GBCA on fat T_1 values since gadolinium-based contrast agent only affects the relaxivity of water protons [13]. However, a minor decrease in precision and increase in the mean fat T_1 values calculated were observed between vial #4 (with GBCA) and #5 (no GBCA) for SM2A and SM2B. Moreover, the fat T_1 values calculated for SM2A and SM2B were highly comparable with the fat T_1 value reported from pure fat (pure peanut oil) of 235 ms [41] and slightly superior to fat T_1 values measured with similar fat fractions of peanut oil in [50]. Extensive quantitative comparisons with [41] and [50] were not possible due to the limited presentation of the results. Ultimately, the conclusions that could be drawn on fat T_1 values measured from experiment #2 were limited by the small number of vials with fat and GBCA. For instance, it was not possible to conclude whether SM2B was better than SM2A due to its higher B_1^+ insensitivity for fat T_1 values. Thus, to have a more extensive analysis of the effects of GBCA and FF on fat T_1 values, experiment #3 was designed

The quality of the resulting fat-water separation from 3-point Dixon was an important factor to produce high quality of fat-water separated T_1 maps. Since every RAGE block and ME-MP2RAGE protocol has different levels of noise (and SNR), different combinations of c_1 and c_2 were expected. However, as reported in [39], discrepancies up to a factor of 25 between two c_2 values gave successful fat-water separation meaning that the exact value of c_2 was not critical. From ad hoc qualitative assessments done in this project, it was also found that c_1 could vary many fold and still produce successful fat-water separation. If no fat-water swaps were detected from a quick visual assessment of the fat and water MP2RAGE images, the fat-water separation was deemed acceptable.

Fat and water fraction calculations were not performed with the resulting fat and water MP2RAGE images. Due to the inherent T_1 weighting of the individual RAGE images acquired at different TIs, biases in fat and water fractions were inevitable and expected. In the end, calculation of the fat and water fractions were not part of the end goal of this project but a more complete signal model could be implemented for the proposed technique in future work to address this limitation.

Relaxivity measurements from global T_1 values calculated for experiment #2 were highly comparable with values from experiment #1 and with [38], [53] except for LS2. As for experiment #1, relaxivity measurements confirmed the quality of the global T_1 maps produced for experiment #2 by acting as a sanity check again. Moreover, the global relaxivity measurements from experiment #2 clearly showed the benefit of optimizing the MP2RAGE protocols for shorter T_1 values as visible with the relaxivity value calculated for LS2.

5.5 Quantitative assessment of fat-water separated T_1 mapping from ME-MP2RAGE protocols across a wide range of T_1 values

For SM3A and SM3B, global T_1 maps produced in experiment #3 showed comparable noise levels throughout the last two echoes whereas global T_1 maps from the first echo showed an increased level of noise. It is important to point out that the first echo of SM3A and SM3B were acquired when fat and water protons were close to OP condition. Thus, less signal and more T_1 variability was expected.

A crucial element to mention is the high probability that GBCA concentrations for the column #4 (FF=12.5%) were wrong for vials A (0.156 mM) and C (0.050 mM) due to an experimental error. Especially, an error in the true volume of GBCA solution added in the vials is suspected because the mean water T_1 values and standard deviations calculated were unexpectedly short and precise for these two vials in comparison with the other mean T_1 values and standard deviations for SM3A and SM3B. Furthermore, relaxivity and standard deviations calculated in water for SM3A and SM3B for FF = 12.5% were substantial outliers, presumably because the GBCA concentrations were inaccurate. Another indication pointing towards an experimental

error is the fact that the four vials with a fat fraction of 12.5% had to be remade promptly a second time at the end of experimental manipulations because an error in the use of the micropipette was realized (a different error than the alleged error discussed in this paragraph). Ultimately, the analysis of the water T_1 values was limited because of the possible error in [GBCA] and any result from these two vials must be put into context of this error.

Regarding fat and water specific T_1 maps, SM3B outperformed SM3A considerably in terms of uniformity and precision. In fact, two of the vials where SM3A showed higher precision for fat and water T_1 maps were the two vials with the possible error in concentration of GBCA. Phantom #3 contained (1) smaller vials than phantom #1 and #2 for the same voxel size and (2) a large polystyrene holder, in addition to (3) unwanted air bubbles in vials inside the FOV due to the positioning of the phantom during the acquisition. Consequently, partial volume effects, B_0 and B_1^+ inhomogeneities might have been considerably present inside the region of interest. Thus, the lower precision of SM3A for water and fat T_1 maps compared to SM3B might be explained by the difference in B_1^+ sensitivity and B_0 uniformity (not studied with in this project) for each protocol. On the other hand, SM3A is 37% faster (2:48 min) to acquire than SM3B (4:28 min). However, this increase in scan time does not seem worthwhile when we observed the decrease in precision and uniformity of the fat and water separated T_1 maps. Water T_1 maps from experiment #2 gave some insights towards this conclusion by showing lower precision for SM2A but no precision difference was measured for fat T_1 maps. Experiment #3 gave a conspicuous difference of precision and uniformity between the two protocols for both fat and water separated T_1 maps. If scan time would be an issue, using a higher parallel imaging acceleration factor, partial Fourier, and acquiring fewer or thicker slices with protocol SM3B would be recommended instead of using SM3A. In the end, 4:28 min is still a relatively short acquisition time that could be easily implemented in clinical situations.

Another factor that could explain the lower precision of T_1 maps produced from SM3A was the lower quality of the fat-water separation for that protocol. Finding an optimal combination of c_1 and c_2 that did not produce any fat-water swaps was very difficult for SM3A. The presence of polystyrene and air bubbles in the phantom definitely impacted the quality of the fat-water separation algorithm for SM3A (and SM3B also but in a lesser way) by creating many phase

wraps in the phase images (not shown). The choice of c_1 and c_2 depends on the level of noise in the resulting images. At first, it was assumed that c_1 and c_2 should be exactly the same from SM2A to SM3A (or SM2B and SM3B) because they were exactly the same protocols. However, the two phantoms used for experiment #2 and #3 were quite different which ultimately resulted in minor variations in c_1 and c_2 for both protocols.

While it was less evident for SM3A due to poor precision levels, SM3B showed a clear decrease in water T_1 values with increasing FF for a constant GBCA concentration (excluding the two vials with the presumed error). That observation is contradictory with the conclusions drawn from [41] and [50] where no variation in water T_1 with increasing fat fraction was observed. However, other works [36], [54], [55] reported a decrease of water T_1 values with increasing fat fraction. The decrease of water T_1 with increasing fat fraction would mean that the presence of fat protons increases the relaxation rates of water protons like GBCA. It is important to specify that the actual underlying mechanisms producing this effect are unknown for the moment. Additional work will need to be done to quantitatively assess the interesting behavior observed in water T_1 values with the presence of fat.

With regards to the water T_1 values with increasing concentrations of GBCA (and a constant FF), most of the fat fractions showed the expected decrease of water T_1 values. The increase in water relaxation R_1 rates with increasing concentration of GBCA was found to be linear for most of the fat fractions. However, the linear slope measured from water relaxation rates against concentration of GBCA were lower overall than the linear slope measured for experiments #1 and #2. FF=12.5% did not show the expected decrease in water T_1 values for both protocols probably due to the experimental error explained at the beginning of this section. For FF=50% of SM3A, the inconsistent behavior of mean water T_1 values might be explained by the poor level of precision for FF = 50%. Indeed, standard deviations up to ~47% of the mean water T_1 values calculated were observed. The lower precision levels seen for both protocols for FF=50% was probably due to lower water signal was inside these vials. Moreover, the water in the vial with 50% fat was part of the safflower oil emulsion that contained several ingredients and not deionized distilled water. For other vials with smaller fat fractions (produced from dilutions), deionized and distilled water was added to the safflower oil emulsion. Specifically, other than

safflower oil and water, the safflower oil emulsion contained polyglycerol esters of fatty acids, soy lecithin, xanthan gum, and ascorbic acid. The possible impacts of these ingredients on water T_1 values are unknown and, to clarify the possible effects, a review of literature with experimental acquisitions with these ingredients with water only could be done in future work.

For SM3B, the mean T_1 value of pure water (FF =0% and [GBCA] = 0 mM) was highly similar to the mean water T_1 values of 2334 ms reported in [41] and approximately 2500 ms (value shown on a figure but not explicitly reported in a table) in [50]. SM3A calculated a mean water T_1 value considerably larger than the two values reported in the previous sentence. Additional comparisons with [35] and [42] were not possible because phantom #3 used in this project did not contain agarose.

An important element to recall about SM3A and SM3B is that both protocols were optimized for a short T_1 range of interest between 200 ms and 800 ms and not long T_1 values. Therefore, it was expected to observe low precision levels for water T_1 values longer than 1000 ms since both protocols were not designed for these T_1 values. However, even if this argument is considered, SM3B clearly outperformed SM3A in precision even for long water T_1 values.

The uniformity (or stability) and precision of fat T_1 values measured for SM3B were superior to SM3A across FFs and concentrations of GBCA and that statement is glaring when comparing the mean fat T_1 values and standard deviations calculated for FF = 50% for the two protocols. The only FF where precision levels were comparable between SM3A and SM3B was 12.5% and that column had poor SNR probably due to the low quantity of fat inside the vials.

Moreover, SM3B should be able to detect variations in fat T_1 values caused by variations in oxygen concentrations. The precision levels of fat T_1 values calculated for a fat fraction of 50% seem to be high enough to detect variations in fat T_1 values caused by different oxygen levels as reported in [36] with Fat DESPOT. Specifically, in [36], a fat T_1 of 333 ms was measured for an oxygen concentration of 20% whereas ~290 ms was reported for an oxygen concentration of 60%. The 43 ms of difference between the two fat T_1 values is larger than standard deviations measured for SM3B at a fat fraction of 50%.

The mean fat T_1 values calculated in this work for experiment #2 and #3 were slightly superior to the values reported in [41] and [50] for peanut oil but highly comparable to [36] for safflower oil emulsion. Extensive comparisons of the fat T_1 values calculated in this work with [50] would have been interesting although comparisons were limited due to the quantity and presentation of the results.

No general trend was observed throughout concentrations of GBCA and FFs for fat T_1 values but variations were still noticeable. The relaxivity of gadolinium-based contrast agent is known to affect water protons exclusively [56] and this supports the result presented here that fat T_1 values should not be disturbed by the presence and quantity of gadolinium-based contrast agent. However, the influence of the FF on the fat T_1 values is less understood. First, no discernable trend for fat T_1 values were detected across FF, in agreement with [50]. On the other hand, recent works where fat T_1 values were measured with STEAM-MRS reported that increasing the fat fraction (same range of FF as this work) resulted in the decrease of fat T_1 values of most individual resonances in the spectrum of safflower oil except for the methylene peak [36]. The disagreement about the decrease of fat T_1 values with increasing fat fraction could be explained by the fact that fat peaks were not individually discriminated here for calculations of fat T_1 values, unlike in [36]. Considering that the proposed technique in this work used a single fat T_1 value to describe all fat resonances, which ignored possible T_1 variations between resonances and resulted in a composite fat T_1 value representing all fat peaks, it is possible that the decrease in fat T_1 values with increasing FF for secondary fat peaks might have been hidden by the stable fat T_1 values of the methylene peak.

There is currently no well-established reference technique for water and fat specific T_1 mapping since fat and water separated T_1 mapping is relatively recent in qMRI [36], [41] and [50]. It would be interesting to develop a two-compartment model for IR-SE acquisitions to produce fat-water separated T_1 maps from a reference technique. The fat-water separated T_1 maps could then be used as reference. For global T_1 mapping, IR-SE is easily considered as the gold standard for global T_1 mapping [20] and the sequence is readily available on all MRI platforms across the

world. Thus, the water and fat T_1 values calculated in this work could not be compared with a reference technique.

Relaxivity values calculated from water R_1 values for SM3A and SM3B were an additional result showing the superior uniformity of SM3B. It was evident that water R_1 (and relaxivity) values were constrained in a much smaller range for SM3B than water R_1 values from SM3A.

However, the relaxivity values measured in experiment #3 did not provide a solid result as in experiments #1 and #2, but this could be due to the range of concentrations of GBCA used. A narrow range of concentrations of GBCA was used and minor errors in R_1 values or concentrations of GBCA might have been overly expressed. More precisely, the maximum concentration of GBCA used in experiment #3 was ~0.35 mM whereas concentrations larger than 1 mM and even up to 16 mM are frequently reported in the literature to measure relaxivity in phantoms [38] or human blood plasma [57]. Moreover, nonlinear relationships between global R_1 values and concentrations of GBCA have been reported at low concentrations for experimental formulations of GBCA [58]. Thus, the relaxivity values measured from experiment #3 did not provide the desired validation of the quality of the T_1 maps produced and further acquisitions and assessments would be required to figure out the discrepancies observed.

Chapter 6

Conclusion

6.1 Overview

With the work completed during this project, a novel T_1 mapping technique able to produce accurate and precise fat-specific T_1 maps optimized for short T_1 values between 200 ms and 800 ms has been successfully developed and validated thoroughly in phantoms.

First, a qualitative assessment of the MP2RAGE-T_1 lookup tables was done to study the impact of individual acquisition parameters on the lookup table and two MP2RAGE protocols optimized for short T_1 values between 200 ms and 800 ms were found. The qualitative assessment of the MP2RAGE lookup tables helped to recognize the flexibility of the MP2RAGE protocol to be optimized for various T_1 range of interest. The qualitative assessment was then followed by a quantitative assessment with numerical simulations. The numerical simulations allowed to fine-tune the acquisition parameters found from the qualitative assessment to create a short T_1 MP2RAGE protocol with higher theoretical accuracy and precision than the original MP2RAGE protocol designed for brain T_1 values.

Afterwards, the newly designed MP2RAGE protocol for short T_1 values was experimentally validated inside a homemade phantom against the original brain T_1 MP2RAGE protocol and IR-SE considered the reference technique for global T_1 mapping. The experimental feasibility of a ME-MP2RAGE including three echoes (with the same acquisition parameters as the short T_1 single echo MP2RAGE) was also verified. The few variations of the short T_1 MP2RAGE protocol tested experimentally showed better accuracy and precision in global T_1 values for most of the vials inside the predefined T_1 range of interest compared to the original brain T_1 MP2RAGE protocol. In addition, the water T_1 values calculated from the ME-MP2RAGE protocol, and 3-point Dixon demonstrated remarkable similarity with the global T_1 values

calculated from the individual echoes of the same protocol and the reference. Finally, accuracy and precision in global T_1 values calculated for the various short T_1 MP2RAGE protocols were highly similar to values reported in the literature [41].

The experimental feasibility of fat-water separated T_1 mapping from two ME-MP2RAGE protocols optimized for short T_1 values was demonstrated with a homemade phantom containing fat and water. One ME-MP2RAGE protocol was designed for fast scanning whereas the other protocol was designed to be less sensitive to B_1^+ inhomogeneities. The two variations of the ME-MP2RAGE protocol optimized for short T_1 mapping were able to produce uniform, precise and comparable fat T_1 maps between protocols and with the literature [41], [50]. Moreover, the two ME-MP2RAGE protocols were able to produce highly accurate and precise water T_1 maps for water-only vials when compared to the reference. For water T_1 values calculated inside vials with fat, the ME-MP2RAGE protocol designed with a lower sensitivity to B_1^+ inhomogeneities showed higher precision than the fast implementation of the ME-MP2RAGE protocol.

Finally, fat and water separated T_1 values calculated from both variations of the short T_1 ME-MP2RAGE protocol were quantitatively assessed across a wide range of T_1 values and extensively compared with a new phantom and experiment. The water T_1 values calculated from the protocol less sensitive to B_1^+ inhomogeneities showed a decrease with increasing fat fractions whereas the low precision level of the fast implementation did not reveal the same trend. For both versions of the ME-MP2RAGE protocol, the fat T_1 values did not show general trend among the different fat fractions and concentrations of GBCA. In the end, the ME-MP2RAGE protocol less sensitive to B_1^+ inhomogeneities showed superior uniformity and precision for both fat and water T_1 values calculated than the fast implementation of the ME-MP2RAGE protocol.

Ultimately, the experiments and analyses presented in this thesis resulted in the development of a new ME-MP2RAGE protocol combined with 3-point Dixon. This newly designed protocol can produce high quality global, fat and water separated T_1 maps simultaneously. Even if the protocol is optimized for a range of short T_1 values where fat T_1 values are normally measured, the protocol can also map longer T_1 values correctly. The ME-MP2RAGE protocol proposed in this thesis possesses a faster or comparable scan time as other similar techniques [41], [50]. In

addition, the ME-MP2RAGE protocol is considerably simpler to implement than other equivalent techniques [41], [50] because it does not require the use of sophisticated reconstruction algorithms with several hours of computer calculations to produce the fat-water separated T_1 maps. For the ME-MP2RAGE protocol proposed in this thesis, the T_1 mapping and 3-point Dixon processes together took less than 5 seconds to calculate. To the best of our knowledge, MP2RAGE has not been applied or adapted to short T_1 values (i.e., < 1000 ms) yet nor combined with 3-point Dixon to produce fat-water separated MP2RAGE images. The MP2RAGE sequence is typically used for brain T_1 mapping [8] where there is no fat signal. The ME version of the MP2RAGE sequence has been used by many in prior studies [7], [9] and [10] to extract parameters like T_2^* or Quantitative Susceptibility Mapping (QSM). It appears that no application with 3-point Dixon to separate the MP2RAGE images into fat-water separated MP2RAGE images has been reported. One application of 2-point Dixon with MP2RAGE has been observed in the literature to facilitate brain tissue segmentation and skull stripping [59].

6.2 Future work

The next step for this project would be to do experimental acquisitions *in vivo*. Indeed, after the extensive validation and assessment in phantoms, the subsequent experiment should be in anatomical regions with fat like the bone marrow, skeletal muscle with fat infiltrations, liver with fatty-liver disease, adipose tissues, or heart. *In vivo* acquisitions would enable a greater assessment of the B_0, B_1^+ and motion sensitivities of the proposed ME-MP2RAGE protocol presented in this work. Furthermore, *in vivo* acquisitions would allow a more extensive quantitative comparison with similar techniques proposed in the literature [41], [50]. *In vivo* acquisitions will also grant the possibility to assess how the 3-point Dixon from a ME-MP2RAGE sequence performs under harsher conditions than in phantom.

It could also be interesting to develop a two-compartment signal model from IR-SE signal to produce a new "reference" fat-water separated T_1 mapping technique. Currently, IR-SE cannot differentiate signal coming from fat and water protons which ultimately limits IR-SE to produce global T_1 maps solely. Fat-water separated T_1 mapping currently lacks from a well-established reference technique contrarily to global T_1 mapping.

Another future step for this project would be to use the ME-MP2RAGE (and 3-point Dixon) to evaluate how fat T_1 values vary with the presence of oxygen. The presence of oxygen is an excessively important factor in the outcome of radiotherapy treatments [4]. Since the ME-MP2RAGE protocol is optimized for a T_1 range where fat T_1 values are found and that fat T_1 values are more sensitive to variations in oxygen level than water and global T_1 values [36], the technique would be an excellent candidate to measure non-invasively the oxygen levels in cancer tumors. Ultimately, the ME-MP2RAGE protocol with 3-point Dixon would be a useful tool to perform a more thorough assessment of the impact of oxygen levels on fat T_1. By first testing the technique in phantom, it would be possible to measure the sensitivity of the fat T_1 from the ME-MP2RAGE protocol to different oxygen levels. If the phantom tests are conclusive, the ME-MP2RAGE protocol could be tested *in vivo* afterwards.

References

[1] W. Hollingworth, C. J. Todd, M. I. Bell, Q. Arafat, S. Girling, K. R. Karia, and A. K. Dixon, The diagnostic and therapeutic impact of MRI: An observational multi-centre study, Clin. Radiol., vol. 55, no. 11, pp. 825–831, 2000.

[2] P. Metcalfe, G. P. Liney, L. Holloway, A. Walker, M. Barton, G. P. Delaney, S. Vinod, and W. Tomé, The potential for an enhanced role for MRI in radiation-therapy treatment planning, Technol. Cancer Res. Treat., vol. 12, no. 5, pp. 429–446, 2013.

[3] M. Just, M and Thelen, Tissue characterization with T1, T2, and proton density values: results in 160 patients with brain tumors., Radiology, vol. 169, no. 3, pp. 779–785, 1988.

[4] R. A. Gatenby, H. B. Kessler, J. S. Rosenblum, L. R. Coia, P. J. Moldofsky, W. H. Hartz, and G. J. Broder, Oxygen distribution in squamous cell carcinoma metastases and its relationship to outcome of radiation therapy, Int. J. Radiat. Oncol. Biol. Phys., vol. 14, no. 5, pp. 831–838, 1988.

[5] J. M. Arbeit, J. M. Brown, K. S. C. Chao, J. D. Chapman, W. C. Eckelman, A. W. Fyles, A. J. Giaccia, R. P. Hill, C. J. Koch, … J. L. Tatum, Hypoxia: Importance in tumor biology, noninvasive measurement by imaging, and value of its measurement in the management of cancer therapy, Int. J. Radiat. Biol., vol. 82, no. 10, pp. 699–757, 2006.

[6] L. Schroeder and C. Faber, In vivo NMR Imaging: Methods and Protocols. Springer Protocols, 2011.

[7] F. Colliez, M. A. Neveu, J. Magat, T. T. C. Pham, B. Gallez, and B. F. Jordan, Qualification of a noninvasive magnetic resonance imaging biomarker to assess tumor oxygenation, Clin. Cancer Res., vol. 20, no. 21, pp. 5403–5411, 2014.

[8] J. P. Marques, T. Kober, G. Krueger, W. van der Zwaag, P. F. Van de Moortele, and R. Gruetter, MP2RAGE, a self bias-field corrected sequence for improved segmentation and T1-mapping at high field, Neuroimage, vol. 49, no. 2, pp. 1271–1281, 2010.

[9] R. Metere, T. Kober, H. E. Möller, and A. Schäfer, Simultaneous quantitative MRI mapping of T1, T2∗ and magnetic susceptibility with Multi-Echo MP2RAGE, PLoS One, vol. 12, no. 1, pp. 1–28, 2017.

[10] G. H. Glover, Multipoint Dixon technique for water and fat proton and susceptibility imaging, J. Magn. Reson. Imaging, vol. 1, no. 5, pp. 521–530, 1991.

[11] D. G. Nishimura, Principles of magnetic resonance imaging. 1996.

[12] M. A. Berstein, K. F. King, and X. J. Zhou, Handbook of MRI pulse sequences. 2004.

[13] R. B. Lauffer, Paramagnetic Metal Complexes as Water Proton Relaxation Agents for NMR Imaging: Theory and Design, Chem. Rev., vol. 87, no. 5, pp. 901–927, 1987.

[14] M. Rohrer, H. Bauer, and J. Mintorovitch, Comparison of Magnetic Properties of MRI Contrast Media Solutions at Different Magnetic Field Strengths, Invest. Radiol., vol. 40, no. 11, pp. 715–724, 2005.

[15] K. P. Pruessmann, M. Weiger, M. B. Scheidegger, and P. Boesiger, SENSE: sensitivity encoding for fast MRI, Magn. Reson. Med. An Off. J. Int. Soc. Magn. Reson. Med., vol. 42, no. 5, pp. 952–962, 1999.

[16] M. A. Griswold, P. M. Jakob, R. M. Heidemann, M. Nittka, V. Jellus, J. Wang, B. Kiefer, and A. Haase, Generalized Autocalibrating Partially Parallel Acquisitions (GRAPPA), Magn. Reson. Med., vol. 47, no. 6, pp. 1202–1210, 2002.

[17] M. Blaimer, F. Breuer, M. Mueller, R. M. Heidemann, M. A. Griswold, and P. M. Jakob, SMASH, SENSE, PILS, GRAPPA: how to choose the optimal method, Top. Magn. Reson. Imaging, vol. 15, no. 4, pp. 223–236, 2004.

[18] S. Eminian, S. D. Hajdu, R. A. Meuli, P. Maeder, and P. Hagmann, Rapid high resolution T1 mapping as a marker of brain development: Normative ranges in key regions of interest, PLoS One, vol. 13, no. 6, pp. 1–16, 2018.

[19] A. J. Taylor, M. Salerno, R. Dharmakumar, and M. Jerosch-Herold, T1 Mapping Basic Techniques and Clinical Applications, JACC Cardiovasc. Imaging, vol. 9, no. 1, pp. 67–81, 2016.

[20] N. Stikov, M. Boudreau, I. R. Levesque, C. L. Tardif, J. K. Barral, and G. B. Pike, On the accuracy of T1 mapping: Searching for common ground, Magn. Reson. Med., vol. 73, no. 2, pp. 514–522, 2015.

[21] R. J. Ogg and P. B. Kingsley, Optimized Precision of Inversion-Recovery T1 Measurements for Constrained Scan Time, Magn. Reson. Med., vol. 51, no. 3, pp. 625–630, 2004.

[22] J. Hennig, A. Nauerth, and H. Friedburg, RARE imaging: a fast imaging method for

clinical MR, Magn. Reson. Med., vol. 3, no. 6, pp. 823–833, 1986.

[23] M. K. Stehling, R. Turner, and P. Mansfield, Echo-planar imaging: Magnetic resonance imaging in a fraction of a second, Science (80-.)., vol. 254, no. 5028, pp. 43–50, 1991.

[24] D. R. Messroghli, A. Radjenovic, S. Kozerke, D. M. Higgins, M. U. Sivananthan, and J. P. Ridgway, Modified look-locker inversion recovery (MOLLI) for high-resolution T 1 mapping of the heart, Magn. Reson. Med., vol. 52, no. 1, pp. 141–146, 2004.

[25] E. K. Fram, R. J. Herfkens, G. A. Johnson, G. H. Glover, J. P. Karis, A. Shimakawa, T. G. Perkins, and N. J. Pelc, Rapid calculation of T1 using variable flip angle gradient refocused imaging, Magn. Reson. Imaging, vol. 5, no. 3, pp. 201–208, 1987.

[26] F. H. Epstein, J. P. Mugler, and J. R. Brookeman, Spoiling of transverse magnetization in gradient-echo (GRE) imaging during the approach to steady state, Magn. Reson. Med., vol. 35, no. 2, pp. 237–245, 1996.

[27] J. P. Mugler and J. R. Brookeman, Three-dimensional magnetization-prepared rapid gradient-echo imaging (3D MP RAGE), Magn. Reson. Med., vol. 15, no. 1, pp. 152–157, 1990.

[28] A. Haase, D. Matthaei, R. Bartkowski, E. D{\"u}hmke, and D. Leibfritz, Inversion recovery snapshot FLASH MR imaging., J. Comput. Assist. Tomogr., vol. 13, no. 6, pp. 1036--1040, 1989.

[29] J. V. Liu, N. A. Bock, and A. C. Silva, Rapid high-resolution three-dimensional mapping of T1 and age-dependent variations in the non-human primate brain using magnetization-prepared rapid gradient-echo (MPRAGE) sequence, Neuroimage, vol. 56, no. 3, pp. 1154–1163, 2011.

[30] L. Chen, Whole-brain T1 Mapping and CNR Optimization using MP3RAGE pulse sequence at 3.0Tesla, National Sun Yat-sen University, 2016.

[31] W. Proctor and F. Yu, The dependence of a nuclear magnetic resonance frequency upon chemical compound, Phys. Rev., vol. 77, no. 5, p. 717, 1950.

[32] N. van Vucht, R. Santiago, B. Lottmann, I. Pressney, D. Harder, A. Sheikh, and A. Saifuddin, The Dixon technique for MRI of the bone marrow, Skeletal Radiol., vol. 48, no. 12, pp. 1861–1874, 2019.

[33] W. T. Dixon, Simple proton spectroscopic imaging, Radiology, vol. 153, no. 1, pp. 189–194, 1984.

[34] J. Ma, Dixon techniques for water and fat imaging, J. Magn. Reson. Imaging, vol. 28, no. 3, pp. 543–558, 2008.

[35] V. Fortier and I. R. Levesque, Phase processing for quantitative susceptibility mapping of regions with large susceptibility and lack of signal, Magn. Reson. Med., vol. 79, no. 6, pp. 3103–3113, 2018.

[36] V. Fortier, Evaluation of Tumor Hypoxia with Magnetic Resonance Imaging, McGill University, 2021.

[37] K. Hattori, Y. Ikemoto, W. Takao, S. Ohno, T. Harimoto, S. Kanazawa, M. Oita, K. Shibuya, M. Kuroda, and H. Kato, Development of MRI phantom equivalent to human tissues for 3.0-T MRI, Med. Phys., vol. 40, no. 3, 2013.

[38] A. Kolokotronis, Robust Characterization of Longitudinal Magnetic Resonance Relaxation with Application to Novel Nanoparticles, McGill University, 2020.

[39] J. Berglund, L. Johansson, H. Ahlström, and J. Kullberg, Three-point Dixon method enables whole-body water and fat imaging of obese subjects, Magn. Reson. Med., vol. 63, no. 6, pp. 1659–1668, 2010.

[40] J. P. Marques and R. Gruetter, New Developments and Applications of the MP2RAGE Sequence - Focusing the Contrast and High Spatial Resolution R1 Mapping, PLoS One, vol. 8, no. 7, 2013.

[41] L. Feng, F. Liu, G. Soultanidis, C. Liu, T. Benkert, K. T. Block, Z. A. Fayad, and Y. Yang, Magnetization-prepared GRASP MRI for rapid 3D T1 mapping and fat/water-separated T1 mapping, Magn. Reson. Med., vol. 86, no. 1, pp. 97–114, 2021.

[42] A. Yamashiro, M. Kobayashi, and T. Saito, Cerebrospinal fluid T1 value phantom reproduction at scan room temperature, J. Appl. Clin. Med. Phys., vol. 20, no. 7, pp. 166–175, 2019.

[43] M. W. A. Caan, P. L. Bazin, J. P. Marques, G. de Hollander, S. O. Dumoulin, and W. van der Zwaag, MP2RAGEME: T 1 , T 2* , and QSM mapping in one sequence at 7 tesla, Hum. Brain Mapp., vol. 40, no. 6, pp. 1786–1798, 2019.

[44] H. Sun, J. O. Cleary, R. Glarin, S. C. Kolbe, R. J. Ordidge, B. A. Moffat, and G. B. Pike, Extracting more for less: multi-echo MP2RAGE for simultaneous T1-weighted imaging, T1 mapping, R2∗ mapping, SWI, and QSM from a single acquisition, Magn. Reson. Med., vol. 83, no. 4, pp. 1178–1191, 2020.

[45] R. A. M. Haast, J. C. Lau, D. Ivanov, R. S. Menon, K. Uludağ, and A. R. Khan, Effects of MP2RAGE B1+ sensitivity on inter-site T1 reproducibility and hippocampal morphometry at 7T, Neuroimage, vol. 224, p. 117373, 2021.

[46] C. Y. Liu, C. A. McKenzie, H. Yu, J. H. Brittain, and S. B. Reeder, Fat quantification with IDEAL gradient echo imaging: Correction of bias from T1 and noise, Magn. Reson. Med., vol. 58, no. 2, pp. 354–364, 2007.

[47] A. C. Hurley, A. Al-Radaideh, L. Bai, U. Aickelin, R. Coxon, P. Glover, and P. A. Gowland, Tailored RF pulse for magnetization inversion at ultrahigh field, Magn. Reson. Med., vol. 63, no. 1, pp. 51–58, 2010.

[48] T. L. Faller, A. J. Trotier, S. Miraux, and E. J. Ribot, Radial MP2RAGE sequence for rapid 3D T1 mapping of mouse abdomen: application to hepatic metastases, Eur. Radiol., vol. 29, no. 11, pp. 5844–5851, 2019.

[49] R. Deichmann, C. D. Good, O. Josephs, J. Ashburner, and R. Turner, Optimization of 3-D MP-RAGE sequences for structural brain imaging, Neuroimage, vol. 12, no. 1, pp. 112–127, 2000.

[50] O. Jaubert, G. Cruz, A. Bustin, T. Schneider, B. Lavin, P. Koken, R. Hajhosseiny, M. Doneva, D. Rueckert, … C. Prieto, Water–fat Dixon cardiac magnetic resonance fingerprinting, Magn. Reson. Med., vol. 83, no. 6, pp. 2107–2123, 2020.

[51] F. Franconi, L. Lemaire, H. Saint-Jalmes, and P. Saulnier, Tissue oxygenation mapping by combined chemical shift and T 1 magnetic resonance imaging, Magn. Reson. Med., vol. 79, no. 4, pp. 1981–1991, 2018.

[52] H. Yu, A. Shimakawa, C. A. McKenzie, W. Lu, S. B. Reeder, R. S. Hinks, and J. H. Brittain, Phase and amplitude correction for multi-echo water-fat separation with bipolar acquisitions, J. Magn. Reson. Imaging, vol. 31, no. 5, pp. 1264–1271, 2010.

[53] A. F. Stalder, D. V. Elverfeldt, D. Paul, J. Hennig, and M. Markl, Variable echo time imaging: Signal characteristics of 1-M gadobutrol contrast agent at 1.5 and 3T, Magn. Reson. Med., vol. 59, no. 1, pp. 113–123, 2008.

[54] H. H. Hu and K. S. Nayak, Change in the proton T1 of fat and water in mixture, Magn. Reson. Med., vol. 63, no. 2, pp. 494–501, 2010.

[55] C. Le Ster, J. Lasbleiz, S. Kannengiesser, R. Guillin, G. Gambarota, and H. Saint-Jalmes, A fast method for the quantification of fat fraction and relaxation times: Comparison of

five sites of bone marrow, Magn. Reson. Imaging, vol. 39, pp. 157–161, 2017.

[56] L. M. De Leõn-Rodríguez, A. F. Martins, M. C. Pinho, N. M. Rofsky, and A. D. Sherry, Basic MR relaxation mechanisms and contrast agent design, J. Magn. Reson. Imaging, vol. 42, no. 3, pp. 545–565, 2015.

[57] J. Pintaske, P. Martirosian, H. Graf, G. Erb, K.-P. Lodemann, C. D. Claussen, and F. Schick, Relaxivity of gadopentetate dimeglumine (Magnevist), gadobutrol (Gadovist), and gadobenate dimeglumine (MultiHance) in human blood plasma at 0.2, 1.5, and 3 Tesla, Invest. Radiol., vol. 41, no. 3, pp. 213–221, 2006.

[58] L. Vander Elst, F. Maton, S. Laurent, F. Seghi, F. Chapelle, and R. N. Muller, A multinuclear MR study of Gd-EOB-DTPA: Comprehensive preclinical characterization of an organ specific MRI contrast agent, Magn. Reson. Med., vol. 38, no. 4, pp. 604–614, 1997.

[59] T. Kober, A. Roche, O. Esteban, S. Gorthi, D. Ribes, M. Bach-cuadra, R. Meuli, and G. Krueger, Atlas-free Brain Tissue Segmentation Using a Single T1-weighted MRI Acquisition, in *International Society for Magnetic Resonance in Medicine (ISMRM'12), Melbourne, Australia*, 2012, vol. 49, no. 2, p. 5409.

[60] J. P. Ridgway, Cardiovascular magnetic resonance physics for clinicians: part I, J. Cardiovasc. Magn. Reson., vol. 12, no. 1, pp. 1–28, 2010.